# Work Fluctuations, Entanglement and Interference in Driven Open Quantum Systems

**Dissertation**

zur Erlangung des akademischen Grades
Dr. rer. nat.

eingereicht an der
Mathematisch-Naturwissenschaftlich-Technischen Fakultät
der Universität Augsburg

Von
**Ralf Blattmann**
aus
St. Peter (Schwarzwald)

Januar 2015

Universität
Augsburg
University

1. Gutachter: Prof. Dr. Dr. h.c. mult. Peter Hänggi
2. Gutachter: Dr. habil. Sigmund Kohler
Tag der mündlichen Prüfung: 09. Januar 2015

# Abstract

In this thesis, we investigate several aspects of driven open quantum systems relevant for experiments with artificial solid-state based systems. First, we propose how to measure the work performed by a time-dependent force and, thus, the work fluctuation relations in a quantum system. Generally, the experimental investigation of these relations in the quantum regime is hindered by the fact that it requires many projective energy measurements. As alternative that circumvents this problem, we investigate the implementation of a recent interferometric method in a circuit QED setup. We highlight that this method could be employed to obtain the work statistics of closed as well as open driven system, even in the strongly dissipative regime. Our simulations demonstrate the experimental feasibility.

In the second part, we explore the possibility to entangle an excitonic two-level system in a semiconductor quantum dot with a cavity defined on a photonic crystal by sweeping the cavity frequency across its resonance with the exciton transition. The dynamic cavity detuning is established by a radio-frequency surface acoustic wave (SAW). It induces Landau-Zener transitions between the excitonic and the photonic degrees of freedom and, thereby, entangles the subsystems. We perform a theoretical study with a master equation approach and optimize the scheme by using tailored Fourier-synthesized SAW pulses. Assuming experimentally demonstrated system parameters, we show that the composed pulses increase both the maximum entanglement and its persistence. The latter is only limited by the dominant dephasing mechanism, i.e., the photon loss from the cavity.

Sweeping periodically through an avoided crossing leads to a series of transitions and results in Landau-Zener-Stückelberg-Majorana (LZSM) interference patterns which we investigate in the third part of this thesis. We derive the structure of these patterns for a qubit that experiences quantum dissipation for time-periodic, but otherwise general driving. A spin-boson Hamiltonian serves as model which we treat with a Bloch-Redfield master equation in Floquet basis. It predicts a peak structure that depends sensitively on the operator through which the qubit couples to the bath. The Fourier transforms of the LZSM patterns exhibit arc structures which reflect the shape of the driving. These features are captured by an effective time-independent Bloch equation which provides an analytical solution.

# Contents

*Für Carla*

. . .

# Chapter 1

# Introduction

In quantum mechanics, the dynamics of a closed quantum system is completely determined by the Schrödinger equation [1] with a time-independent Hamilton operator that generates the time evolution. In practice, however, it is often neither feasible nor meaningful to consider the exact dynamics to describe a specific experimental situation. First, in experiments one often couples a quantum system to external fields, in order to prepare, control, or read out the system. A full quantum mechanical description of these external sources can increases the complexity drastically, because they usually have many microscopic degrees of freedom. In many cases, however, it is possible to condense these degrees of freedom to a single or few classical variables, which can be described by classical equations of motion involving a classical time parameter. Coupling these variables to a quantum system leads to semi-classical Hamiltonian that is time-dependent by itself [2,3].

Second, it is, in general, not possible to screen a quantum systems from its environment, which introduces dissipation and noise. For example, in solid-state based quantum systems, like quantum dots or superconducting circuits, environmental fluctuations, evoked by thermal phonons or the external circuitry, are unavoidable. These systems received increasing attention recently, one the hand because they exhibit quantum mechanical phenomena on a macroscopic scale, and on the other hand because they are promising candidates for future applications like, e.g., quantum computers. Since the environmental degrees of freedom are usually not controllable or even exactly measurable, they only can be taken into account effectively. Often, it is possible to model the environment as an infinite heat bath, and tracing out the bath degrees of freedom leads to an open system description for the reduced system. Appart from its coherent dynamics, the reduced system now also undergoes incoherent and irreversible processes because of its coupling to the bath [4–6].

In summary, it is often appropriate to consider the dynamics of a reduced system with time-dependent coefficients interacting with a heat bath, instead of the exact and

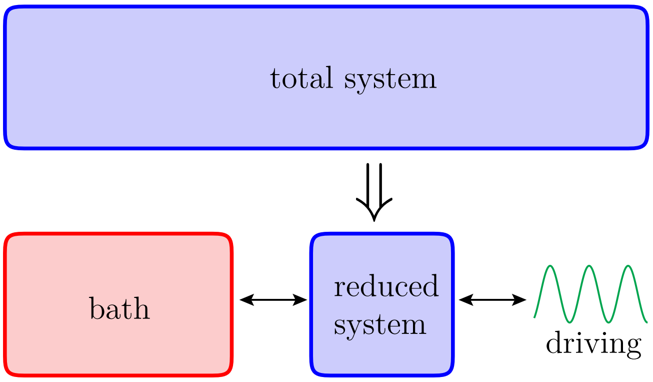

Figure 1.1: *Driven open quantum systems*: The complexity of the total system, including external fields and the environment, can be reduced by considering a reduced system interacting with a classical driving field and a heat bath. This leads to a time evolution that is governed by a explicitly time-dependent Hamiltonian and includes incoherent processes.

coherent dynamics, as illustrated in Fig. 1.1. This establishes the field of of driven open quantum systems. In this thesis, we will discuss several selected aspects of this field without claiming to offer a complete discussion of its variety of effects.

A time-dependent modulation of systems parameters, can be interpreted as a thermodynamic transformation. If a system is initially in thermal equilibrium and the modulation is slow (adiabatic), the transformation is reversible, and no heat is produced, however, if the modulation is faster (non-adiabatic) the transformation gets irreversible and the system heats up. In the latter case, the work performed on the system is larger than its gain of free energy. For large systems, close to equilibrium this statement follows from the second law of thermodynamics. For small systems, far from equilibrium, however, it is only true on average. Here, work becomes a random quantity which obeys so called (quantum) fluctuation relations [7]. While in the classical regime these relations have been studied also experimentally, in the quantum regime their experimental investigation turns out to be a difficult task, because there, in general, many projective energy measurement are needed, in order to determine the work performed by a time-dependent force. Recently, a novel method has been put forward [8,9] which avoids projective measurements by utilizing an interferometric scheme allowing to determine the characteristic function of work. In the first part of this thesis (Chapter 2), we propose to apply this method to an artificial quantum system based on superconducting circuits, in order to study work fluctuations. Therefore, we consider the archetype system of circuit QED [10] (cavity QED with superconducting circuits), a Cooper-pair box coupled to a transmission line resonator and discuss the adjustments needed to make this system suitable for the interferometric scheme. Our analysis will be supported by numerical simulations, testing the reliability of our arguments. While we restrict the numerical calculations to a closed system, we point out that the presented scheme in principle enables to measure work fluctuations in open quantum systems with arbitrarily strong coupling to the environment.

If a system, which is initially in an eigenstate, undergoes a time-dependent transformation, it will, in general, not be stationary. Only if the modulation is adiabatically slow,[1] the *adiabatic theorem* [12] guarantees that, if one starts in a stationary state, one stays in the corresponding stationary state, for all times [13]. Faster change of the system parameters will induce non-adiabatic transitions between the system's eigenstates [14] and the dynamics will become non-stationary. Here, the most fundamental paradigm is the Landau-Zener (LZ) problem (see Sec. 3.3), where the level splitting of a two-level system depends linearly on time [15–18]. If levels are connected by a tunnel coupling, the energy spectrum, as a function of time, forms an avoided crossing. While most of the time its evolution can be considered as adiabatic, the system experiences the tunnel coupling in the crossing region and, with certain probability, undergoes a transition to the initially unpopulated state. Consequently, the wavefunction splits into a superposition. The probability for such a non-adiabatic transition is given by the famous Landau-Zener formula (see Appendix B for a derivation), which tells us that the transition probability only depends on the tunnel coupling between the levels and the sweep velocity. This opens the possibility to prepare the two-level system in any superposition by controlling the sweep velocity. Transferring this finding to composite systems with controllable detuning, for example in circuit QED [19], allows to create entanglement between the subsystems dynamically, and hence serves the possibility to build quantum gates. In the second part of this thesis (Chapter 3), we discuss the implementation of LZ entangling gates in a semiconductor cavity QED system consisting of an excitonic two-level system in a single semiconductor quantum dot coupled to a cavity localized in the optical mode of a photonic resonator. The time-dependent detuning is provided by surface acoustic waves (SAWs), for which we consider various feasible pulse shapes. If the amplitude of the SAW is large, the driving can be linearized in the crossing region, i.e., where the detuning between the quantum dot and the cavity vanishes, and the dynamics can be described in terms of (LZ) transitions. Because entanglement relies on the phase coherence of the involved states, it is rather sensitive to decoherence caused by the interaction with the environment. In the case being considered, the main sources of decoherence are the incoherent decay of excitons because of the interaction with the substrate phonons and the photon loss of the cavity. We incorporate these effects in our theory using a master equation description and simulate the dynamics of the system numerically. Thereby, we show that, for experimentally demonstrated system parameters, entanglement with a

---

[1] The notion of the system parameters are changing slowly implies that the system has an intrinsic time scale to compare with. Such a timescale is usually associated with a discrete or gapped spectrum. However, it is possible to formulate the adiabatic theorem even for systems with gapless continuous spectrum [11].

persistence of the photon lifetime can be achieved and discuss directions to improve the performance of our proposal by using Fourier synthesized SAW pulses.

In the previous part, the lifetime of a photon was shorter than one period, so that we were able to ignore the periodicity of the driving and restricted on a single sweep through the avoided crossing. In general, however, a periodic driving may generate a variety of phenomena like interference [20], quantum chaos [21], localisation [22], geometrical phases [23] or even novel topological states of matter [24]. Sweeping the detuning with a time-periodic field results in a series of avoided crossing, where the wavefunction splits and recombines repeatedly. The phase accumulation between transitions may engender constructive or destructive interference and leads to Landau-Zener-Stueckelberg-Majorana (LZSM) interference patterns [20] demonstrated in various experiments with solid-state qubits [25–32]. Going beyond the mere demonstration of interference, LZSM interferometry can be employed as a tool to determine the dephasing time of a qubit. Here, one uses the fact that the Fourier transform of LZSM patterns exhibit arc structures which decay with a rate that depends on the decoherence rate of the qubit [33]. Comparing measured and computed decay rates, may allow one to characterize the coherence properties of the qubit and to determine the bath parameters experimentally [34]. In the third part of this thesis (Chapter 4), we investigate the influence of the bath coupling and the form of the driving shape on the LZSM patterns. Therefore, we study a periodically driven two-level system in contact with a bath of harmonic oscillators. Using a combination of Floquet theory and master equation techniques, we numerically calculate the steady state interference pattern, for transversal bath coupling (bath and driving couple to perpendicular coordinates), as well as for longitudinal bath coupling (bath and driving couple to the same coordinate) and discuss the interplay between driving and dissipation. Our numerical results are supported by an analytical treatment in terms of effective time-independent Bloch equations. In addition, the effect of a general system-bath coupling is discussed. Moreover, we show that, while the patterns in "energy space" are mainly governed by the bath coupling, the structures in Fourier space reflect the shape of the driving. We provide an analytical expression for these structures and determine their decay as function of the bath parameters.

# Chapter 2

# Employing Circuit QED to measure work fluctuations

In the last decades, the field of non-equilibrium statistical mechanics and thermodynamics has made considerable progress and stimulated the interest of more and more researchers from different communities, reaching from biological physics [35] to condensed matter physics [36], quantum optics [37] and quantum information theory [38]. One reason for this development was the discovery of fluctuation relations which are a generalization of the fluctuation-dissipation theorem to the regime beyond linear response [7, 39–41]. In fact, they characterize non-equilibrium phenomena to any order in the perturbative expansion and pose stringent conditions on the statistics of fluctuating quantities in non-equilibrium situations. Being rooted in the early works of Einstein [42, 43] and Sutherland [44] on Brownian motion, the theory of fluctuation relation developed gradually during the last century (see [7] for a historical overview). In general, a fluctuation theorem is a relation that is expressed as

$$\frac{p_{\mathrm{f}}(x)}{p_{\mathrm{b}}(-x)} = \exp(a(x-b)), \tag{2.1}$$

where $p_f(x)$ is the probability density function of a fluctuating quantity $x$ during a non-equilibrium thermodynamic (forward) transformation and $p_b(x)$ is the probability density function during the reversed (backward) transformation [7]. The constants $a$ and $b$ contain information about the equilibrium state before the non-equilibrium transformation is applied. If we assume $x$ to be a thermodynamic quantity like *work* or *entropy*, an equation of the form (2.1) can be interpreted as a generalization of the second law of thermodynamics [45]. In this chapter, we will focus on (quantum) work fluctuations and work fluctuation relations, where the random variable $x$ in Eq. (2.1) is the work performed by an external force on a quantum system. Other relations like entropy fluctuation theorems are discussed in [46]. Despite the considerable theoretical progress in the field of quantum (work) fluctuation relations [7], few experimental results have been obtained so far. This stems from the fact that the measuring the work in a quantum system requires at least two projective energy measurements which are experimentally challenging. In a recently published new approach, this issue is circumvented by determining the work indirectly using an interferometric scheme [8, 9]. This proposal uses an ancilla qubit to read out the characteristic function of work, and relies on a coupling between the system and the ancilla that is diagonal, state-dependent and highly tunable. The experimental realization of such a coupling, however, is in general far from trivial. In this chapter, we demonstrate that the scheme can be applied to a circuit QED setup. We show that, by introducing a second ancilla qubit and by going to the right parameter regime, the required coupling can be effectively realized using standard building blocks of circuit QED: charge qubits coupled to a transmission line. Our derivation is supported by numerical simulations. Moreover, we discuss that the interferometric scheme can applied to open quantum system even in the strong coupling regime, where little is konwn so far. We start with an introduction to quantum work fluctuation relations. The results of this chapter have been published previously in [47].

## 2.1 Quantum fluctuation relations

### 2.1.1 Work is not a quantum observable

Consider an arbitrary quantum system described by the unperturbed Hamiltonian $H_0$. Applying a time-dependent external force $\lambda_t$ which couples to the system coordinate $\mathcal{Q}$, leads to a perturbation $-\lambda_t\mathcal{Q}$ and results in the time-dependent Hamiltonian

$$H_{\rm S}(\lambda_t) = H_0 - \lambda_t\mathcal{Q} \tag{2.2}$$

obeying the (instantaneous) eigenvalue equation[1]

$$H_{\rm S}(\lambda_t)\left|\Psi_n^{\rm S}(\lambda_t)\right\rangle = E_n^{\rm S}(\lambda_t)\left|\Psi_n^{\rm S}(\lambda_t)\right\rangle . \tag{2.3}$$

The notation $H_{\rm S}(\lambda_t)$, $E_n^{\rm S}(\lambda_t)$, etc. is meant to indicate the dependence of the perturbed Hamiltonian and its eigenvalues and -states, respectively, on the time-dependent force $\lambda_t$. We use this convention in the whole chapter, however, in the following chapters we will only hallmark the time dependence. The instantaneous values of this force are specified by a function $\lambda$ which we will refer to as the force protocol. Depending on the specific shape of the protocol $\lambda$ the perturbation will alter the state of the system and lead to a shift of the systems eigenenergies $E_n^{\rm S}(\lambda_t)$. Hence, in general, the system's total

---

[1] For simplicity we consider non-degenerate eigenstates. In the degenerate case the following discussion stays valid, see [7].

energy will change. In the language of thermodynamics one calls the energy transferred to a system by means of an external force the *work* performed on the system. Let us assume that the system with Hamiltonian $H_\mathrm{S}(\lambda_0)$ is initially in a state described by a density matrix $\rho_\mathrm{S}(\lambda_0)$. In order to determine the energy of the system *before* the forcing we perform a projective energy measurement yielding one particular energy eigenvalue $E_n^\mathrm{S}(\lambda_0)$ of the initial Hamiltonian. Then, we evolve the system from $t = 0$ to $t = \tau$ by means of the time-dependent Hamiltonian (2.2), generating the time evolution operator $U_{\tau,0}^\mathrm{S}[\lambda] = \mathcal{T}\exp(-i\int_0^\tau dt H_\mathrm{S}(\lambda_t))$, with $\mathcal{T}\exp(\dots)$ being the time-ordered exponential ( [48], p. 143). The energy *after* the force protocol is obtained by again performing a projective energy measurement[2] leading to an energy eigenvalue $E_m^\mathrm{S}(\lambda_\tau)$. The work then is defined by the energy difference [7, 51]:

$$w := E_m^\mathrm{S}(\lambda_\tau) - E_n^\mathrm{S}(\lambda_0)^{3}. \tag{2.4}$$

From Eq. (2.4) and the previous discussion it follows that two measurements are needed in order to determine the work performed on a quantum system. This shows that “work” is a quantity that characterizes a process and not the state of a quantum system. As pointed out in [51] this implies that the work in a quantum system can not be represented by a Hermitian operator and hence is not a quantum observable.

### 2.1.2 The work probability distribution and its characteristic function

Randomness is a generic feature of quantum mechanics, and quantum theory in general allows only probabilistic statements about measurement outcomes. From the definition in Eq. (2.4), where the difference of two projective measurement outcomes appears, it immediately follows that the work in quantum mechanics is also a random quantity, with a probability density function $p[w;\lambda]$ which is presented in the following.

As stated before, the first measurement at $t = 0$ yields an energy eigenvalue $E_n(\lambda_0)$ with probability $p_n^0 = \mathrm{tr}[\Pi_n(\lambda_0)\rho_0]$, where $\Pi_n(\lambda_t) = |\Psi_n(\lambda_t)\rangle\langle\Psi_n(\lambda_t)|$. Assuming that the system is initially prepared in a canonical state

$$\rho_\mathrm{S}(\lambda_0) = e^{-\beta H_\mathrm{S}(\lambda_0)}/Z_\mathrm{S}(\lambda_0), \tag{2.5}$$

where $Z_\mathrm{S}(\lambda_t) = \mathrm{tr}[e^{-\beta H_\mathrm{S}(\lambda_t)}]$ is the partition function, we obtain:

$$p_n^0 = e^{-\beta E_n^\mathrm{S}(\lambda_0)}/Z_\mathrm{S}(\lambda_0). \tag{2.6}$$

---

[2] The consequences of the use of generalized instead of projective measurements have been discussed recently in [49, 50].

[3] Eq. (2.4) represents the quantum version of the so called classical inclusive work. Alternatively, one can introduce the quantum exclusive work $w_0 = e_m - e_n$, where $e_m$ and $e_n$ are eigenvalues of the unperturbed Hamiltonian $H_0$ [7].

According to von Neumann's projection postulate [52], after the first measurement the system is found in the state

$$\rho_n^0 = \Pi_n(\lambda_0)\rho_{\mathrm{S}}(\lambda_0)\Pi_n(\lambda_0)/p_n^0. \tag{2.7}$$

Now we propagate the system until time $\tau$. Assuming that the system is thermally isolated for $t \leq 0$ this time evolution is determined by the unitary operator $U^{\mathrm{S}}_{t,0}[\lambda]$, so that the system evolves according to $\rho_n(t) = U^{\mathrm{S}}_{t,0}[\lambda]\rho_n^0(U^{\mathrm{S}}_{t,0}[\lambda])^\dagger$. Here the index $n$ is used to stress that the time evolution explicitly depends on the outcome of the first energy measurement. The second energy measurement at time $\tau$ then yields the energy eigenvalue $E^{\mathrm{S}}_m(\lambda_\tau)$ with probability

$$p_{m|n}[\lambda] = \mathrm{tr}[\Pi_m(\lambda)\rho_n(\tau)]. \tag{2.8}$$

The conditional probability $p_{m|n}[\lambda]$ quantifies the probability for the transition $|\Psi_n(\lambda_0)\rangle \to |\Psi_m(\lambda_\tau)\rangle$. For sufficiently slow driving, the adiabatic theorem [12,13] holds, and the system stays in the instantaneous eigenstate $|\Psi_n(\lambda_t)\rangle$, $\forall\ t$, i.e. we get $p_{m|n}[\lambda] = \delta_{n,m}$, with $\delta_{n,m}$ being the Kronecker delta. In this case, the work is given by the shift of the eigenenergy $E^{\mathrm{S}}_n(\lambda_t)$. However, for finite velocities the driving will induce non-adiabatic transitions and the system will end up in a different eigenstate. Finally, the probability density function for having performed the work $w$ is given by [7]:

$$p[w;\lambda] := \sum_{m,n} \delta(w - [E_m(\lambda_\tau) - E_n(\lambda_0)])p_{m|n}[\lambda]p_n^0. \tag{2.9}$$

An important quantity in probability theory is the characteristic function of a probability density function, defined as its Fourier transform. Thus, the characteristic function of work $G[u;\lambda]$ is given by

$$G[u;\lambda] = \int dw e^{iuw} p[w;\lambda]. \tag{2.10}$$

Since the Fourier transform is a bijection, no information gets lost because of this operation and $G[u;\lambda]$ contains the full statistical information about the work $w$ performed by the external force $\lambda_t$. Inserting Eq. (2.9) into the expression (2.10) and evaluating the integral, yields [51]

$$\begin{aligned} G[u;\lambda] =& \langle e^{iu\tilde{H}_S(\lambda_\tau)} e^{-iuH_S(\lambda_0)}\rangle \\ =& \langle (e^{-iuH_S(\lambda_\tau)} U^S_{\tau,0}[\lambda])^\dagger U^S_{\tau,0}[\lambda] e^{-iuH_S(\lambda_0)}\rangle, \end{aligned} \tag{2.11}$$

where $\tilde{H}_S(\lambda_\tau) = (U^S_{\tau,0}[\lambda])^\dagger H_S(\lambda_\tau) U^S_{\tau,0}[\lambda]$ is the Hamiltonian in the Heisenberg picture and $\langle \dots \rangle = \mathrm{tr}[\dots \rho_{\mathrm{S}}(\lambda_0)]$ the system average. Equation (2.11) shows that the characteristic function of work can be expressed as two-time correlation function. Later we will see that this correlation function is an experimentally accessible quantity.

### 2.1.3 The quantum fluctuation theorem

In this subsection, we introduce the quantum Crooks fluctuation theorem [7, 53]. This theorem holds under very general conditions and exactly characterizes systems far from equilibrium. In order to derive it, two assumption have to be made: first, the system has to be initially in a Gibbs state, defined in Eq. (2.5), and second, the time evolution must by be time-reversal symmetric [7], i.e.,

$$\left(U^{\mathrm{S}}_{\tau,0}[\lambda]\right)^{\dagger} = U^{\mathrm{S}}_{0,\tau}[\lambda] = \Theta^{\dagger} U^{\mathrm{S}}_{\tau,0}[\tilde{\lambda}]\Theta, \tag{2.12}$$

where $\Theta$ is the time-reversal operator ( [54], p. 669), and $\tilde{\lambda}$ the time reversed protocol. Starting from Eq. (2.11) one is able to derive the relation [7, 53]

$$Z_{\mathrm{S}}(\lambda_0)G[u;\lambda] = Z_{\mathrm{S}}(\lambda_\tau)G[i\beta - u;\tilde{\lambda}], \tag{2.13}$$

using the unitarity of the time evolution and the fact that the characteristic function is analytic [53]. Applying the inverse Fourier transform to Eq. (2.13) yields the *quantum work fluctuation theorem*, also called (quantum) *Tasaki-Crooks relation*:

$$\frac{p[w,\lambda]}{p[-w,\widetilde{\lambda}]} = e^{\beta(w-\Delta F_{\mathrm{S}})}, \tag{2.14}$$

where $\Delta F_{\mathrm{S}} = F_{\mathrm{S}}(\lambda_\tau) - F_{\mathrm{S}}(\lambda_0)$ is the change of the free energy $F_{\mathrm{S}}(\lambda_t) = -\beta^{-1}Z_S(\lambda_t)$. Equation (2.14) states that it is exponentially more probable to perform the work $w$ by the force protocol $\lambda$ than to gain the work $w$ by the reversed protocol. Interestingly, Eq. (2.14) also connects the equilibrium quantity $\Delta F_{\mathrm{S}}$ with the work probability density function $p[w;\lambda]$ characterizing non-equilibrium processes.

Multiplying Eq. (2.14) by $p[-w,\tilde{\lambda}]$ and integrating over $w$ directly leads to the *quantum Jarzynski equality*:

$$\langle e^{-\beta w}\rangle_\lambda = e^{-\beta \Delta F_{\mathrm{S}}}, \tag{2.15}$$

with $\langle \dots \rangle_\lambda = \int dw \dots p[w;\lambda]$ being the average regarding the work probability density function. The quantum fluctuation theorem (2.14) as well as the quantum Jarzynski equality (2.15) are formally equivalent to their classical counterparts [7]. Note that in the quantum case it is important to determine the work by projective measurements. For generalized measurements the formal equivalence between the quantum and the classical case can only be established if the measurements are error free and the transition probabilities $p_{n|m}[\lambda]$ satisfy a generalized detailed balance condition [49, 50]. Recently, a different kind of quantum work fluctuation theorems was derived without introducing any measurements at all [55].

Classically, the fluctuation theorem in Eq. (2.14) has been tested in a single molecule stretching experiment. Moreover, the experimentalists were able to use the fluctuation theorem in order to determine the free energy landscape of the molecule folding [56, 57]. In contrast, the quantum fluctuation theorem and the quantum Jarzynski equality, respectively, have not been verified yet. The problem lies in the fact that, in the quantum regime, projective measurements before and after the force protocol are needed. Indeed, there has been an experimental proposal for an ion trap experiment based on a two measurement scheme [58], but so far it has not been realized. Recently, a new approach to determine the work probability density function has been introduced by [8, 9]. This approach avoids projective measurements by using an interferometric scheme allowing to reconstruct the characteristic function of work by reading out an ancilla qubit coupled to the system. Here, the experimental challenge is to realize the proposed tunable coupling between system and ancilla. We will discuss this in greater detail in the next chapter, after the following example.

### 2.1.4 Example: The parametrically driven oscillator

To illustrate the rather formal discussion before, we consider the parametrically driven oscillator, whose frequency changes in time according to $\omega^2(t) = \omega^2 - 4\omega\lambda_t$. Its Hamiltonian reads

$$\begin{aligned} H_S(\lambda_t) &= p^2/2m + m(\omega^2 - 4\omega\lambda_t)x^2/2 \\ &= \hbar\omega(a^\dagger a + 1/2) - \hbar\lambda_t(a^\dagger + a)^2, \end{aligned} \tag{2.16}$$

where $a = x\sqrt{m\omega/2\hbar} + ip\sqrt{1/2m\omega\hbar}$ and $a^\dagger = x\sqrt{m\omega/2\hbar} - ip\sqrt{1/2m\omega\hbar}$ are the usual shift operators. The statistics of work of the parametrically driven oscillator was first discussed in [59]. Fig. 2.1 shows the real (left) and imaginary (middle) part of the characteristic function of work and the work probability distribution (right), following from Eq. (2.16) with a linear driving $\omega(t) = (1 + vt)\omega$ from $t = 0$ to $t = \tau = 2\pi/\omega$. Comparing the real and imaginary parts of the characteristic functions one finds that in the slow driving case ($v = 0.1$) both, the real and the imaginary part show periodic behavior, while in the case of a faster driving ($v = 0.5$) the oscillations are more complicated. The reason for this is that in the first case only a few transitions are induced by the driving, so that the system stays close to equilibrium. As a consequence, the work probability density only contains a few peaks which correspond to the frequency components of the characteristic function. In the latter, fast driving case the system is pushed out of equilibrium, leading to complex system dynamics with many transitions

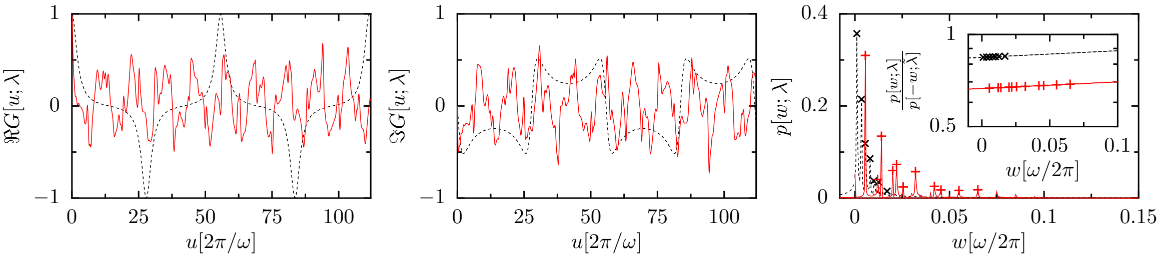

FIGURE 2.1: Work statistics of a parametrically driven oscillator, for $v = 0.1$ (black dashed line, cross symbol) and $v = 0.5$ (red solid line, plus symbol). Left: Real part of the characteristic function. Middle: Imaginary part of the characteristic function. Inset: Check of the fluctuation theorem.

between different levels. This reflects itself in many non-equidistant peaks in the work probability density and the wild oscillations in the characteristic function. Despite the differences both situation fulfill the fluctuation theorem (2.14) (see inset of Fig. 2.1).

## 2.2 Interferometric reconstruction of the characteristic function of work

### 2.2.1 The scheme

In this section, we review the method for extracting the statistics of work that has been put forward by Dorner *et al.* [8] and Mazzola *et al.* [9]. This method uses an interferometric scheme in order to specify the characteristic function of work.

Imagine one wants to determine the statistics of work in a system described by the Hamiltonian (2.2). Instead of studying the system (S) alone, the interferometric scheme proposes to introduce an ancilla qubit (A) coupled to (S) according to the Hamiltonian:

$$H_{\mathrm{S+A}} = \frac{\hbar\varepsilon}{2}\sigma_z + H_0 - (\lambda_t^e(u)\Pi_e + \lambda_t^g(u)\Pi_g)\mathcal{Q}, \tag{2.17}$$

where $\sigma_z = \Pi_e - \Pi_g$ is the usual Pauli matrix, $\Pi_{e,g} = |e,g\rangle\langle e,g|$ is the projector onto the excited and ground state, $|e\rangle$ and $|g\rangle$, respectively, and $\lambda_t^{e,g}(u)$ are two driving protocols of duration $T = \tau + u$, giving the coupling between system and the ancilla states. The first term in Eq. (2.17) represents the free Hamiltonian of the ancilla, the second term the free Hamiltonian of the system and the third term describes the coupling between the system and the ancilla. Note that the system-ancilla coupling is diagonal, i.e. the interaction induces no transition in the ancilla qubit. Moreover, the couplings to the qubit's excited and ground states ,$\lambda_t^{e,g}(u)$, have are controllable independently. Besides their dependence on time $t$, these couplings additionally depend on the parameter $u$ whose role will become clear later. Because the system-ancilla coupling commutes with the free ancilla Hamiltonian $H_{\mathrm{A}} = \hbar\varepsilon\sigma_z/2$, the evolution $U_{t,0}^{\mathrm{S+A}}[\lambda^e, \lambda^g]$ of S + A generated

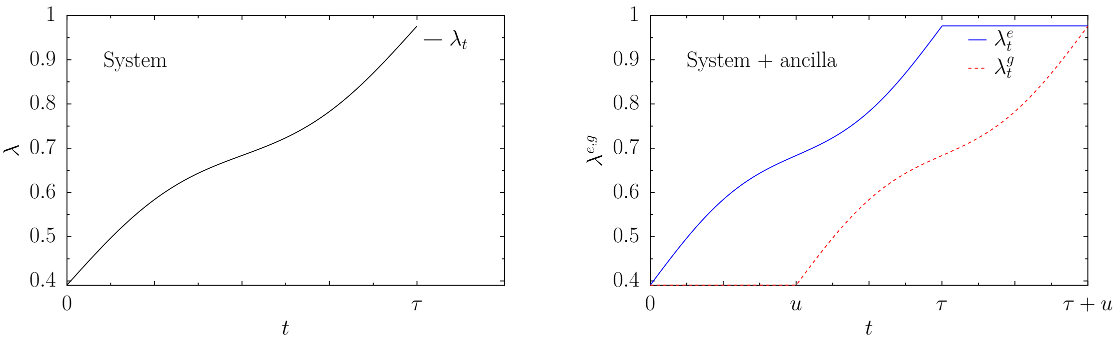

FIGURE 2.2: Exemplary sketch of the force protocol $\lambda_t$ (left) and the associated time-dependent system ancilla couplings $\lambda_t^{e,g}(u)$ (right) as a function of time. Compare with the definition of $\lambda_t^{e,g}(u)$ in Eq. (2.19).

by the drivings $\lambda_t^e(u)$ and $\lambda_t^g(u)$ is block diagonal in the basis $\{|e\rangle, |g\rangle\}$

$$U_{t,0}^{\mathrm{S+A}}[\lambda^e, \lambda^g] = \begin{pmatrix} e^{-i\varepsilon t/2\hbar} U_{t,0}^{\mathrm{S}}[\lambda^e] & 0 \\ 0 & e^{i\varepsilon t/2\hbar} U_{t,0}^{\mathrm{S}}[\lambda^g] \end{pmatrix}. \tag{2.18}$$

For a given force protocol $\lambda$, starting at time $t=0$ and ending at $t=\tau$, we choose the couplings $\lambda_t^{e,g}(u)$ to be

$$\lambda_t^e(u) = \begin{cases} \lambda_t & \text{for } t \in [0,\tau] \\ \lambda_\tau & \text{for } t \in [\tau, \tau+u] \end{cases}, \quad \lambda_t^g(u) = \begin{cases} \lambda_0 & \text{for } t \in [0,u] \\ \lambda_{t-u} & \text{for } t \in [u, \tau+u] \end{cases}, \tag{2.19}$$

as sketched in Fig. 2.2. Hence, the two independent protocols in Eq. (2.19) are of duration $T = \tau + u$. The evolution operator, propagating from $t=0$ to $t=\tau+u$ is given by

$$U_{T,0}^{S+A}[\lambda^e, \lambda^g] = \begin{pmatrix} e^{-i\varepsilon(\tau+u)/2\hbar} e^{-iuH_{\mathrm{S}}(\lambda_\tau)/\hbar} U_{\tau,0}^{\mathrm{S}}[\lambda] & 0 \\ 0 & e^{i\varepsilon(\tau+u)/2\hbar} U_{\tau,0}^{\mathrm{S}}[\lambda] e^{-iuH_{\mathrm{S}}(\lambda_0)/\hbar} \end{pmatrix}. \tag{2.20}$$

It contains the operators $U_{\tau,0}^{\mathrm{S}}[\lambda] e^{-iuH_{\mathrm{S}}(\lambda_0)/\hbar}$ and $e^{-iuH_{\mathrm{S}}(\lambda_\tau)/\hbar} U_{\tau,0}^{\mathrm{S}}[\lambda]$ which also appear in the expression of the characteristic function, Eq. (2.11).

Inspired by Ramsey interferometry, the idea is to prepare the ancilla in a superposition of excited and ground states, so that the two time evolutions interfere, and the wanted information is encoded in the state of the ancilla at the final time $T = \tau + u$. This is achieved by the following protocol [8, 9]:

1. Prepare the compound system in the state $\rho_{\mathrm{S+A}} = |g\rangle\langle g| \otimes \rho_{\mathrm{S}}(\lambda_0)$ at $t < 0$, with $\rho_{\mathrm{S}}(\lambda_0)$ given by Eq. (2.5).
2. Perform a Hadamard operation $\sigma_H = (\sigma_x + \sigma_z)/\sqrt{2}$ on the ancilla at $t = 0$.
3. Let the S+A system evolve for a time $\tau + u$, according to $U_{T,0}^{\mathrm{S+A}}[\lambda]$.

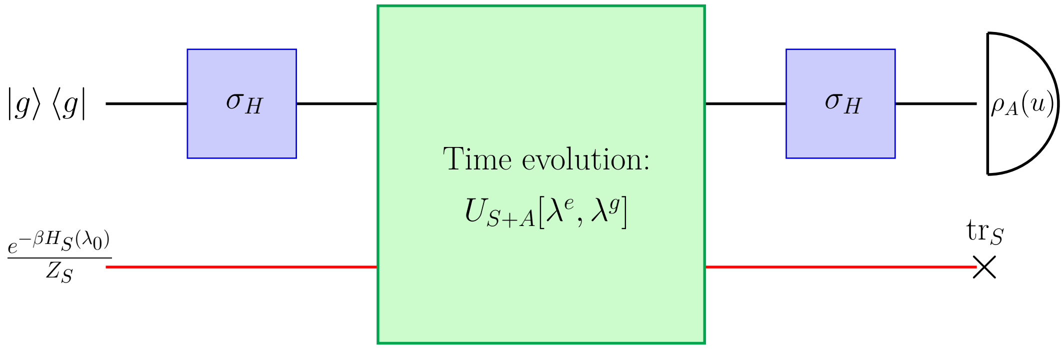

FIGURE 2.3: The *interferometric scheme*, depicted as succession of gate operations on system and ancilla, starting with the preparation of S and A on the left and ending with the measurement of the qubit state $\rho_A(u)$ on the right.

4. Perform a Hadamard operation $\sigma_H$ on the ancilla at $t = T = \tau + u$.

A graphical representation of this scheme is given in Fig. 2.3. The purpose of the first Hadamard transformation is to create a superposition of the up and down states. The second Hadamard recombines the entries of the ancilla density matrix at time $T = \tau + u$ and, as such, is not strictly necessary. After the protocol, the ancilla is described by the reduced density matrix

$$\rho_A(u) = \mathrm{tr}_S \sigma_H U^{S+A}_{T,0}[\lambda^e, \lambda^g] \sigma_H \rho_{S+A} \sigma_H \left(U^{S+A}_{T,0}[\lambda^e, \lambda^g]\right)^\dagger \sigma_H \tag{2.21}$$

$$= \frac{1}{2}\left(1 - [\Re L(u)]\sigma_z + [\Im L(u)]\sigma_y\right), \tag{2.22}$$

where $\Re$ and $\Im$ denote real and imaginary parts, $\mathrm{tr}_S$ is the trace over the system's Hilbert space, and

$$L(u) = e^{-i\varepsilon(\tau+u)/\hbar} G[u, \lambda]. \tag{2.23}$$

Thus, by state tomography of the ancilla density matrix at time $t = T = \tau + u$, one can recover the value of the characteristic function $G[u, \lambda]$ at $u$. By repeating the whole procedure for various values of $u \in (0, \infty)$, one obtains $G[u, \lambda]$ on the positive real axis. Using $G[-u, \lambda] = G^*[u, \lambda]$ one obtains $G[u, \lambda]$ on the whole real axis, and then, by inverse Fourier transform the work statistics $p[w, \lambda]$. In practice, one can sample the characteristic function only in a finite domain. This in turn limits the accuracy with which the work probability distribution function can be resolved. Note also that the diagonal and state-dependent coupling in Eq. (2.17) can often be realized only approximately. The aim of our work is to apply the aforementioned scheme to a real physical system, to be more precise, to a system built of superconducting circuits. In the next section, we will give a short introduction to superconducting circuits and circuit quantum electrodynamics, before we discuss how to employ such systems for measuring

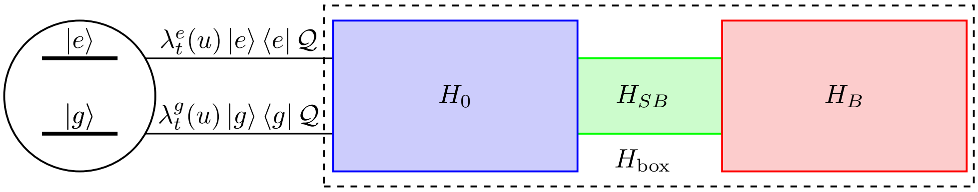

Figure 2.4: The interferometric scheme in a general open quantum system: Choosing $\lambda_t^e(u)$ and $\lambda_t^g(u)$ as in (2.19), the ancilla qubit (black circle on the left) accounts for the work performed on the whole "black-box" system (dashed rectangle) $H_{\text{box}} = H_0 + H_{\text{SB}} + H_{\text{B}}$ that it is coupled to. Hence, one is able to reconstruct the characteristic function of work in an open system with arbitrary system-bath coupling strength.

work statistics. In the following subsection we discuss the possibility to extend the interferometric scheme to open quantum systems.

### 2.2.2 Work statistics of arbitrary open quantum systems

As mentioned above, the primary advantage of the interferometric scheme of Dorner *et al.* [8] and Mazzola *et al.* [9] is that it avoids projective measurements on the system of interest $H_{\text{S}}$ by replacing them with state tomography on the ancilla. This has a very important consequence in regard to the possibility of experimentally testing fluctuation theorems in open quantum systems with arbitrarily strong coupling to a thermal environment [60]

$$H_{\text{S+B}}(\lambda_t) = H_{\text{S}}(\lambda_t) + H_{\text{B}} + H_{\text{SB}}\,. \tag{2.24}$$

Here, $H_{\text{B}}$ is the thermal bath Hamiltonian and $H_{\text{SB}}$ the system-bath coupling Hamiltonian with an arbitrary strong coupling. Nevertheless, the fluctuation theorem continues to hold unaltered in this case [60], because when driving the system $S$, part of the injected energy may flow to the bath B and in the SB interaction. Thus the work spent to drive the system is given by the change in the S + B energy: $w = E_m^{\text{S+B}}(\lambda_\tau) - E_n^{\text{S+B}}(\lambda_0)$, where $E_n^{\text{S+B}}(\lambda_t)$ are the instantaneous eigenvalues of the system-bath Hamiltonian $H_{\text{S+B}}(\lambda_t)$ at time $t$. Since the total system S + B, described by the Hamiltonian in Eq. (2.24), is a closed system with an unitary time evolution, by assuming a thermal initial state

$$\rho_{\text{S+B}} = \frac{e^{-\beta H_{\text{S+B}}(\lambda_0)}}{Z_{\text{S+B}}(\lambda_0)}\,, \tag{2.25}$$

the ordinary fluctuation relation applies $p[w,\lambda]/p[-w,\widetilde{\lambda}] = e^{\beta(w-\Delta F_{S+B})}$ independent of the coupling strength. Here, $Z_{\text{S+B}}$ and $\Delta F_{\text{S+B}}$ are the partition function and, respectively, the free energy difference in the total S + B system. Using the expression of the free energy of an arbitrary open quantum system [61] $F_{\text{S}}(\lambda_t) = F_{\text{S+B}}(\lambda_t) - F_{\text{B}}^0$ (where $F_{\text{B}}^0 = -\beta^{-1}\ln \mathrm{tr}_{\text{B}} e^{-\beta H_{\text{B}}}$, and $F_{\text{S+B}}(\lambda_t) = -\beta^{-1}\ln \mathrm{tr}_{\text{S+B}} e^{-\beta H_{\text{S+B}}(\lambda_t)}$), one immediately sees that $\Delta F_{\text{S+B}} = F_{\text{S+B}}(\lambda_t) - F_{\text{S+B}}(\lambda_0) = F_{\text{S}}(\lambda_t) - F_{\text{S}}(\lambda_0) = \Delta F_{\text{S}}$. Thus the fluctuation theorem reads also in the case of an arbitrary open quantum system [60]

$$\frac{p[w,\lambda]}{p[-w,\widetilde{\lambda}]} = e^{\beta(w-\Delta F_{\mathrm{S}})}, \tag{2.26}$$

i.e., it is formally agrees with Eq. (2.14). This result is the quantum version of an analogous result obtained by Jarzynski for classical systems [62]. In contrast to classical systems, in the quantum case, in principle, one should perform two projective measurements of the *total* Hamiltonian $H_{\mathrm{S+B}}$. Making a projective measurement on S alone is already a challenging task in many experimental set-ups; making a projective measurement of $\mathrm{S+B}$ seems much more difficult, if not impossible. The interferometric scheme may be effective in overcoming this problem. If now the open system is coupled to the ancilla which, in turn, has no direct contact to the environment, the $\mathrm{S+B+A}$ Hamiltonian reads

$$H_{\mathrm{S+B+A}} = \frac{\hbar\varepsilon}{2}\sigma_z + H_0 + H_{\mathrm{B}} + H_{\mathrm{SB}} - (\lambda_t^e\Pi_e + \lambda_t^g\Pi_g)\mathcal{Q}. \tag{2.27}$$

Implementing the same interferometric scheme as in Sec. 2.2.1 with the initial state being $\Pi_g\rho_{\mathrm{S+B}}$ then allows one to measure the characteristic function of the open system $H_{\mathrm{S+B}}(\lambda_t)$ (see Fig. 2.4). Thus, if the ancilla is well isolated, the interferometric approach provides, access to the work distribution of arbitrary open as well as closed non-equilibrium quantum systems.

Most remarkably, our present discussion highlights that by using the interferometric scheme of Dorner *et al.* [8] and Mazzola *et al.* [9], deviations from the fluctuation theorem are expected only as a consequence of thermal noise on the ancilla $A$. Thermal noise on the system $S$ may, by contrast, affect the statistics of work itself, but not the validity of the fluctuation relations.

We emphasize that the fluctuation theorem for open quantum systems described in this section is fully general and exact. In particular, it does not require the interaction $H_{\mathrm{SB}}$ to be weak nor the initial $\mathrm{S+B}$ state to be uncorrelated. Quite on the contrary, in case of strong coupling the initial state $\rho_{\mathrm{S+B}}$ contains correlations, and the subsequent evolution of the reduced system density matrix needs not be described by completely positive maps [63], nor has to be Markovian. In this regard newly introduced definitions of characteristic functions for open quantum systems in terms of the reduced system dynamics [64–67] must be regarded as approximate expressions whose validity is in general not guaranteed, and whose main object is generally not the work, i.e., the change in energy of $\mathrm{S+B}$ but some other quantity that pertains to the system S only.

## 2.3 An introduction to circuit quantum electrodynamics

### 2.3.1 Superconductivity and Josephson effect

In this section, we give a short introduction to the field of circuit quantum electrodynamics and superconducting quantum circuits. Although the typical size of these system is of the order of micrometers, they obey the rules of quantum mechanics at low temperatures. The reason for this macroscopic quantum behavior is the superconducting phase transition appearing at a critical temperature $T_c$ of a few milli-Kelvin. Below this temperature, the electrons in a type-I-superconducting material like aluminium or niobium condensate into stable Cooper-pairs which, because of their bosonic nature, fill the same ground state [68]. As a consequence, the ground state becomes macroscopically occupied and can be described by the macroscopic wave function

$$\Psi(\mathbf{r}) = |\Psi_0| e^{i\varphi(\mathbf{r})}, \tag{2.28}$$

with $|\Psi_0|^2$ being the average density of Cooper-pairs and $\varphi(\mathbf{r})$ the collective spatial phase. Equation (2.28) has first been postulated in a phenomenological approach to superconductivity known as Ginzburg-Landau theory [69]. Later the Bardeen-Cooper-Schrieffer (BCS) theory [70, 71] provided a microscopic theory of superconductivity[4], identifying the formation of Cooper-pairs as a result of the electron-phonon interaction. Interestingly, this interaction which is responsible for dissipative effects in first order leads to an attractive net interaction between pairs of electrons at second order and hence is responsible for the coherent and dissipationless behavior at low temperatures [36].

In 1962, Josephson investigated the problem of Cooper-pair tunneling between two superconductors coupled via a week isolating link, nowadays called Josephson junction [72]. He showed that by applying a weak external voltage a dissipationless supercurrent flows through the junction which can be expressed by the equation (first Josephson equation)

$$I_s = I_c \sin(\Delta\varphi). \tag{2.29}$$

Here, $I_c$ is the critical current depending on the barrier thickness and the size of the superconducting gap[5] and $\Delta\varphi$ is the phase difference between the superconducting wave functions (2.28) on both sides of the barrier. The phase difference obeys the second Josephson equation

$$\frac{d\Delta\varphi}{dt} = \frac{2\pi U(t)}{\Phi_0}, \tag{2.30}$$

where $U(t)$ is the voltage drop across the barrier and $\Phi_0 = h/2e$ the magnetic flux quantum. Using the Eqs. (2.29) and (2.30) the potential energy, i.e. the coupling energy

---

[4] To be precise, the BCS theory describes the so called type-I-superconductivity. A full theoretical understanding of the type-II-superconductivity appearing at high temperature is still missing.

[5] By applying an magnetic field, $I_c$ can be manipulated externally.

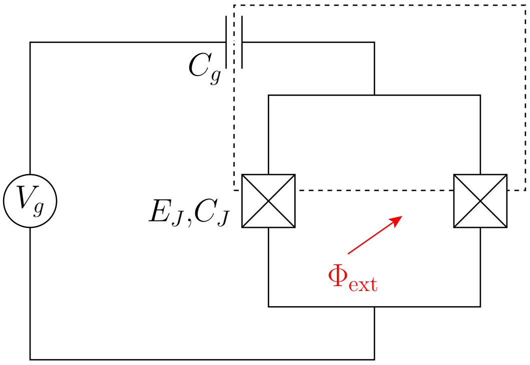

FIGURE 2.5: Cooper-pair box with tunable Josephson coupling. Cooper-pairs can tunnel through the two Josephson junctions (crossed square), onto the superconducting island (dashed rectangle) representing a charge qubit (see Eq. (2.36)). The background charge $N_g$ and hence the qubits level splitting $E_{\text{el}}$ can be tuned via the gate voltage $V_g$, while the Josephson energy $E_\text{J}$ and therefore the qubit splitting is controlled via the external magnetic flux $\Phi_{\text{ext}}$ through the loop structure.

between the superconductors, results in

$$V(t) = \int dt' \; I(t')U(t') = -E_\text{J}\cos(\Delta\varphi(t)), \tag{2.31}$$

where we introduced the Josephson energy $E_\text{J} = \Phi_0 I_\text{c}/2\pi$. Since real superconductors posses a non vanishing capacitance $C_\text{J}$, an additional charging energy per Cooper pair of $E_\text{C} = e^2/2C_\text{J}$ has to be taken into account. This energy corresponds to the kinetic energy of the junction. Up to now, the description of the Josephson junction was fully classical. Using quantum circuit theory [73, 74], the quantized Hamiltonian operator of the junction can de expressed as

$$H_{\text{JJ}} = 4E_\text{C}\hat{N}^2 - E_\text{J}\cos(\Delta\hat{\varphi}), \tag{2.32}$$

where we introduced the number operator $\hat{N}$, whose eigenvalues correspond to the number of excess Cooper-pairs on the junction capacitance, and the phase operator $\Delta\hat{\varphi}$ having continuous eigenvalues on the unit circle $[0, 2\pi]$. The operators represent conjugate variables obeying the commutation relation

$$[e^{\Delta\hat{\varphi}}, \hat{N}] = -e^{i\Delta\hat{\varphi}}. \tag{2.33}$$

From Eq. (2.32) it follow that the Josephson junction introduces a non-linear, and at the same time non-dissipative element in a superconducting circuit. This nonlinearity is crucial since it leads to a discrete, strongly anharmonic spectrum providing energy levels suitable for a qubit [75].

### 2.3.2 The Cooper-pair box

The simplest Josephson junction qubit is the so called Cooper-pair box (CPB). It consists of a small superconducting island connected to a superconducting reservoir by a tunnel junction [76]. Sometimes it is useful to introduce a second junction in a loop configuration (see Fig. 2.5), because this allows to tune the Josephson energy $E_J \to E_J \cos(2\pi\Phi_x/\Phi_0)$ with an external flux $\Phi_x$. The Hamiltonian of the CPB reads (compare with Eq. (2.32))

$$H_{\text{CPB}} = 4E_C(\hat{N} - N_g)^2 - E_J \cos(\Delta\hat{\varphi}), \tag{2.34}$$

with the gate charge $N_g = C_g V_g/2e$ accounting for the gate voltage which allows to control the number of excess Cooper-pairs[6] $N$ on the island. Operating in the charge regime, where $E_C \gg E_J$, it is convenient to express the Hamiltonian in the charge basis, i.e. the eigenbasis of the operator $\hat{N}$. This yields [76]

$$H_{\text{CPB}} = \sum_n 4E_C\big(N - N_g\big)^2 \left|N\right\rangle \left\langle N\right| - \frac{1}{2}E_J(\left|N\right\rangle \left\langle N+1\right| + \left|N+1\right\rangle \left\langle N\right|)\big). \tag{2.35}$$

Near the charge degeneracy point, where $N_g$ is approximately half integer, the Hamiltonian (2.34) is dominated by the second term and two adjacent energy eigenstates are close to each other (forming an avoided crossing). Since in this region the other energy levels are far away, the system effectively reduces to a two level system. In the charge basis, i.e. $|g\rangle = N_0, |e\rangle = |N_0 + 1\rangle$, where $N_0$ corresponds to the (unknown) number of Cooper pairs on the island, the Hamiltonian (2.34) reads

$$H_{\text{qb}} = -\frac{E_{\text{el}}}{2}\sigma_z - \frac{E_J}{2}\sigma_x. \tag{2.36}$$

The Cooper-pair box is the simplest realization of a charge qubit in superconducting circuits. Other implementations like flux qubits or phase-based qubits are reviewed in [76–78].

### 2.3.3 A charge qubit coupled to a transmission line resonator

One big advantage of superconducting qubits is that they can be integrated on a chip and combined with other circuit elements [75, 76]. In particular, they can be coupled to a transmission line resonator which can be modeled as an harmonic oscillator [75, 79]. Hence, a line resonator can be seen as an electric analogue of an optical cavity studied in quantum optics and cavity quantum electrodynamics [80]. Using the bosonic creation

---

[6] eigenvalue of the operator $\hat{N}$

and annihilation operators $a$ and $a^\dagger$ the quantized Hamiltonian of the resonator reads

$$H_{\text{res}} = \hbar\Big(\omega a^\dagger a + \frac{1}{2}\Big), \tag{2.37}$$

where $\omega = \pi/l\sqrt{L_x C_x}$ is the resonance frequency of the resonator, with $l$ being its length and $L_x$ and $C_x$ the inductance and, the capacitance per unit length, respectively. In (2.37) we restricted us on a single resonator mode, neglecting the fact that in general the resonator is described by a (infinite) sum of modes [75]. The resonator couples to the Cooper-pair box via the capacitance $C_c$, leading to the interaction Hamiltonian [79]

$$H_{\text{int}}^{\text{res}} = 2e\frac{C_c U_0}{C_g + C_J}(\sigma_z - N_g)(a + a^\dagger), \tag{2.38}$$

with $U_0 = \sqrt{\hbar\omega/C}$ and $C$ being the inductance of the resonator. At the charge degeneracy point and in the eigenbasis of the qubit the total system $H_{\text{qb}} + H_{\text{res}} + H_{\text{int}}^{\text{res}}$ reduces to the Rabi Hamiltonian [81,82]

$$H_{\text{Rabi}} = \frac{\hbar\varepsilon}{2}\sigma_z + \hbar\omega a^\dagger a + \hbar g\sigma_x(a^\dagger + a) \tag{2.39}$$

with coupling $g = eC_cU_0/(C_g + C_J)$. It describes a two-level system coupled to a harmonic oscillator with arbitrary coupling strength $g$. Especially, in the field of circuit QED the last point gets more and more important, because in recent times one has been able to reach the ultra-strong coupling regime [83] experimentally. Note that despite its simplicity the integrability of the Hamiltonian (2.39) has only been shown recently [82]. While the transmission line often is used to read out the state of a qubit [84,85], we will use it as the “system” and detect the work performed on it using the qubit.

## 2.4 Measuring quantum work fluctuations in circuit QED

We want to use the interferometric scheme to access the work statistics of the parametrically driven quantum oscillator (2.16), discussed in Sec. 2.1.4. To implement this Hamiltonian we consider the circuit QED setup, as in the previous section, where a qubit is coupled to a single mode $\omega$ of a line resonator. The qubit-oscillator system is described by the Rabi Hamiltonian (2.39). Note that this Hamiltonian is generally not of the type (2.17) needed to implement the interferometric scheme. First, the qubit-system interaction does not commute with the free qubit Hamiltonian $\hbar\varepsilon\sigma_z/2$. Second, the interaction term is linear in $(a^\dagger + a)$, whereas we want to implement an interaction quadratic in $(a^\dagger + a)$. Third, the setup does not provide the possibility to control the interaction $g$ in time, because $g$ is fixed by the geometry of the device. Setups allowing the control of $g$ have been studied only theoretically so far [86]. However, using a setup as in Fig. 2.5, one can relatively easily control the qubit splitting $\varepsilon$ by changing

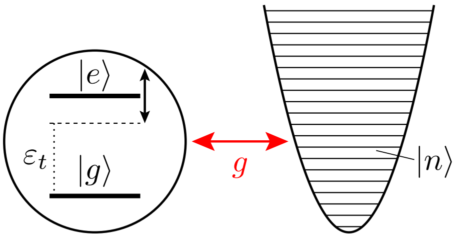

FIGURE 2.6: A qubit-oscillator system in the “soft mode” regime, where the conditions (2.40) and (2.43) are fulfilled: The variation of the level splitting $\varepsilon_t$ is too small to induce transitions between the qubit states. However, since $\dot{\varepsilon}_t/\varepsilon_t$ is comparable to the oscillator splitting $\omega$ the latter gets driven out of equilibrium.

the external flux $\Phi_{\text{ext}}$. In the following, we show that, by going to the right parameter regime, a time-dependent level splitting leads to a time-dependent effective coupling, so that the coupling can effectively be controlled by changing $\Phi_{\text{ext}}$.

### 2.4.1 Qubit-oscillator system with time-dependent coupling

In order to achieve a time-dependent and diagonal coupling between the resonator and the qubit, we consider a time-dependent qubit splitting $\varepsilon_t$ and work in a regime where the coupling $g$ and the oscillator frequency $\omega$ are small (see Fig. 2.6):

$$g \simeq \omega \ll \varepsilon_t \,. \tag{2.40}$$

Applying the time-dependent unitary transformation

$$U(t) = e^{ig(a^\dagger + a)\sigma_y/\varepsilon_t}, \tag{2.41}$$

and neglecting terms of order larger than second in the small parameter $g/\varepsilon_t$, we obtain, up to a global energy shift

$$\begin{aligned} H'_{S+A}(\varepsilon_t) &= U(t)H_{\text{S+A}}U(t)^\dagger + i\dot{U}(t)U(t)^\dagger \qquad (2.42)\\ &= \frac{\hbar\varepsilon_t}{2}\sigma_z + \hbar\omega\left(a^\dagger a + \frac{1}{2}\right) + \frac{\hbar g^2}{\varepsilon_t}(a^\dagger + a)^2\sigma_z \\ &\quad + i\frac{\hbar\omega g}{\varepsilon_t}(a^\dagger - a)\sigma_y - \frac{\hbar g\dot{\varepsilon}_t}{\varepsilon_t^2}(a^\dagger + a)\sigma_y . \end{aligned}$$

The last term originates from the explicit time dependence of the transformation $U(t)$. We now consider a qubit driving that is slow compared to the qubit's own time scale and that is comparable to the oscillator's time scale

$$\dot{\varepsilon}_t/\varepsilon_t \simeq \omega \ll \varepsilon_t \,. \tag{2.43}$$

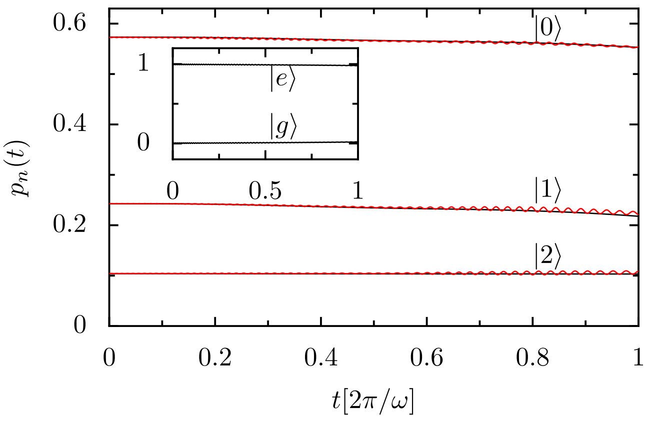

FIGURE 2.7: Comparison between the dynamics generated by the Rabi Hamiltonian in Eq. (2.39) (black line), and the dynamics generated by the diagonal Hamiltonian in Eq. (2.44) (red line). The plot shows the evolution of the population of the first three eigenstates of the oscillator. The inset shows the corresponding evolution of the qubit population. The initial state was $|g\rangle\langle g|\, e^{-\beta H_S(\lambda_0)}/\mathrm{tr} e^{-\beta H_S(\lambda_0)}$. We used the driving $\varepsilon_t = \hbar g^2/2\lambda_t$, where $\lambda_t = \lambda_0 + vt$, and the following parameters: $g = 2.5\hbar\omega$, $v = 1.52\pi\omega$, $\lambda_0 = 0.0625\hbar\omega$ and $1/\beta = \hbar\omega$.

In this way, the oscillator can be driven out of equilibrium while the qubit undergoes an adiabatic evolution. Note that the factors $g\omega/\varepsilon_t$ and $g\dot{\varepsilon}_t/\varepsilon_t^2$ are comparable to the factor $g^2/\varepsilon_t$ appearing in the third term of Eq. (2.42). However, the last two terms are oscillating much faster and can therefore be neglected within a rotating wave approximation. This can be seen by switching to the interaction picture with respect to $\hbar\varepsilon_t\sigma_z/2 + \hbar(\omega a^\dagger a + 1/2)$, where the last two terms contain the frequencies $\pm(\bar{\varepsilon}_t \pm \omega) \simeq \pm\bar{\varepsilon}_t = \pm t^{-1}\int_0^t \varepsilon_s ds$ and the second term contains the much lower frequencies $0, \pm 2\omega$. We thus conclude that (see Appendix A for a detailed derivation)

$$\begin{aligned} H'_{\mathrm{S+A}}(\varepsilon_t) &= \frac{\hbar\varepsilon_t}{2}\sigma_z + \hbar\omega\left(a^\dagger a + \frac{1}{2}\right) + \frac{\hbar g^2}{\varepsilon_t}(a^\dagger + a)^2\sigma_z \\ &= \frac{\hbar\varepsilon_t}{2}\sigma^z + \hbar\omega\left(a^\dagger a + \frac{1}{2}\right) + \left(\frac{\hbar g^2}{\varepsilon_t}\Pi_e - \frac{\hbar g^2}{\varepsilon_t}\Pi_g\right)(a^\dagger + a)^2 \qquad (2.44) \end{aligned}$$

is a good approximation of $H_{S+A}$ in the chosen parameter regime. This approximation is also justified by the numerical results depicted in Fig. 2.7, where we compare the time evolution generated by the Rabi Hamiltonian (2.39) in a parameter regime where Eqs. (2.40) and (2.43) hold, with the time evolution generated by the effective Hamiltonian (2.44). Obviously, the agreement between the two time evolutions is very good. The form (2.44) is already rather close to the desired Hamiltonian in Eq. (2.17). The main difference is that in Eq. (2.17) one drives the two subspaces spanned by $\Pi_{e,g}$ with two independent drivings $\lambda_t^{e,g}(u)$, whereas here we have only one driving parameter $\varepsilon_t$ that drives both subspaces at the same time. The other difference is that now the free qubit Hamiltonian is time-dependent. This affects only an overall phase, which therefore is not our major concern here. Note that the transformation (2.41) is similar but not quite the same as the transformation commonly employed in the dispersive regime [87]. We might call the regime investigated here, where the oscillator is very slow, the *soft mode* regime, and the resulting effective Hamiltonian $H'_{S+A}$, (see Eq. (2.44)) the *soft mode* Hamiltonian. Like the dispersive Hamiltonian, the soft mode Hamiltonian is diagonal in the natural qubit-oscillator basis, but different from the dispersive Hamiltonian, which presents a qubit-oscillator coupling linear in $(a+a^\dagger)$, the soft mode Hamiltonian presents a coupling term that is quadratic in $(a+a^\dagger)$.

### 2.4.2 Introducing a second qubit

To allow for the independent driving of two subspaces, we modify the method described above by introducing a second qubit. The measurement of the characteristic function of work is thus assisted by two ancillae. Our starting Hamiltonian is

$$H_{\mathrm{S+2A}} = \hbar\varepsilon_1\sigma_z^1/2 + \hbar\varepsilon_2\sigma_z^2/2 + \hbar\omega(a^\dagger a + 1/2) + \hbar(a^\dagger + a)(g_1\sigma_x^1 + g_2\sigma_x^2), \tag{2.45}$$

where $\varepsilon_{1,2}$ and $\sigma_{x,z}^{1,2}$ are the level splittings and the Pauli matrices of the two qubits, respectively. Following the derivation illustrated above, we work in the regime

$$\omega, g_i \ll \varepsilon_{i,t}\,, \quad \dot{\varepsilon}_{i,t}/\varepsilon_{i,t} \simeq \omega \ll \varepsilon_{i,t}\,, \quad i = 1, 2. \tag{2.46}$$

By applying the transformation

$$U(t) = e^{ig_1(a^\dagger+a)\sigma_y^1/\varepsilon_{1,t}}e^{ig_2(a^\dagger+a)\sigma_y^2/\varepsilon_{2,t}} \tag{2.47}$$

and neglecting cubic or higher terms in $g_1/\varepsilon_1$ and $g_2/\varepsilon_2$ as well as fast oscillating contributions, we arrive at

$$\begin{aligned} H'_{\mathrm{S+2A}}(\varepsilon_{1,t}, \varepsilon_{2,t}) \quad = \quad & \frac{\hbar}{2}\varepsilon_{1,t}\sigma_z^1 + \frac{\hbar}{2}\varepsilon_{2,t}\sigma_z^2 + \hbar\omega\left(a^\dagger a + \frac{1}{2}\right) \\ & + \hbar(a^\dagger + a)^2\left(\frac{g_1^2}{\varepsilon_{1,t}}\sigma_z^1 + \frac{g_2^2}{\varepsilon_{2,t}}\sigma_z^2\right). \end{aligned} \tag{2.48}$$

It is worthwhile rewriting $H'_{S+2A}$ in terms of projectors $\Pi_{i,j}$, $i,j \in \{e,g\}$, onto the four states $|i,j\rangle$:

$$\begin{aligned} H'_{\mathrm{S+2A}}(\varepsilon_{1,t}, \varepsilon_{2,t}) = & \hbar[\varepsilon_t^e + \omega(a^\dagger a + 1/2) + \lambda_t^e(u)(a^\dagger + a)^2]\Pi_{ee} \\ & + \hbar[\varepsilon_t^g + \omega(a^\dagger a + 1/2) + \lambda_t^g(u)(a^\dagger + a)^2]\Pi_{eg} \\ & + \hbar[-\varepsilon_t^e + \omega(a^\dagger a + 1/2) - \lambda_t^g(u)(a^\dagger + a)^2]\Pi_{ge} \\ & + \hbar[-\varepsilon_t^g + \omega(a^\dagger a + 1/2) - \lambda_t^e(u)(a^\dagger + a)^2]\Pi_{gg}, \end{aligned} \tag{2.49}$$

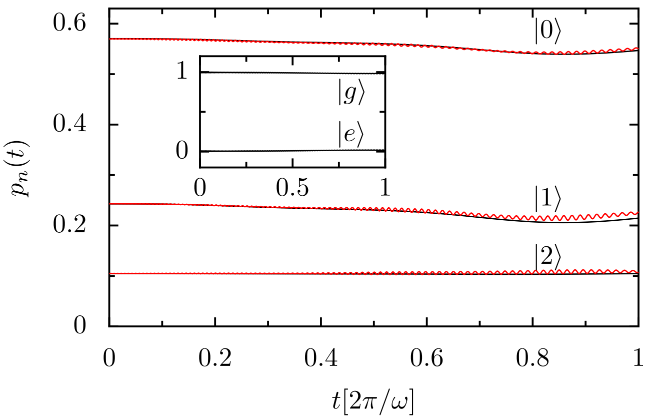

FIGURE 2.8: Comparison between the dynamics generated by the Tavis-Cummings Hamiltonian in Eq. (2.45) (black line), and the dynamics generated by the diagonal Hamiltonian in Eq. (2.49) (red line). The plot shows the evolution of the population of the first three eigenstates of the oscillator. The inset shows the corresponding evolution of the first qubit population. The initial state was $\rho_{S+2A}$ (Eq. 2.55), and $\varepsilon_{1,t}$, $\varepsilon_{2,t}$ were chosen as in Fig. 2.9, right panel, as to realize the drivings $\lambda_t^{e;g}$ shown in Fig. 2.9, left panel, corresponding to a linear ramp $\lambda_t = \lambda_0 + vt$. We employed the following parameters: $g_1 = 2.5\hbar\omega$, $g_2 = 1.5\hbar\omega$, $v = 1.52\pi\omega$, $\lambda_0 = 0.0625\hbar\omega$ and $1/\beta = \hbar\omega$.

where

$$\varepsilon_t^e = \tfrac{\varepsilon_{1,t}+\varepsilon_{2,t}}{2}, \tag{2.50}$$

$$\varepsilon_t^g = \tfrac{\varepsilon_{1,t}-\varepsilon_{2,t}}{2} \tag{2.51}$$

and

$$\lambda_t^e(u) = \frac{g_1^2}{\varepsilon_{1,t}} + \frac{g_2^2}{\varepsilon_{2,t}}, \tag{2.52}$$

$$\lambda_t^g(u) = \frac{g_1^2}{\varepsilon_{1,t}} - \frac{g_2^2}{\varepsilon_{2,t}}. \tag{2.53}$$

Like in Sec. 2.4.1, we compare the time evolution of the effective Hamiltonian (2.49) with the time evolution of the Rabi Hamiltonian (2.45) in Fig. 2.8. Again, the numerical results indicate that the time evolution of the Rabi Hamiltonian is well approximated. By focussing onto the subspace spanned by $\Pi_{ge}$ and $\Pi_{gg}$, i.e. where the qubit 1 is in the ground state, we see that by manipulating the two splittings $\varepsilon_{1,t}$ and $\varepsilon_{2,t}$ one can realize two independent drivings $\lambda_t^e(u)$ and $\lambda_t^g(u)$ acting in the respective sub-subspace. This realizes all the ingredients that we need for implementing the characteristic function measurements protocol employing a circuit QED setup.

### 2.4.3 The protocol

First, the two drivings $\varepsilon_{1,t}$ and $\varepsilon_{2,t}$ are chosen in such a way as to realize the protocols $\lambda_t^e(u)$ and $\lambda_t^g(u)$ in Eq. (2.19). This is achieved by solving Eq. (2.53) and (2.51) for $\varepsilon_{1,t}$

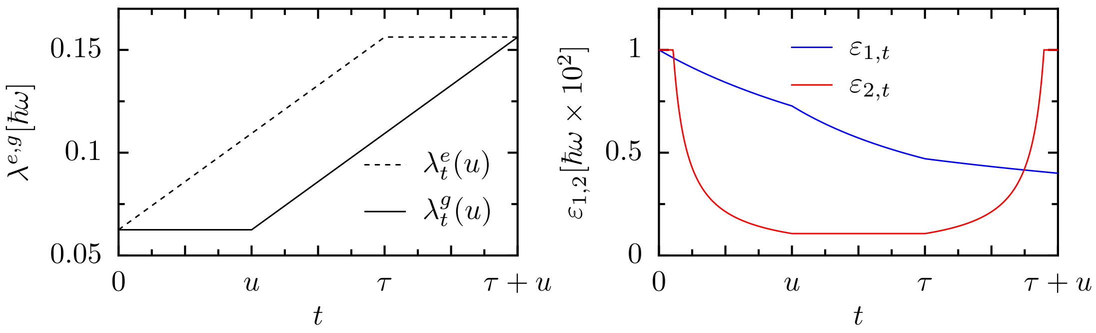

FIGURE 2.9: Left: time evolution of the two driving parameters $\lambda_t^{e,g}(u)$, Eq. (2.19), for a linear ramp of $\lambda_t$. Right: the time evolution of the two qubit splittings $\varepsilon_{i,t}$ that realize the drivings $\lambda_t^{e,g}(u)$, see Eq. (2.54).

and $\varepsilon_{2,t}$ to obtain (see Fig. 2.9):

$$\varepsilon_{1,t} = \frac{2g_1^2}{\lambda_t^e(u)+\lambda_t^g(u)}, \quad \varepsilon_{2,t} = \frac{2g_2^2}{\lambda_t^e(u)-\lambda_t^g(u)}. \tag{2.54}$$

With this choice, the protocol proceeds as follows, see Fig. 2.3:

1. Prepare the system at $t<0$ in the state
$$\rho_{\mathrm{S+2A}} = \frac{e^{-\beta(\omega a^\dagger a-\lambda_0(a^\dagger+a)^2)}}{Z_{\mathrm{S+2A}}(\lambda_0)}\Pi_{gg} \tag{2.55}$$
2. Perform a Hadamard operation $\sigma_H^2 = (\sigma_x^2+\sigma_z^2)/\sqrt{2}$ on the second qubit at time $t=0$.
3. Let the $\mathrm{S+2A}$ system evolve for a time $\tau+u$ according to $H_{\mathrm{S+2A}}(\varepsilon_{1,t},\varepsilon_{2,t})$.
4. Perform a Hadamard operation $\sigma_H^2$ at time $t=T=\tau+u$.

This results in the following two-qubit density matrix:

$$\begin{aligned}\rho_{2A}(u) &= \mathrm{tr}_S \sigma_H^2 U_{T,0}^{S+A}[\lambda^e,\lambda^g]\sigma_H^2\rho_{S+2A}\sigma_H^2\left(U_{T,0}^{S+A}[\lambda^e,\lambda^g]\right)^\dagger\sigma_H^2 \\ &= \left(1-\Re L_2(u)\,\Sigma_z^2-\Im L_2(u)\,\Sigma_y^2\right)/2,\end{aligned} \tag{2.56}$$

where

$$\begin{aligned}L_2(u) &= e^{i/\hbar\int_0^{\tau+u}\varepsilon_{2,t}dt}G[u,\lambda], &(2.57)\\ \Sigma_z^2 &= \Pi_{ge}-\Pi_{gg}, &(2.58)\\ \Sigma_y^2 &= |ge\rangle\langle gg| + |gg\rangle\langle ge|. &(2.59)\end{aligned}$$

Thus, performing two-qubit state tomography gives the characteristic function $G[u,\lambda]$

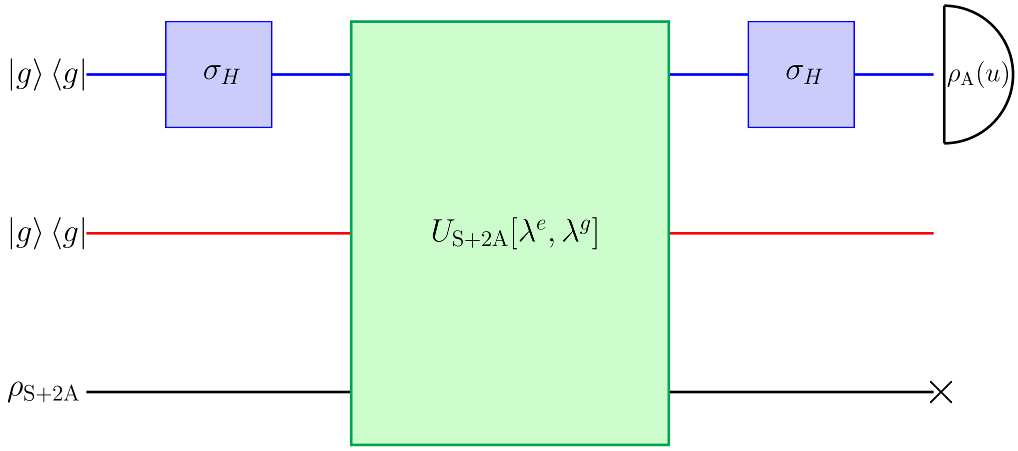

FIGURE 2.10: The interferometric scheme with 2 qubits represented by gate operations (compare with Fig. 2.3). Note that the Hadamard operations (multiplication with $\sigma_H$) and the measurement only is applied to the upper qubit.

of the process in Eq. (2.16) at the point $u$ (apart from a known phase factor). Note that qubit 2 alway stays in the state $|g\rangle$ during the protocol. Moreover, the relevant information about the characteristic function of work is encoded in the subspace where the second qubit is in its ground state. Therefore, it is enough to measure only qubit 1 after the protocol, see Fig. 2.10. This is a big simplification, since single qubit tomography is experimentally much easier. The state $\rho_{S+2A}$ can be prepared by thermalizing the $\mathrm{S}+2\mathrm{A}$ system at a temperature such that $\beta^{-1} \simeq \hbar\omega \ll \hbar\varepsilon_{1,0}, \hbar\varepsilon_{2,0}$. Qubit-state tomography can be realized in this setup by means of quantum non-demolition joint dispersive read-out [88]. This is possible due to the fact that the system and the oscillator are far detuned. Noticing that only terms involving $\Sigma_z^2$ and $\Sigma_y^2$ appear in Eq. (2.56), the wanted information can be retrieved in the following way: (i) Follow the protocol describe above. (ii) At the end of the protocol, perform a measurement of the two-qubit observables $\Sigma_z^2$ and $\Sigma_y^2$. Repeat (i) and (ii) many times to obtain the expectation values $\langle\Sigma_z^2\rangle$, and $\langle\Sigma_y^2\rangle$. Then, $\Re L_2(u) = -\langle\Sigma_z^2\rangle$, $\Im L_2(u) = -\langle\Sigma_y^2\rangle$.

### 2.4.4 Numerical test

The discussion above shows that by going to the right parameter regime, the Hamiltonian (2.17) can be realized using the standard system of circuit QED. Hence, it is in principle possible to realize the interferometric scheme introduced in Sec. 2.2.1 using a superconducting chip. The approximation steps needed to derive the effective Hamiltonian (2.49) were supported by numerical studies (see Figs. 2.7 and 2.8). The aim of this subsection is to check numerically how good these approximations are, when it comes to calculating the work probability distribution. We numerically studied the case of a linear ramp in the protocol

$$\lambda_t = \lambda_0 + vt \tag{2.60}$$

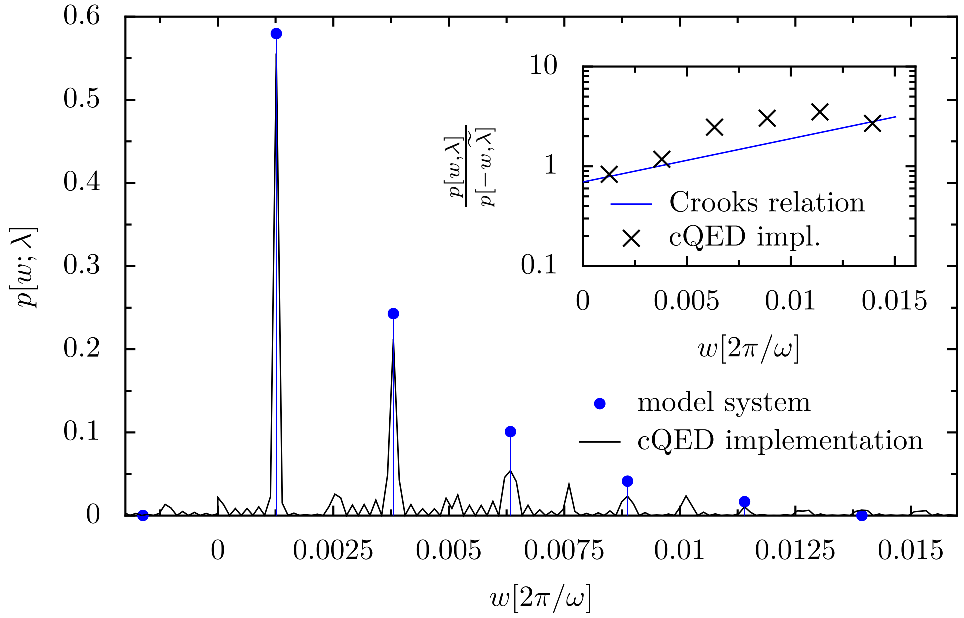

FIGURE 2.11: Work probability distribution of a parametrically driven oscillator. Solid black line: Numerical result obtained by the interferometric 2 qubits+oscillator setup. Blue points: Result obtained by solving the exact equations of motion governed by the Hamiltonian (2.16). Inset: Check of the Crooks fluctuation theorem. The parameter used are: $g_1 = 2.5\hbar\omega$, $g_2 = 1.5\hbar\omega$, $v = 1.52\pi\omega$, $\lambda_0 = 0.0625\hbar\omega$, $1/\beta = \hbar\omega$ and $\tau = 2\pi/\omega$.

using $1/\omega$ as unit of time and the parameters $g_1 = 2.5\omega$, $g_2 = 1.5\omega$, $\lambda_0 = 0.0625\omega$, $v = 1.5/2\pi\omega$, $\tau = 2\pi/\omega$. For $\omega = 300$ MHz this amounts to couplings $g_1 = 750$ MHz and $g_2 = 450$ MHz, an initial qubit splitting $\varepsilon_{1,0} = 30$ GHz and a velocity of $v \approx 70$ (MHz)$^2$. The level splitting of the second qubit goes to infinity at the beginning and at the end of the protocol, corresponding to a complete decoupling. The cutoff we introduced to handle this divergence is equivalent to $\varepsilon_{2,0} = 600$ GHz. Being aware of the fact that such strong coupling strengths are not feasible at present, we are optimistic that the technological progress will proceed towards this deep ultra-strong coupling regime soon [86, 89]. The temporal development of the two drivings $\lambda_t^{e,g}(u)$ is illustrated in Fig. 2.9 left. The graph in the right panel of Fig. 2.9 shows the corresponding time evolution of the two qubit energy splittings $\varepsilon_{i,t}$, $i = 1, 2$. Note that $\varepsilon_{2,t}$ diverges for $t \to 0$ and for $t \to \tau + u$. In our simulation, $\varepsilon_{2,t}$ was cut at the value $10\varepsilon_0$. This results in a deviation of the actual drivings $\lambda_t^{e,g}$ from those reported in Fig. 2.9 left panel at the beginning and the end. For small $u$ (as compared to $\tau$), this deviation becomes more relevant. With the so chosen parameters, the condition (2.46) was obeyed at all times $t \in [0, \tau + u]$.

We computed $\rho_{2A}(u)$ according to Eq. (2.56), where the time evolution was obtained by numerical integration of the Liouville-von Neumann equation. The thermal energy $\beta^{-1}$ was chosen equal to $\hbar\omega$. We then extracted the real and imaginary parts of the characteristic function $G[u, \lambda]$ using Eq. (2.57). Figure 2.11 shows the work probability distribution obtained after inverse Fourier transform of the so-obtained $G[u, \lambda]$. The blue dots show the values of the work probability density function as obtained by integrating the model Hamiltonian (2.16) directly. The approximations introduced by our implementation result in a spreading of the peaks, as compared to the expected ones, and to the emergence of further peaks in the work probability at high $w$ (not shown). Because of normalization these effects lower the height of the relevant peaks. We repeated the same procedure for the time reversed protocol $\widetilde{\lambda}_t = \lambda_\tau - vt$. The inset of Fig. 2.11 shows a good agreement between the logarithm of the ratio $p[w; \lambda]/p[-w, \widetilde{\lambda}]$ obtained by our numerics, and the linear behavior expected from Eq. (2.14). The agreement is however not as good as one would expect from Fig. 2.8 which shows very good agreement between the dynamics of the model Hamiltonian and the actual Hamiltonian. One source of error is the fast oscillating phase $e^{i/\hbar \int \varepsilon_{2,t} dt}$ in Eq. (2.57), which has to be taken away before the inverse Fourier transformation is applied. Moreover, in order to get an acceptable resolution we had to go to large $u$ in Fourier space, resulting in long propagation times. This leads to an amplification of the otherwise small errors coming from the approximations and the cut off. These points may pose an issue at the experimental level as well.

## 2.5 Summary and Outlook

We have extended the interferometric scheme of Dorner *et al.* [8] and Mazzola *et al.* [9] for the measurement of work distributions. We noticed that the method lends itself straightforwardly to the application to open quantum systems, even in the regime of strong dissipation. This is a crucial advantage beyond the previous works, because it opens the possibility to study work fluctuation in arbitrary open quantum system far from equilibrium experimentally, as well as theoretically. It is the task of future research to investigate these opportunities. The central novelty is the illustration of a realistic implementation of the method with current circuit QED technology. Particularly, we consider a transmission line resonator, used as the system and a charge qubit acting as ancilla, in order to determine the characteristic function of work of an parametrically driven oscillator. To adapt the scheme for circuit QED we introduced a second ancilla qubit, i.e. a second charge qubit. This technique may prove useful in all experimental scenarios where, as in the present case, two independent drivings might not be easily achieved with a single qubit. We show that by working in the “soft mode” regime, where the oscillator is slow, the coupling between system and ancilla is effectively diagonal and achieve the driving $\lambda_t(a^\dagger + a)^2$ indirectly by modulating the qubit splitting. Our numerical simulations show the experimental feasibility. As an alternative to the proposed implementation one could use a setup that enables the control of $\lambda_t$ directly. This could for example be implemented by coupling a flux qubit to a SQUID, as illustrated in [90].

# Chapter 3

# Entanglement creation in a quantum dot-nanocavity system by Fourier-synthesized acoustic pulses

As pointed out by Richard Feynman in 1981, it is impossible to efficiently simulate the time evolution of a quantum system on a classical computer, i.e., a computing machine with a state that is specified with certainty at any instant of time [91]. He argued that quantum systems should be simulated by other quantum systems and thereby introduced the concept of quantum computation. Later David Deutsch proposed an algorithm for a quantum computer that solves a deterministic problem exponentially faster than any classical algorithm [92] and thereby triggered a revolution in quantum physics and computer science. Although this algorithm was of little practical use, it provided the inspiration for other quantum algorithms like the Grover algorithm [93], leading to an exponentially speed up of the search in large databases, and the Shor algorithm, making it possible it find the prime factors of large numbers in polynomial time [94]. Hence, two of the most prominent problems in computer science and information theory could be solved efficiently using a quantum computer.

Nowadays, plenty of quantum algorithms and protocols for a quantum computer exist [95], most of them using entanglement, a quantum mechanical correlation in composite systems, defined in Sec. 3.1, as a fundamental resource [96]. In practice, the creation and control of entanglement in a quantum system is one of the main challenges one has to master, when it comes to the implementation of the "hardware" for a quantum computer [97]. By definition, entanglement cannot be created by local operations and, thus, requires some interaction between the subsystems. In order to achieve a controlled degree of entanglement, one may turn on and off the effective interaction, by tuning the subsystems into or close to resonance for a limited time. This includes a linear sweep across the resonance, giving rise to a Landau-Zener (LZ) scenario at an avoided crossing. In between the regimes of adiabatic following and sudden switching, this process splits the wavefunction into two parts with a well-defined phase and thereby creates an entangled state.

Since entanglement relies on a well-defined phase relation, it is fundamentally limited by the susceptibility to decoherence of the chosen architecture. In the very active field of solid-state quantum systems the focus of LZ-based entanglement creation was set in the past mainly to superconducting [19, 98] or spin-based [99] setups using their remarkable coherence properties. Although all-electrical radio frequency control can be readily implemented in these systems, transfer of the encoded quantum information to "flying" photonic qubits [100, 101] is difficult to achieve. In contrast, excitonic qubits in a single semiconductor quantum dot have the advantage that they can be integrated into optical circuits, although their coherence times cannot compete with the remarkable coherence times that have been observed, e.g. with superconducting qubits. Recently, it was demonstrated that coherent acoustic phonons formed by a surface acoustic wave (SAW) serve a fast tuning mechanism for the resonance frequency of a optical mode in a photonic resonator [102]. Being one order of magnitude faster than alternative approaches, this method opens the possibility to implement LZ-gates in semiconductor cavity QED and gives the ability to convert stationary and flying qubits.

In this chapter, we discuss the possibility to create entanglement in a cavity QED system consisting of an excitonic two-level system in a self-assembled quantum dot coupled to a cavity formed by a photonic resonator, see Fig. 3.1. We introduce a time-dependent detuning provided by SAWs and consider various feasible pulse shapes. In order to simulate the dynamics of the system, we numerically solve a master equation including the dissipative effects of (spontaneous) quantum dot decay and photon loss. This allows us to study, for experimentally demonstrated system parameters, to what extent it is possible to entangle the state of the quantum dot with the state of the cavity and how decoherence affects the system. Finally, we discuss directions to reduce the experimental complexity due to the high drive frequencies by using tailored Fourier-synthesized gating pulses. We begin with brief introductions to entanglement theory and the physics of quantum dots and photonic crystals. The results of this chapter have been published previously in [103].

## 3.1 Quantum entanglement and concurrence

Here, we give a formal definition of entanglement and introduce the concurrence, an entanglement measure for mixed states of two qubits. Later, we will use the concurrence to quantify the entanglement in a quantum dot–nanocavity system. Formally, for a composite system with Hilbert space $\mathcal{H} = \otimes_l^n \mathcal{H}_l$, a general state

$$|\Psi\rangle = \sum_{i_1,\dots,i_n} c_{i_1\dots i_n} |i_1\rangle \otimes |i_2\rangle \otimes \cdots \otimes |i_n\rangle \tag{3.1}$$

is entangled, if it is not separable, i.e. if it cannot be written as a product state $|\Psi\rangle \neq |\Psi_1\rangle \otimes |\Psi_2\rangle \otimes \cdots \otimes |\Psi_n\rangle$. Here $(|i_l\rangle)$ $|\Psi_l\rangle$ is a (basis) state of the subspace $\mathcal{H}_l$. If a composite system is in an entangled state (3.1), it is in general not possible to attribute a pure state to the subsystem $\mathcal{H}_l$. Moreover, it is not possible to create an entangled state from a separable one by local operation acting on a subsystem $\mathcal{H}_l$ alone. Extending the definition to mixed states with total density matrix $\rho$, a state is entangled if:

$$\rho \neq \sum_i p_i \rho_1^i \otimes \cdots \otimes \rho_n^i, \tag{3.2}$$

for every local basis of the subspaces $\mathcal{H}_l$. From the definition (3.2) it follows that "most" of the states in the composite Hilbert space $\mathcal{H}$ are entangled, to some extent. For quantum information processing, however, in general highly entangled states are required [95]. In order to quantify the entanglement of a given quantum state one introduces entanglement measures, like the entanglement entropy [104]. It turns out that specially for mixed states and many-body systems the quantification of entanglement is non-trivial problem [105]. In this work, we will only deal with the entanglement in a bipartite system $\mathcal{H} = \mathcal{H}_A \otimes \mathcal{H}_B$ and quantify it in terms of the *concurrence* [106]

$$\mathcal{C}(\rho) = \max(\chi_1 - \chi_2 - \chi_3 - \chi_4, 0), \tag{3.3}$$

where the $\chi_i$ are the square roots of the eigenvalues of the matrix $(\sigma_y^{(\mathrm{A})} \otimes \sigma_y^{(\mathrm{B})})\rho^*(\sigma_y^{(\mathrm{B})} \otimes \sigma_y^{(\mathrm{A})})$ in descending order. Here, $\sigma_y^{(\mathrm{A})}/\sigma_y^{(\mathrm{B})}$ are Pauli matrices on the two dimensional subspaces $\mathcal{H}_\mathrm{A}/\mathcal{H}_\mathrm{B}$ and $\rho^*$ denotes the complex conjugate density matrix $\rho$ expressed in the "magic basis" of Bell states [106]. The concurrence is closely related to the so called entanglement of formation[1] [108]

$$\mathcal{E}_\mathrm{f}(\rho) = \inf\Big\{\sum_i \; p_i \; S(\mathrm{tr}_\mathrm{A}\rho_i) \;\;|\;\; \sum_i p_i\rho_i = \rho\Big\}, \tag{3.4}$$

a standard entanglement measure for bipartite mixed states $\rho = \rho_\mathrm{A} \otimes \rho_\mathrm{B}$, which follows from the entanglement entropy[2] by convex roof construction [104]. Here $S(\rho) = -\mathrm{tr}\{\rho \mathrm{ln} \rho\}$ denotes the von-Neumann entropy. In contrast to the entanglement of formation, the concurrence can be calculated in practice without much computational effort.

---

[1] The entanglement of formation can be expressed as monotonic function of the concurrence [107].

[2] The entanglement entropy is a common entanglement measure for pure states.

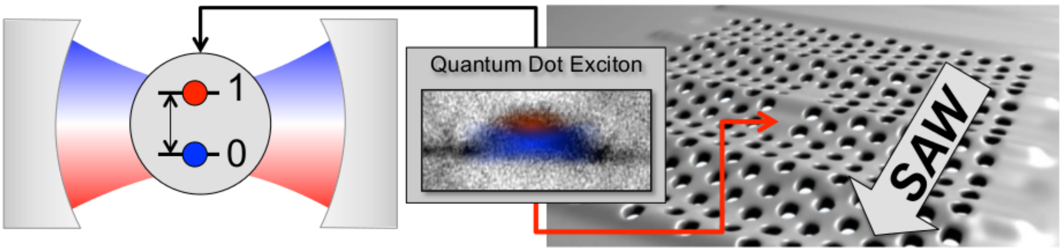

Figure 3.1: Semiconductor quantum dot inside a photonic crystal nanocavity serving as a realization of cavity QED. Applying surface acoustic waves (SAWs) to the photonic crystal leads to a modulation of the cavity resonance frequency.

For separable states, it vanishes, while for (maximally entangled) Bell states it takes the value of unity.

## 3.2 A quantum dot in a nanocavity

A quantum dot is a semiconductor nano-structure that confines the motion of electrons, electron holes, or excitons (electron-hole pairs) in all three spatial dimensions. This confinement can be, for example, due to an electrostatic potential or due to the small diameter of nanocrystalline structures. As a consequence of this confinement, the quantum dot exhibits a discrete energy spectrum similar to the spectrum of a "particle in a box" or an atomic spectrum. Hence quantum dot are sometimes referred to as "artificial atoms". This discreteness, as well as the possibility to coherently manipulate its state, make quantum dots a promising candidate for basic device units for quantum information processing. One approach is to use the fundamental optical excitation $X$ (exciton), creating an electron-hole pair, and the ground state of a quantum dot as qubit [109]. Using tailored laser pulses this quantum dot qubit can be excited in a controlled way. In order couple the quantum dot qubit to a single photonic mode, one places it inside a high-$Q$ nanophotonic defect resonator defined in a two-dimensional photonic crystal membrane [110]. Such a photonic crystal cavity is composed of a periodic dielectric structure, where the periodicity of the dielectric constant induces a photonic band gap [111, 112]. Hence, depending on their wavelength, photons are forbidden to propagate through the periodic structure, so that periodic crystals can be used to guide or trap light to regions where the periodicity is resolved. This opens the possibility to design optical cavities or even optical quantum networks [100, 113].

Here, we consider a single quantum dot couple to a photonic crystal cavity (see Fig. 3.1) modeled by the Jaynes-Cummings (JC) Hamiltonian [114]

$$H_{\mathrm{JC}} = \frac{\varepsilon}{2}\sigma_z + \hbar\omega a^\dagger a + g(a\sigma_+ + a^\dagger\sigma_-), \tag{3.5}$$

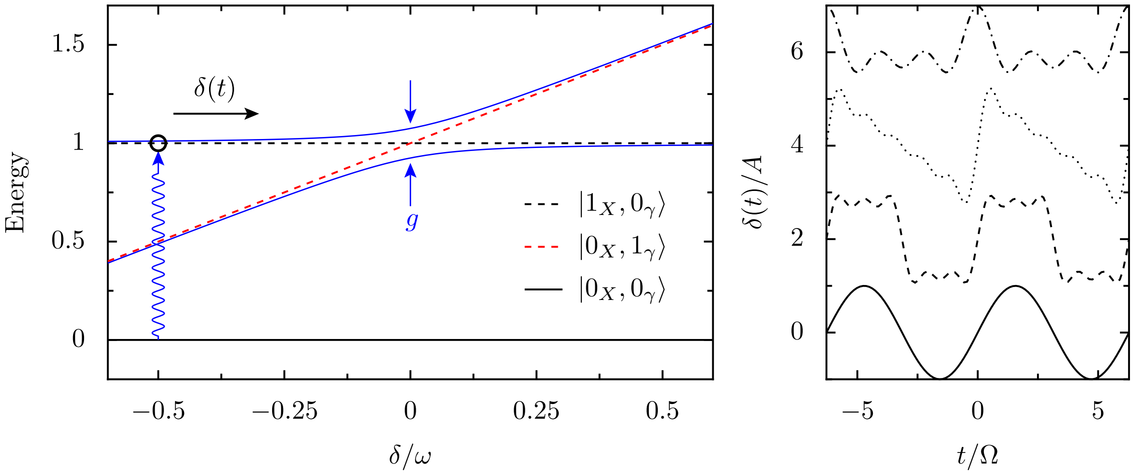

FIGURE 3.2: Left: Energy spectrum of the JC Hamiltonian (3.5) in dependence on the detuning. Owing to the cavity-quantum dot coupling $g$, the diabatic exciton energy (black dotted line) and the one-photon energy (red dotted line) form avoided crossing. The blue lines show the corresponding energy eigenstate with one exciton/photon in the system. In order to prepare the system in a entangled state we excite one exciton from the ground state with a laser pulse (blue wavy line) and sweep through the crossing with according to $\delta(t)$. Right: Waveforms defined in Eq. (3.8) as a function of time. Sine, Square, Sawtooth, Spike (from bottom up).

where the pseudo-spin operators $\sigma_z$ and $\sigma_\pm = 1/2(\sigma_x \pm i\sigma_y)$ describe the excitonic quantum dot within a two-level approximation in the basis of the ground state $|0_X\rangle$ and the one-exciton state $|1_X\rangle$ with the energy splitting $\varepsilon$. The bosonic operators $a$ and $a^\dagger$ refer to the cavity with resonance frequency $\omega$, which is dipole coupled to the quantum dot according to $g\sigma_x(a^\dagger + a)$. This leads to the Rabi Hamiltonian (2.39), introduced in previous chapter. Equation (3.5) can be derived from Eq. (2.39) by applying the rotating wave approximation (RWA). Transforming the system to the interaction picture with respect to the uncoupled Hamiltonian ($g = 0$), the transformed Hamiltonian contains terms proportional to $\sigma_+ a$ and $\sigma_- a^\dagger$, oscillating with $\exp[\pm i(\omega - \varepsilon/\hbar)]$ and terms proportional to $\sigma_- a^\dagger$ and $\sigma_+ a$ oscillating with $\exp[\pm i(\omega + \varepsilon/\hbar)]$, respectively. Close to resonance, i.e. for $\varepsilon \approx \hbar\omega$, the first terms are slowly oscillating whereas the latter terms exhibit fast counter-rotating oscillations. If additionally the coupling is weak, i.e. $g \ll \min\{\varepsilon, \hbar\omega\}$, the time scales separate and the fast oscillating terms average out, so that the corresponding terms can be neglected [87]. This results in the JC Hamiltonian Eq. (3.5). In contrast to the Rabi Hamiltonian (2.39), the JC Hamiltonian conserves the number of excitations in the system, so that the Hilbert space of the composed system discerns into doublets spanned by the states $|1_X, n_\gamma\rangle$ and $|0_X, (n+1)_\gamma\rangle$. As a function of the detuning $\delta = \varepsilon - \hbar\omega$, the eigenenergies of $H_{\mathrm{JC}}$ form avoided crossings of width $2\sqrt{n+1}g$ [115], see Fig. 3.2.

Experimentally, quantum dots coupled to a nanocavity have been studied over the past decade by several groups [116], who successfully demonstrated in key experiments both, the weak [117–119] and the strong [120–124] coupling regime of cavity QED.

Recently, it has been shown that photonic crystal nanocavities uniquely allow for a dynamical and reversible spectral control of the optical mode at Gigahertz frequencies using the coherent acoustic phonon field of a radio frequency SAW [102]. This introduces an external driving to the system, which is crucial for implementing coherent control schemes. Note that the quantum dot transition is also sensitive to the strain and the electric field induced by the SAW. Previous experimental data [125] as well as other experimental studies [126] on self-assembled InGaAs quantum dots suggest that the bandwidth of this modulation is roughly three times smaller than that of the cavity. Therefore, we set the quantum dot transition to be constant during the acoustic cycle and treat the nanocavity resonance as time-dependent. A sketch of this system is shown in Fig. 3.1. Since the SAW modulates the cavity frequency, the latter becomes time-dependent, i.e. $\omega \to \omega(t)$. This implies that also the detuning gets modulated with time: $\delta \to \delta(t)$. For the case of a sinusoidal wave, it is $\delta(t) = \delta_0 + A\sin[\Omega(t-t_0)]$. It has been shown that in general also the superpositions of acoustic waves with different frequencies are experimentally feasible [102]. If the amplitude $A$ exceed the static detuning $\delta_0$ the system passes through the avoided crossing and, for sufficient strong driving, non-adiabatic transitions are induced. This enables for the implementation of Landau-Zener entangling gates, discussed in the following.

## 3.3 Entanglement creation with Landau-Zener transitions

If the amplitude of the (SAW) is large compared to the extent of the avoided crossing, the driving can be linearized, resulting in a sweep velocity of the order $v \sim A\Omega$. This leads to a curve crossing problem of the Landau Zener type [15–18]. Let us assume that system is initially in the state $|1_X, 0_\gamma\rangle$. From the experimental point of view this initial state seems natural, since the exciton state can be prepared in a controlled way using suitable laser pulses. For adiabatically slow sweeping, an initial exciton state then transforms into a photon, $|0_X, 1_\gamma\rangle$, by adiabatic following. Increasing the sweep velocity, the system may stay in its initial state with a probability given by the LZ-formula (see Appendix B) [15–18]

$$P_{\mathrm{LZ}} = \exp(-2\pi g^2/\hbar v). \tag{3.6}$$

Far from the crossing region the final state yields

$$|\Psi(\infty)\rangle = \alpha\,|0_X, 1_\gamma\rangle + \beta\,|1_X, 0_\gamma\rangle\,, \tag{3.7}$$

with $\alpha = \sqrt{1-P_{\mathrm{LZ}}}$ and $\beta = \sqrt{P_{\mathrm{LZ}}}$. Significant exciton-cavity entanglement requires $P_{\mathrm{LZ}} \approx 1/2$. In this case, the state $|\Psi(t)\rangle$ becomes a maximally entangled Bell state [19]. Note that Eq. (3.7) is only exact for linear driving and $t \to \infty$. In general, the values of $\alpha$ and $\beta$ will be time-dependent and reflect the specific form of the driving. In the case of periodic driving the return to the crossing region after the LZ-transition will induce coherent oscillations and additional transition which depend on the phase of the system. Such features will be discussed in the next chapter and are unwanted in this case. Hence, it is desirable to slow down the modulation after the entanglement is created, so that further state manipulations or a readout of the quantum state can be performed. Therefore we like to exploit recent experimental achievements of a controlled superposition of higher harmonics to the SAW and consider more generic waves that lead to the detuning $\delta(t) = \delta_0 + \sum_{n=1}^{N} A_n \sin[n\Omega(t - t_0) + \phi_n]$. In an experiment both the amplitudes $A_n$ and the phases $\phi_n$ can be controlled rather well, which enables a flexible design of the pulses. Here we consider, besides purely sinusoidal driving, also waves with the characteristic shapes of a square, a sawtooth, and a spike, see Fig. 3.2 (right panel). We restrict ourselves to the experimentally feasible case in which those waves are approximated by a fundamental angular frequency of $\Omega = 2\pi \times 1\,\text{GHz}$ and its harmonics up to order $N = 5$, i.e., we consider the drivings

$$\delta(t) = \delta_0 + \begin{cases} A\sin[\Omega(t-t_0)] & \text{sine,} \\ \sum\limits_{n=0}^{5} \frac{A}{N}\cos[n\Omega(t-t_0)] & \text{spike,} \\ \sum\limits_{n=0}^{2} \frac{A}{2n+1}\sin[n\Omega(t-t_0)] & \text{square,} \\ \sum\limits_{n=1}^{5} \frac{A}{n}\sin[n\Omega(t-t_0)] & \text{sawtooth.} \end{cases} \tag{3.8}$$

Moreover, in order to highlight the benefit of non-sinusoidal pulses, we also consider pure sine waves with the angular frequencies $3\Omega$ and $5\Omega$.

Apart from the creation of entangled states, one of the main challenges when it comes to the implementation of solid-state devices for processing of quantum information is decoherence, i.e., the decay of entanglement [127] because of the interaction with an environment. In our case, the main sources of decoherence are the interaction of the quantum dot with the environmental phonons and the photon loss of the cavity which can be interpreted as a result of the interaction with with the photonic environment outside the cavity. In order to incorporate these environmental effects in our treatment, we employ a master equation description, derived in the next section.

## 3.4 Derivation of the master equation

Entanglement is a genuine quantum feature and, thus, is rather sensitive to decoherence caused by the interaction with environmental degrees of freedom. Here, the latter are mainly the photonic modes $\nu$ outside the cavity and the substrate phonons. Both can be modeled by an infinite sum of harmonic oscillators. Since this bath model will also be used in the next chapter, we make no assumptions about the system here and derive a general Markovian master equation starting from the system-bath Hamiltonian (compare with Eq. (2.24)):

$$H_{\mathrm{S+B}}(t) = H_{\mathrm{S}}(t) + H_{\mathrm{B}} + H_{\mathrm{SB}}, \tag{3.9}$$

where $H_{\mathrm{S}}(t)$ is the system Hamiltonian,

$$H_{\mathrm{B}} = \sum_{\nu} \hbar\omega_{\nu} a_{\nu}^{\dagger} a_{\nu}, \tag{3.10}$$

is the Hamiltonian of the (e.g. photonic or phononic) environment, modeled as an infinite sum of harmonic oscillators with frequencies $\omega_\nu$ and

$$H_{\mathrm{SB}} = X \sum_{\nu} \lambda_{\nu} (a_{\nu}^{\dagger} + a_{\nu}), \tag{3.11}$$

the system-bath interaction Hamiltonian describing the linear coupling of the system operator $X$ to the bath. Here, $\lambda_\nu$ is the coupling strength and $a_\nu^\dagger$, $a_\nu$ are the creation and, respectively, the annihilation operators of the bath mode $\omega_\nu$.

The time evolution of system-plus-bath is given by the *Liouville-von-Neumann equation*

$$\dot{\rho}_{\mathrm{S+B}}(t) = -\frac{i}{\hbar}[H_{\mathrm{S+B}}(t), \rho_{\mathrm{S+B}}(t)], \tag{3.12}$$

with $\rho_{\mathrm{S+B}}$ being the density matrix of the total system, while the density matrices of the reduced system and the bath alone will be denoted by $\rho_{\mathrm{S}}$ and $\rho_{\mathrm{B}}$, respectively. Transforming to the interaction picture with respect to the uncoupled system using the unitary operator $U_{t,t_0} = \mathcal{T}\exp\big(-i\int_{t_0}^{t} ds (H_{\mathrm{S}}(s) + H_{\mathrm{B}})\big)$ and formally integrating Eq. (3.12) leads to [115]

$$\tilde{\rho}_{\mathrm{S+B}}(t) = \tilde{\rho}_{\mathrm{S+B}}(0) - \frac{i}{\hbar}\int_0^t ds [\tilde{H}_{\mathrm{SB}}(s), \tilde{\rho}_{\mathrm{S+B}}(s)], \tag{3.13}$$

where $\tilde{A}(t) = U_{t,0}^{\dagger} A U_{t,0}$ denote operators in the interaction picture. Here we set the initial time $t_0 = 0$. Iterating this procedure leads to the Dyson series [115]

$$\begin{aligned}\tilde{\rho}_{\mathrm{S+B}}(t) = \tilde{\rho}_{\mathrm{S+B}}(0) + \sum_{0}^{\infty}\Big(-\frac{i}{\hbar}\Big)^n \int_0^t dt_1 \int_0^{t_1} dt_2 \dots \int_0^{t_{n-1}} dt_n \\ \times [\tilde{H}_{\mathrm{SB}}(t_1), [\tilde{H}_{\mathrm{SB}}(t_2), \dots [\tilde{H}_{\mathrm{SB}}(t_n) \tilde{\rho}_{\mathrm{S+B}}(0)].\end{aligned} \tag{3.14}$$

Assuming that system and environment are initially uncorrelated, i.e. assuming an initial condition of the Feynman-Vernon type

$$\rho_{\mathrm{S+B}}(0) = \rho_{\mathrm{S}}(0) \otimes \rho_{\mathrm{B}}(0), \tag{3.15}$$

truncating Eq. (3.14) at $n = 2$, and differentiating with respect to the final time, leads to

$$\frac{d}{dt}\tilde{\rho}_{\mathrm{S+B}}(t) = -\frac{i}{\hbar}[\tilde{H}_{\mathrm{SB}}(t), \tilde{\rho}_{\mathrm{S+B}}(t)] - \frac{i}{\hbar}\int_0^t ds[\tilde{H}_{\mathrm{SB}}(t), [\tilde{H}_{\mathrm{SB}}(s), \tilde{\rho}_{\mathrm{S+B}}(t)]. \tag{3.16}$$

This truncation is known as the *Born approximation* and is justified if the coupling between system and environment is week. Because we are only interested in the reduced dynamics of the system, we trace out the environment to obtain

$$\frac{d}{dt}\tilde{\rho}_{\mathrm{S}}(t) = -\frac{i}{\hbar}\mathrm{tr}_{\mathrm{B}}\int_0^t ds[\tilde{H}_{\mathrm{SB}}(t), [\tilde{H}_{\mathrm{SB}}(s), \tilde{\rho}_{\mathrm{S}}(s) \otimes \rho_{\mathrm{B}}], \tag{3.17}$$

where $\mathrm{tr}_{\mathrm{B}}$ denotes the trace over the bath degrees of freedom. Without loss of generality we assumed that $\mathrm{tr}_B\big(H_{\mathrm{SB}}(t)\rho_{\mathrm{B}}\big) = 0$.[3] Moreover, we drop the time parameter of the bath density matrix, assuming a large environment that is not altered because of the interaction with the system. Equation (3.17) is still non-local in time, i.e. it depends, at any instant of time, one the whole history of states. This makes it hard to solve it. Assuming that the bath correlations decay much faster than the system state changes, we perform the *Markov approximation* and replace $\rho_{\mathrm{S}}(s)$ by $\rho_{\mathrm{S}}(t)$. Moreover, we substitute $s$ by $t - s$ and let the upper limit of the integral go to infinity [4]. Finally, we arrive at the Markovian quantum master equation [4, 6, 128]:

$$\frac{d}{dt}\tilde{\rho}_{\mathrm{S}}(t) = -\frac{i}{\hbar}\int_0^\infty ds\, \mathrm{tr}_B[\tilde{H}_{\mathrm{SB}}(t), [\tilde{H}_{\mathrm{SB}}(t-s), \tilde{\rho}_{\mathrm{S}}(t) \otimes \rho_{\mathrm{B}}]. \tag{3.18}$$

### 3.4.1 Lindblad master equation for photon loss and exciton decay

In the following, we consider the case where the SAW-driven quantum dot–nanocavity system, described by the Hamiltonian (3.5), is interacting with the photonic environment outside the cavity. In this case, the bath is coupled to the cavity dipole operator $X = X_\gamma = a^\dagger + a$ with the interaction picture representation

$$\tilde{X}_\gamma(t) = a^\dagger e^{i\omega t} + a e^{-i\omega t}, \tag{3.19}$$

which coincides with the Schrödinger picture at $t = 0$. Since the SAW driving is slow compared to the system dynamics, the influence of the driving on the dissipation is negligible, moreover, the intrinsic coupling between quantum dot and cavity is one order

---

[3] This can always be achieved by appropriate re-definition of the system Hamiltonian [6].

of magnitude smaller than the cavity resonance frequency, so that $H_{\rm JC}$ is effectively diagonal in the basis of number states $|m_X, n_\gamma\rangle$. This allows us to treat the dissipative effects on the cavity, i.e. the photon loss, and the quantum dot dynamics separately. Consequently, we consider the system Hamiltonian

$$H_{\rm S} = \hbar\omega a^\dagger a, \tag{3.20}$$

for which we derive a master equation for the photon loss. Inserting the explicit form of the interaction Hamiltonian $\tilde{H}_{\rm SB}(t)$ in Eq. (3.17) and reordering of the terms leads to

$$\frac{d}{dt}\tilde{\rho}_{\rm S}(t) = \mathcal{C}(\omega)\Big(\big(a\tilde{\rho}_{\rm S}(t)a^\dagger - a^\dagger a\tilde{\rho}_{\rm S}(t)\big) + e^{-i\omega t}\big(a\tilde{\rho}_{\rm S}(t)a - aa\tilde{\rho}_{\rm S}(t)\big) + \text{h.c.}\Big), \tag{3.21}$$

where we introduced the half-side Fourier transform of the bath correlation function

$$\mathcal{C}(\omega) = \int_0^\infty ds e^{i\omega s}\langle B^\dagger(s)B(0)\rangle_{\rm B}. \tag{3.22}$$

Here, $\langle\ldots\rangle_{\rm B} = \text{tr}_{\rm B}\{\ldots\rho_{\rm B}\}$ is the average with respect to the bath density matrix and

$$B(t) = \sum_\nu \lambda_\nu(a_\nu^\dagger e^{i\omega_\nu t} + a_\nu e^{-i\omega_\nu t}). \tag{3.23}$$

Because the time scale $1/\omega$ defined by cavity resonance frequency in Eq. (3.21) is small compared to the relaxation time of the open system we can perform the *secular approximation* [128] and neglect the terms oscillating with $e^{\pm i2\omega t}$, in Eq. (3.21), since they are fast oscillating and average out, and obtain

$$\frac{d}{dt}\tilde{\rho}_{\rm S}(t) = \mathcal{C}(\omega)\big(a\tilde{\rho}_{\rm S}(t)a^\dagger - a^\dagger a\tilde{\rho}_{\rm S}(t)\big) + \text{h.c.} \tag{3.24}$$

In order to evaluate the function $\mathcal{C}(\omega)$, we assume a continuum of bath modes $\sum_{\omega_\nu} = \int d\omega' J(\omega')$ with the Ohmic spectral density $J(\omega') = \pi\sum_\nu |\lambda_\nu|^2\delta(\omega' - \omega_\nu) \equiv \pi\alpha_\gamma\omega'/2$ and the dimensionless dissipation parameter $\alpha_\gamma$ [5, 129, 130]. Moreover, we take the environment to be in a thermal state

$$\rho_{\rm B} = \frac{1}{Z_{\rm B}}\exp(-\beta H_{\rm B}), \tag{3.25}$$

with partition function $Z_{\rm B} = \text{tr}_B\exp(-\beta H_{\rm B})$ and inverse temperature $\beta$. Making use of the formula

$$\int_0^\infty ds\exp(\pm i\varepsilon s) = \pi\delta(\varepsilon) \pm i\text{PV}\frac{1}{\varepsilon}, \tag{3.26}$$

with PV being the Cauchy principal value, the integrals in Eq. (3.22) can can be evaluated to yield

$$\mathcal{C}(\omega) = \frac{1}{2}\Gamma_\gamma(\omega) + iS(\omega) \tag{3.27}$$

with the decay rate

$$\Gamma_\gamma = \Gamma_\gamma(\omega) = \pi\alpha_\gamma\omega(1 + N(\omega)) \tag{3.28}$$

and the Lamb shift

$$S(\omega) = \frac{1}{\pi} PV \int_0^\infty d\omega' \frac{1 + N(\omega)}{\omega - \omega'}. \tag{3.29}$$

The latter leads to a renormalization of the oscillator frequency and will be neglected in the following. Assuming a rather low temperature we can ignore thermal excitation of the cavity. Transforming back to the Schrödinger picture we get:

$$\frac{d}{dt}\rho_{\mathrm{S}}(t) = -\frac{i}{\hbar}[H_{\mathrm{S}}, \rho_{\mathrm{S}}] + \mathcal{L}_\gamma(\rho_{\mathrm{S}}) \tag{3.30}$$

with dissipative superoperator in Lindbald form [131, 132]:

$$\mathcal{L}_\gamma(\rho) = \frac{\Gamma_\gamma}{2}(2a\rho a^\dagger - a^\dagger a\rho - \rho a^\dagger a). \tag{3.31}$$

Mutatis mutandis, the same derivation holds for the treatment of dissipative effects on the quantum dot, stemming from the interaction with the environmental phonons, coupled via

$$X_X = \sigma_+ + \sigma_-. \tag{3.32}$$

This leads to the dissipator

$$\mathcal{L}_X(\rho) = \frac{\Gamma_X}{2}(2\sigma_-\rho\sigma_+ - \sigma_+\sigma_-\rho - \rho\sigma_+\sigma_-), \tag{3.33}$$

with the exciton decay rate

$$\Gamma_X = \pi\alpha_X\varepsilon. \tag{3.34}$$

Summing up the results, we arrive at the master equation:

$$\frac{d}{dt}\rho = -\frac{i}{\hbar}[H_{\mathrm{JC}}(t), \rho] + \mathcal{L}_\gamma(\rho) + \mathcal{L}_X(\rho). \tag{3.35}$$

## 3.5 Entanglement dynamics

We consider the dynamics of the cavity–quantum dot setup after an exciton is created at time $t = 0$, while the cavity is empty, i.e., we numerically integrate the master equation for the initial state $|1_X, 0_\gamma\rangle$. In course of time, the SAW sweeps the energies of the two subsystems through an avoided crossing by means of the time dependent detuning $\delta(t)$ (see Fig. 3.2). Moreover, the Lindblad forms (3.31) and (3.33) cause a decay towards the ground state $|0_X, 0_\gamma\rangle$. Our main aim is to investigate and to optimize the degree of entanglement for differently shaped SAW pulses. We quantify the entanglement by the *concurrence* (3.3). In order to employ this measure, we treat the cavity within

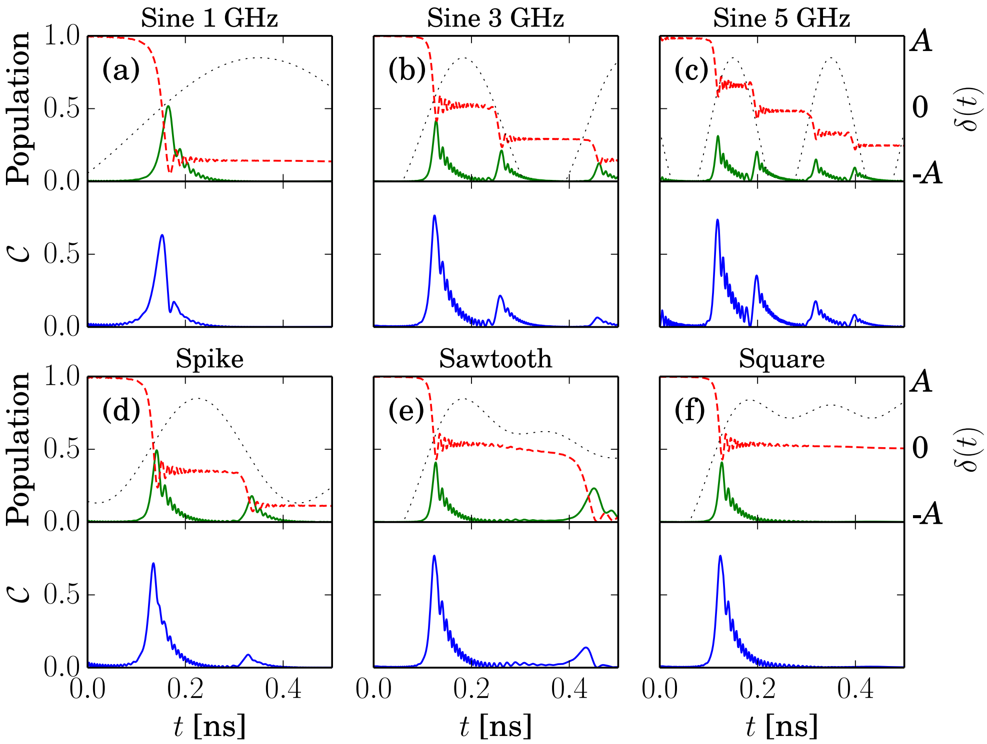

FIGURE 3.3: LZ entanglement dynamics for SAW shapes of a pure sine with frequencies 1 GHz (a), 3 GHz (b), and 5 GHz (c), as well as for a spike (d), a sawtooth (e), and a square (f), each with fundamental frequency $\Omega/2\pi = 1\,\mathrm{GHz}$. The cavity-dot coupling is $g = 35\,\mu\mathrm{eV}$, while the static detuning $\Delta_0 = 0.3\,\mathrm{meV}$ is modulated with an amplitude $A = 1\,\mathrm{meV}$, such that the crossing is reached at time $t_0 = T/10 = 0.5\,\mathrm{ns}$. The cavity and exciton decay rates read $\Gamma_\gamma = 25\,\mu\mathrm{eV}/\hbar$ and $\Gamma_X = 0.2\,\mu\mathrm{eV}/\hbar$. Upper panels: Population of the states $|1_X, 0_\gamma\rangle$ (red solid line) and $|0_X, 1_\gamma\rangle$ (green dashed line). The dotted line visualizes the course of the detuning $\delta(t)$. Lower panels: Cavity-dot entanglement in terms of the concurrence $\mathcal{C}$.

a two-level approximation in the subspace spanned by the states $|0_\gamma\rangle$ and $|1_\gamma\rangle$ with the corresponding Pauli matrices $\sigma_y^\gamma$. This approximation is well justified, because our Hamiltonian (3.5) preserves the total number of excitations, while our low-temperature dissipation kernels $\mathcal{L}_\gamma$ and $\mathcal{L}_X$ only contain decay terms.

For our modeling, we restrict ourselves exclusively to *experimentally demonstrated system parameters*. In particular, we assume a InGaAs-based system with optical transitions at $E_0 = \hbar\omega_0 = 1.3\,\mathrm{eV}$ and with the decay rates $\Gamma_X = 2\,\mu\mathrm{eV}$ and $\Gamma_\gamma = 25\,\mu\mathrm{eV}$ for the excition and the photon, respectively. The latter corresponds to a cavity quality factor of $Q = 5.2 \cdot 10^4$ and a photon life time of $\tau_\gamma = \hbar\Gamma_\gamma = 26\,\mathrm{ps}$. Furthermore, we assume the system in the strong coupling regime with a vacuum Rabi splitting $g > \Gamma_\gamma$. For a better comparison with the experiments we express all parameters (except for the SAW frequency) in terms of energy throughout this chapter.

In order to get a first impression of the dynamics, we depict in ,Fig. 3.3, the time evolution of the populations of the states $|1_X, 0_\gamma\rangle$ and $|0_X, 1_\gamma\rangle$, and the corresponding entanglement quantified by the concurrence, for various wave forms, while all other parameters are equal. In all subplots a LZ-transition is visible, whenever the detuning (black dotted line) is vanishing. For a purely sinusoidal driving with frequency $\Omega/2\pi = 1\,\mathrm{GHz}$, the population of the initial state is mainly transferred to $|0_X, 1_\gamma\rangle$. This corresponds to imperfect adiabatic following. At an intermediate stage at time $t \approx t_0$, the populations of both states are comparable, while phase coherence between the participating states ensures good entanglement with a concurrence up to $\mathcal{C} \approx 0.7$. However, since for these parameters, $P_{\mathrm{LZ}}$ is significantly smaller than $1/2$, soon after the crossing the one-photon state becomes highly populated. Therefore, the systems disentangle soon after having passed the crossing. Thus, we must increase the sweep velocity, which can be achieved by using a higher frequency. The results in panels (b) and (c) demonstrate, that this indeed augments the concurrence. Moreover, it increases the time during which the concurrence exceeds a certain threshold value. This "entanglement persistence" is mainly limited by the cavity decay rate $\Gamma_\gamma$, at least under the realistic condition $\Gamma_\gamma \gg \Gamma_X$. Thus, our goal is to find parameters and waveforms for which a significant entanglement is present during a time of the order $\hbar\Gamma_\gamma$. A theoretically interesting observation is that for higher frequencies, the system may pass through the avoided crossing several times in the time range considered. The resulting repeated passages depend on the phase acquired in between the crossings, leading to Landau-Zener-Stückelberg interference [16–18, 20]. However, for realistic cavity decay rates, dephasing is too fast and, thus, the coherent superposition of our entangled states turns into a (separable) mixture. Therefore, we will not discuss these effects in this context. In the next chapter, however, we will reconsider these interference effects for a driven qubit in great detail.

Even though SAWs with frequencies of 3 or 5 GHz are feasible, inducing them with a large intensity, such that the detuning amplitude becomes 1 meV, represents a rather difficult task. Waves with lower amplitudes are not helpful, because they lead to a smaller sweep velocity and, thus, we would loose what we gained from the higher frequency. Moreover, the initial preparation of the exciton with a laser pulse must be performed during a fraction of the driving period, because the laser pulse has a certain length and cannot be triggered with arbitrary precision. Thus, for shorter driving periods, one will have difficulties to carry out the preparation. These difficulties can be circumvented by employing more elaborate pulses such as the ones sketched in Fig. 3.2 (right) and given in Eq. (3.8). Notice that for these pulses, the contribution of each harmonic is significantly smaller than 1 meV, while the driving period remains at $2\pi/\Omega = 1\,\mathrm{ns}$. The resulting entanglement dynamics is plotted in Fig. 3.3(e–f). As compared to panel (a), the performance of the entanglement creation has improved. Moreover, as we will see below, this performance can be reached in a broader parameter range.

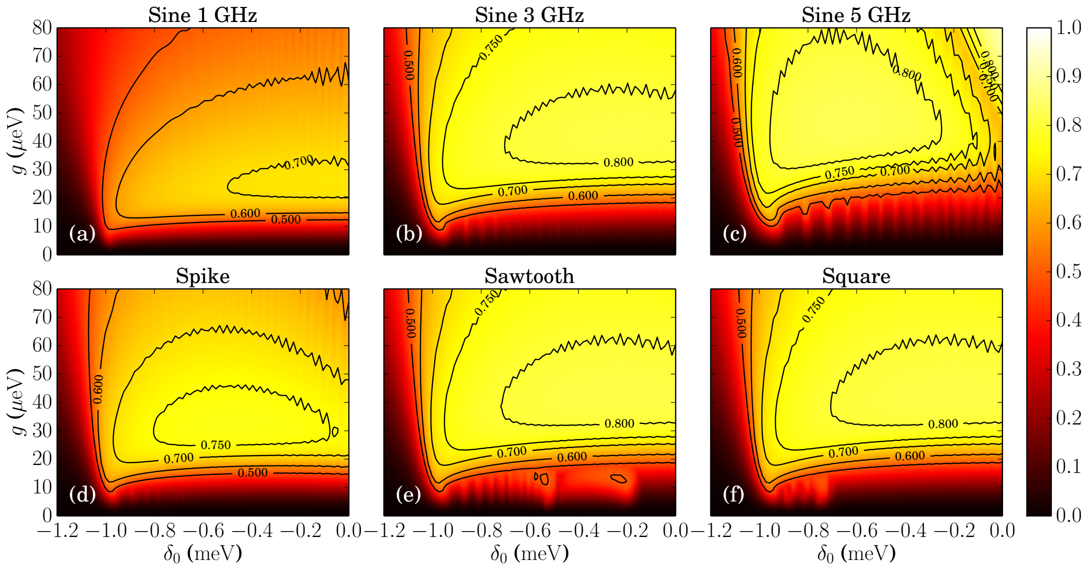

FIGURE 3.4: Maximum of the concurrence achieved as function of the static detuning $\delta_0$ and the dot-cavity coupling $g$. All other parameters, the wave forms, and the arrangement of the panels is as in Fig. 3.3.

In an experimental implementation of our proposed scheme, one would on the one hand like to obtain a rather large maximum for the concurrence, while on the other hand, an appreciable entanglement should be found during a not too short time, ideally limited only by $\Gamma_\gamma$. Moreover, the cavity-dot coupling $g$ is essentially a fixed parameter determined during chip fabrication, which implies that the width of the avoided crossing can be tuned only within a narrow range via the driving frequency and the amplitude. Therefore, it is desirable that the results do not depend too sensitively on $g$. Given this low flexibility, suggestions for more promising SAW shapes are particularly welcome.

## 3.6 Analysis of the parameter space

To analyze the performance of each wave form in a more systematic way, we employ two figures of merit. The first one is the maximal concurrence $\mathcal{C}$, reached during a time $T/4$ centered at the avoided crossing as function of $g$ and $\delta_0$, depicted in Fig. 3.4. For all frequencies and pulse shapes considered, the concurrence can reach values up to $\mathcal{C} \approx 0.8$. However, the basic sinusoidal wave at 1 GHz yields this value only in a small range of the coupling $g$, which requires a precise fabrication process. Since, as discussed above, for 3 and 5 GHz, the required amplitudes of the order 1 meV are difficult to achieve, the more elaborate pulse shapes are clearly preferable. For all three composed pulses, the plots of the concurrence maximum behave very similar. The common feature of all three is the rather steep slope of the detuning $\delta(t)$ close to the center of the avoided crossing, as it can be appreciated in the lower panels of Fig. 3.3. This suggests that the main

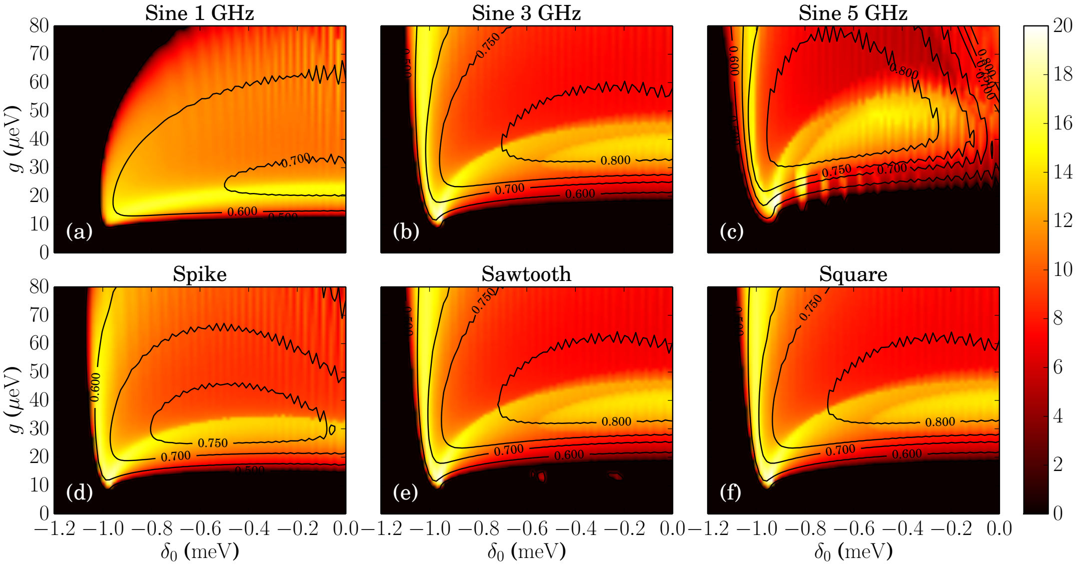

FIGURE 3.5: Persistence of the entanglement, i.e., time during which the concurrence exceeds the threshold value set by $\mathcal{C} > 1/2$. All parameters, wave forms, and the contour lines marking the maximum of the concurrence are as in Fig. 3.4.

effect of the higher-order Fourier components is to augment the sweep velocity at the crossing.

Our second figure of merit is the persistence time $\tau$ of the entanglement defined as the time during which $\mathcal{C} > 1/2$. This quantifier is depicted in Fig. 3.5. The contour lines enable a comparison with the results shown in Fig. 3.4. This reveals that a large maximum does not necessarily coincide with long persistence. This is in particular the case for the sinusoidal pulses with higher frequencies (panels (b) and (c)). Nevertheless, there exist regimes where both the entanglement maximum and the persistence are rather favorable and where $\tau$ practically reaches its theoretical limit, which is the cavity lifetime $\hbar/\Gamma_\gamma = 26\,\text{ps}$. As for the maximum, the plot for the sine wave with 3 GHz and the ones for the composed pulses (panels (d)–(f)) look similar. However, the former has the disadvantage of being experimentally more demanding. Interestingly enough, in two regimes, albeit small, pure sine waves yield surprisingly long entanglement duration: First, for 1 GHz in the regime $\delta_0 \approx -1\,\text{meV}$, $g \gtrsim 10\,\mu\text{eV}$, where, however, the maximum is rather low. Second, for 5 GHz, we witness in panel (f) at $g \approx 25\,\mu\text{eV}$ some islands with $\tau \gtrsim 20\,\text{ps}$. Combining the two criteria of large maximum $\mathcal{C}$ and long persistence, we can conclude that for an experimental realization, the quantum dot-cavity coupling $g$ should be in the range 20–50 $\mu$eV.

## 3.7 Summary and Outlook

The theoretical study of this chapter demonstrates the experimental feasibility of entanglement generation in a semiconductor quantum dot–nanocavity system by a SAW-gated LZ-transition. Using exclusively experimentally demonstrated, state of the art system parameters, we find high levels of entanglement corresponding to a concurrence of $\mathcal{C} > 0.8$. Its persistence is mainly limited by the photon loss from the cavity. This dominant dephasing mechanism arises from the moderate quality factor of such semiconductor-based cavities. An extension of this scheme to Fourier-synthesized SAW waveforms promises two significant advantages over a single-frequency sinusoidal drive. First, our model predicts, for square and sawtooth pulses, a large value of concurrence over the system-limited timescales for a broad range of $g$ and $\delta_0$. The second advantage lies in the experimental implementation: The complexity to achieve a sufficiently large modulation amplitude of 1 meV increases significantly with increasing SAW frequency, in particular for modulation frequencies of the order 3 GHz and larger. In order to generate Fourier-synthesized waveforms also higher harmonics with frequency larger than 1 GHz are needed, however, already small amplitudes are sufficient to create pulses with a considerably steeper slope. Moreover, the fundamental SAW period in the experiment remains constant at 1 ns which facilitates the synchronisation with the optical initialization and the measurement of the entanglement. The latter can be implemented, e.g., by extending existing schemes based on reflectivity spectroscopy [122] using short ($< 1$ ps) and broadband laser pulses as a function of time during the acoustic cycle. Moreover, since the system is initialized in the exciton state, i.e., in the lower branch of the avoided crossing, any signal from the upper branch detected the loss spectrum provides a fingerprint of the LZ-transition.

Another possible application of SAW based modulation schemes could be the controlled generation of photons by adiabatic following. Here, smaller SAW frequencies $< 1$GHz are sufficient to coherently transfer the excitation from the quantum dot to the cavity. The incoherent exponential decay out of the cavity then usually releases single photon with a Lorentzian spectral distribution. Using different tailored SAW pulses allows one to control the population in the cavity, and therefore to shape the wave packet of the released photons.

Finally we note, that the results of our theoretical study can be directly transferred to other types of semiconductor cavities, most notably Bragg-type microcavities [133] which are SAW-compatible [134]. In addition, amongst the broad variety of control techniques, electrical tuning of the quantum dot transition via the quantum confined stark effect [123, 135–137] could be an alternative approach to realize the required Gigahertz frequencies.

# Chapter 4

# Qubit interference at avoided level crossings

In the previous chapter, we considered a quantum system with a periodically modulated detuning. Since the amplitude of the modulation was sufficiently large, the driving could be linearized near an avoided crossing and the dynamics of the system could be qualitatively described in term of Landau Zener transitions. Because the lifetime of an excitation (the photon) in the system was shorter than half the driving period, it was also adequate to restrict to a single transition, since the excitation was lost before the crossing was reached a second time.

In general, however, sweeping the detuning with an ac-field, results in a series of avoided crossings, so that the wavefunction splits and recombines repeatedly—the quantum mechanical analogue of a Mach-Zehnder interferometer [20]. The resulting Landau-Zener-Stückelberg-Majorana (LZSM) interference patterns, have been demonstrated in various experiments with solid-state qubits [25–27, 29–32].

To observe LZSM patterns with an adequate resolution the system has be coherent, to some extent. Environmental fluctuations and dissipation will, in general, spoil the system's coherence, and therefore reduce the contrast of the interference pattern. From a different perspective, this enables to employ LZSM interferometry as a tool to determine the dephasing time of a qubit. The analysis of the interference pattern may be performed in "real space", i.e. as a function of detuning and amplitude [31], or in Fourier space [34]. The latter type of analysis is based on the observation that the Fourier transform of LZSM patterns exhibit arc structures with a characteristic decay [33]. By comparing measured and computed patterns for a qubit, one can determine the inhomogeneous broadening as well as the faster decoherence induced by substrate phonons [34]. Since this procedure takes considerable numerical effort, analytic knowledge about the patterns in Fourier space simplifies the analysis considerably.

In this chapter, we address two questions beyond related previous studies: the role of the system-bath coupling and influence of the driving shape. As a model system we employ a two-level system driven by a periodic force and coupled to an environment of harmonic oscillators. We calculate LZSM interference patterns in the steady state and analyses them in real and Fourier space. In Sec. 4.2, we introduce the Floquet-Bloch-Redfield formalism which provides our numerical solutions. Section 4.3 is devoted to the LZSM pattern in real space which is governed by the coupling operator to the bath. In Sec. 4.4 we discuss the Fourier transform of the LZSM patterns exhibiting characteristic arc structure that decay exponentially. Moreover, we determine the decay of the arcs as a function of the bath parameters. Finally, in Sec. 4.5 we investigate LZSM patterns with general periodic driving and derive an analytic description of the corresponding structures in Fourier space. We start with an introduction to the theory of LZSM Interference. The results of this chapter have been published previously in [138].

## 4.1 Periodic sweeping through an avoided crossing

Let us consider a two level system with a time-dependent level splitting $\varepsilon(t)$ and the tunnel coupling $\Delta$ between the level. This system is described by the Hamiltonian

$$H(t) = \frac{\hbar\varepsilon(t)}{2}\sigma_z + \frac{\hbar\Delta}{2}\sigma_x{}^{1}, \tag{4.1}$$

having the energy eigenvalues

$$E_{\pm}(t) = \pm\hbar\sqrt{\varepsilon(t)^2 + \Delta^2}, \tag{4.2}$$

and the eigenstates $|\pm\rangle$. The time-dependent level splitting is assumed to vary periodically in time, according to

$$\varepsilon(t) = \epsilon_0 + Af(t), \tag{4.3}$$

where $\epsilon_0$ is a static detuning and $f(t) = f(t+T)$ a periodic driving function. At this point, we assume that the driving is of the form

$$f(t) = \cos(\Omega t). \tag{4.4}$$

Figure 4.1(a) shows the spectrum of the Hamiltonian (4.1) for $A = 0$ as function of the static detuning $\epsilon_0$, forming an avoided crossing. Here, the dashed lines correspond to the diabatic state $|\uparrow\rangle$ and $|\downarrow\rangle$, i.e. the eigenstates of the Hamiltonian (4.1) with $\Delta = 0$. Switching on the driving (symbolized by the green line) with $A > \epsilon_0$ will sweep the

---

[1] Note that this Hamiltonian can be mapped onto: $H(t) = \frac{\hbar\varepsilon(t)}{2}\sigma_x - \frac{\hbar\Delta}{2}\sigma_z$, by applying a $\pi/2$ rotation around the $y$-axis. With a driving of the from Eq. (4.4) this Hamiltonian describes a two-level atom driven by a laser field [20].

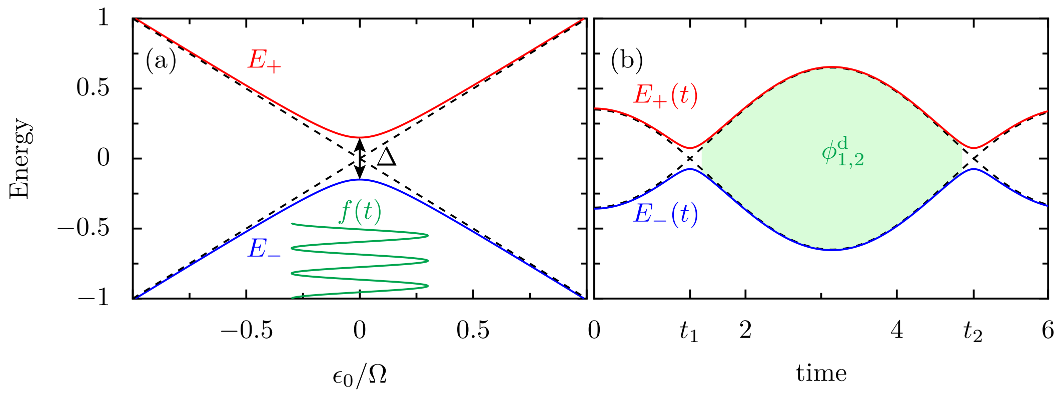

FIGURE 4.1: Periodic sweeping through an avoided level crossing: (a) shows the energy spectrum without driving as a function of the static detuning $\epsilon_0$. The red and blue line are the system eigenenergies given by (4.2), the corresponding eigenstates are also called adiabatic states. The black dashed lines show the energies of the diabatic states, i.e. eigenstates of the uncoupled system. The green line symbolizes the driving. (b) shows the time evolution of the spectrum as a function of time. The system passes through an avoided crossing at times $t_1$ and $t_2$. Between the avoided crossing it gains a dynamical phase $\phi^{\mathrm{d}}_{1,2}$. Parameter: $\Delta/\Omega = 0.2$, $A/\Omega = 1$.

qubit periodically through the avoided crossing. This leads to a series of successive non-adiabatic transitions, whenever the diabatic states cross. The probability for a single transition can be approximated by the Landau-Zener formula (compare with discussions in Sec. 3.3 and Appendix B) [20]

$$P_{\mathrm{LZ}} = \exp\Big(\frac{-\pi\Delta^2}{2A\Omega}\Big). \tag{4.5}$$

Note that, in contrast to the last section, here, we express the system in the adiabatic basis. If the amplitude $A$ is large as compared to the width of the crossing region, the system evolves adiabatically between two consecutive transitions at times $t_1$ and $t_2$, however, it will gain a dynamical phase [20] (see, Fig. 4.1 (b)):

$$\phi^{\mathrm{d}}_{1,2} = \frac{1}{2}\int_{t_1}^{t_2} \sqrt{\varepsilon(t)^2 + \Delta^2}\, dt. \tag{4.6}$$

Because of this phase, the wave functions belonging to the states with energies $E_+$ and $E_-$ interfere at the avoided crossing at $t_2$. This may increase the probability to undergo a Landau-Zener transition (constructive interference) or may diminish it (destructive interference).

### 4.1.1 Double passage

Before we discuss the general case, let us discuss the situation where we sweep through the avoided crossing exactly two times. This situation is depicted in Fig. 4.1, and an analog to a Mach-Zehnder interferometer [139,140] in optics [25] (see Fig. 4.2). The first

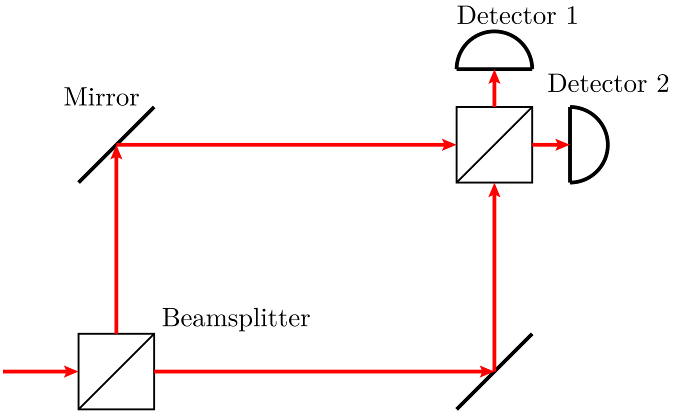

FIGURE 4.2: The Mach Zehnder interferometer: A light beam hits a 50:50 beamsplitter and gets divided into two beams. These beams get reflected by a mirror an pass a second beamsplitter, where they interfere. Depending on the optical path length the two beams enter the second beamsplitter with a phase difference, determining the intensity detected with detector 1 and 2.

transition at time $t_1$ divides the qubit wavefunction into two parts (one part is in the state $|+\rangle$, the other in $|-\rangle$), and plays the role of the first beamsplitter in Fig. 4.2. The probability to be either in state $|+\rangle$ or in state $|-\rangle$ after the transition is given in terms of the Landau-Zener formula, Eq. (4.5) and can be expressed using the S-Matrix [20]

$$S_{\mathrm{LZ}} = \begin{pmatrix} \sqrt{1-P_{\mathrm{LZ}}}\; e^{-i\varphi_{\mathrm{S}}t} & -\sqrt{P_{\mathrm{LZ}}} \\ \sqrt{P_{\mathrm{LZ}}} & \sqrt{1-P_{\mathrm{LZ}}}\; e^{i\varphi_{\mathrm{S}}t} \end{pmatrix}, \tag{4.7}$$

where we used the adiabatic eigenstates as a basis. In Eq. (4.7) an additional phase $\varphi_{\mathrm{S}}$, called the Stokes phase, is appearing (see [20] and references therein for the precise expression). This phase can be interpreted as a geometric phase and is related to the Berry phase [141].

After the first transition, the system evolves adiabatically until it approaches the second avoided crossing. Like a propagating light beam the qubit wavefunction gains a phase during its free evolution. This is described by the matrix

$$U_{t_2,t_1} = \begin{pmatrix} \exp(-i\phi^{\mathrm{d}}_{1,2}) & 0 \\ 0 & \exp(i\phi^{\mathrm{d}}_{1,2}) \end{pmatrix}. \tag{4.8}$$

The effect of the second transition is again described by Eq. (4.7). Starting in the ground state $|-\rangle$ after the second transition the system is in the state:

$$|\Psi_2\rangle = S_{\mathrm{LZ}}\, U_{t_2,t_1}\, S_{\mathrm{LZ}}\, |-\rangle\,, \quad \text{with} \quad |-\rangle = \begin{pmatrix} 0 \\ 1 \end{pmatrix}. \tag{4.9}$$

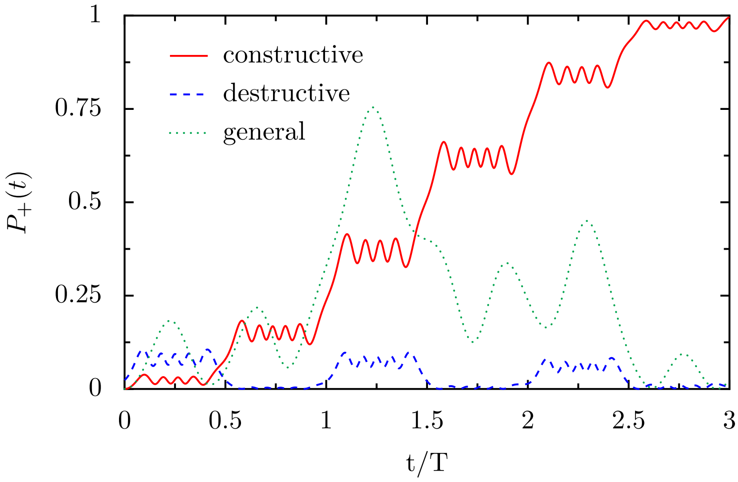

FIGURE 4.3: Time evolution of periodically driven qubit. The plot shows the probability to be in the excited state. For $A \gg \Delta$ and $A \gg \Omega$ the qubit undergoes a series of well separated LZ-transitions, and interferes constructively (red solid line) or destructively (blue dashed line) at the transitions. Parameters: $A/\Omega = 15$, $\Delta/\Omega = 0.8$, $\epsilon_0/\Omega = 1$ (constructive), and, respectively, $\epsilon_0/\Omega = 0.5$ (destructive). The green dotted line shows $P_+(t)$ for $A/\Omega = 3$, $\Delta/\Omega = 0.8$ and $\epsilon_0/\Omega = 0.3$. Results obtained by numerical integration of the Schrödinger equation with Hamiltonian (4.1).

It follows, that the probability $P_+ = |\langle + |\Psi_2\rangle|^2$ to be in the excited state $|+\rangle = (1,0)^T$ after sweeping twice through the crossing is given by

$$P_+ = 4P_{\rm LZ}(1 - P_{\rm LZ})\sin^2(\Phi_{\rm St}), \tag{4.10}$$

where $\Phi_{\rm St} = \phi^{\rm d}_{1,2} + \varphi_{\rm S}$ is the so-called Stückelberg phase [17, 20]. The corresponding Stückelberg oscillations have been observed experimentally, for example in the microwave excitation of Rydberg atoms [142]. While for destructive interference Eq. (4.10) vanishes, for constructive interference we have $P_+ = 4P_{\rm LZ}(1 - P_{\rm LZ})$, i.e. the probability is twice as large as one would expect for two successive transition without interference [20].

### 4.1.2 Multiple transitions

Sweeping through an avoided crossing many times induces multiple LZ-transition and may lead to a complex dynamics. In Fig. 4.3, we plot the probability to be in the excited state $P_+(t) = |\langle + |\Psi(t)\rangle|^2$ as a function of time, where $|\Psi(t)\rangle$ is the solution of the Schrödinger equation with the initial state $|-\rangle$ and the Hamiltonian (4.1). If the amplitude $A$ is large as compared to the width of the avoided crossing, the dynamics can be described as a series of separated transition, and is well approximated by a generalisation of the model[2] presented in the last subsection [20]. The red solid and the blue dashed line in Fig. 4.3 depict the special cases of constructive (red solid) and, destructive interference (blue dashed), respectively, at the avoided crossing. While in

---

[2] Also called “adiabatic impulse model” in the literature.

the latter cases one can clearly distinguish between the individual transitions, for general parameters this is no longer possible (green dotted line).

In order to derive an analytical expression for the systems time evolution, we transform the Hamiltonian, Eq. (4.1), to a rotating frame by applying the unitary transformation [20, 143, 144]:

$$U_{\mathrm{r}}(t) = \exp\Big(-\frac{i}{2\hbar}V(t)\Big), \tag{4.11}$$

with the operator

$$V(t) = \int_0^t dt'\ A\cos(\Omega t')\sigma_z = \frac{A}{\Omega}\sin(\Omega t)\sigma_z. \tag{4.12}$$

Using the identity

$$e^{ix\sin(t)} = \sum_{n=-\infty}^{\infty} J_n(x)e^{int}, \tag{4.13}$$

with $J_n(x)$ being the $n$th Bessel function of the first kind [145], this yields the transformed Hamiltonian:

$$H_{\mathrm{r}} = \sum_{n=-\infty}^{\infty} \frac{\Delta_n}{2}\big(e^{-in\Omega t}\sigma_+ + e^{in\Omega t}\sigma_-\big) + \frac{\epsilon_0}{2}\sigma_z, \tag{4.14}$$

with $\sigma_\pm = \sigma_x \pm i\sigma_y$ and the renormalized tunnel matrix element

$$\Delta_n = J_n\Big(\frac{A}{\hbar\Omega}\Big)\Delta. \tag{4.15}$$

In order to eliminate the time dependence of Eq. (4.14) we apply a second transformation $U_k(t) = \exp(ik\Omega t/2)$ and assume that we are close to a $k$-photon resonance, where $k\Omega \approx \sqrt{\epsilon_0^2 + \Delta^2} \approx |\epsilon_0|$. If the coupling $\Delta$ is sufficiently weak, we can adopt a RWA, supposing that in the vicinity of the resonance $\delta_n = n\Omega - \epsilon_0 \approx 0$ the rapidly oscillating term with $n \neq k$ can be neglected (compare with the discussion after Eq. (3.5)). This leads to the effective Hamiltonian:

$$H_n^{\mathrm{eff}} = \frac{\delta_n}{2}\sigma_z + \frac{\Delta_n}{2}\sigma_x. \tag{4.16}$$

Hence, we have converted the Hamiltonian to a form that is time independent. Note that in Eq. (4.16), the renormalized tunnel coupling $\Delta_n$ is appearing, i.e., the original coupling constant $\Delta$ is multiplied by the Bessel function $J_n(A/\hbar\Omega)$. At certain values of $A/\hbar\Omega$ the Bessel function vanishes and the tunneling gets suppressed. This phenomenon is called *coherent destruction of tunneling* [146]. From Eq. (4.16) the Schrödinger equation can

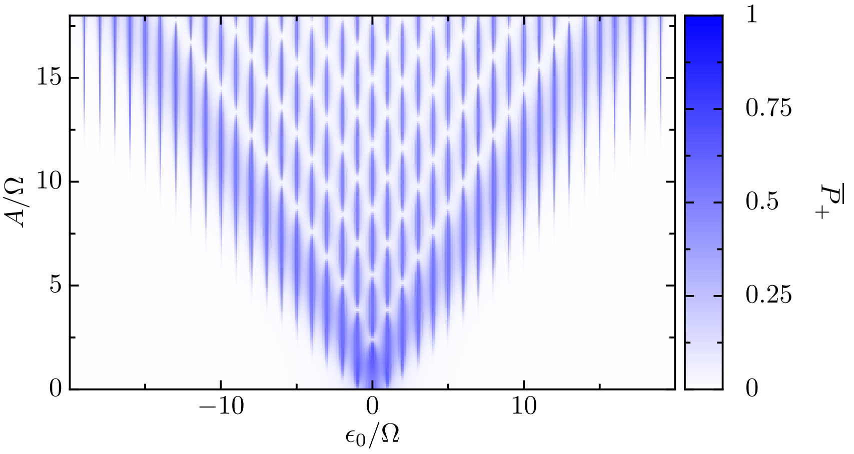

FIGURE 4.4: Landau-Zener-Stückelberg-Majorana interference pattern: The excited state population $\overline{P}_+(\epsilon_0, A)$, given by Eq. (4.18), as a function of amplitude $A$ and static detuning $\epsilon_0$. Parameters: $\Delta/\Omega = 0.5$.

be solved readily to yield the excited state probability [20]

$$P_+^{(n)}(t) = \frac{1}{2}\frac{\Delta_n^2}{\delta_n^2 + \Delta_n^2}\Big(1 - \cos\big(\Omega^{(n)}t\big)\Big), \tag{4.17}$$

with $\Omega^{(n)} = \sqrt{\delta_n^2 + \Delta_n^2}$. Averaging over the period $2\pi/\Omega^{(n)}$, and summing up all $n$-photon resonances leads to

$$\overline{P}_+(\epsilon_0, A) = \frac{1}{2}\sum_n \frac{\Delta_n^2}{\delta_n^2 + \Delta_n^2}. \tag{4.18}$$

The notation of Eq. (4.18) already indicates that the excited state probability is a function of the static detuning $\epsilon_0$ and the amplitude $A$. Indeed, in many experiments with solid state qubits these parameter can be controlled to a high degree [25–27,29–32]. Figure 4.4 shows $\overline{P}_+(\epsilon_0, A)$. One observes an interference pattern called *Landau-Zener-Sückelberg-Majorana (LZSM) interference pattern* with several peaks restricted to an area where $A < \epsilon_0$, because the amplitude of the driving must exceed the detuning in order to induce transitions. The peaks appear when $\delta_n = 0$ and hence can be interpreted as multi-photon resonances. At certain values of $A$, where the Bessel functions $J_n$ vanish, these resonances are suppressed because of coherent destruction of tunneling (as discussed above).

Hitherto, we considered a closed system. As already mentioned in the previous chapter, this often is a deficient approximation, especially if one is dealing with solid state qubits, at long times beyond the coherence time. In order to take into account environmental effects, one may describe the system dynamics in terms of a master equation as in Sec. 3.4, however, if the system is driven by a strong external field, the driving affects the system–bath coupling and complicates the solution of the master equation [22]. In order to overcome this issue, we use the fact, that the system is driven by a periodic force and empoly Floquet theory to derive a *Floquet-Redfield master equation* in the next section.

## 4.2 Bloch-Redfield equation and Floquet theory

Symmetry is one of the deepest concepts in modern physics and symmetry considerations are often at the beginning of a theoretical analysis, or allow to simplify a complex problem. For example, in condensed matter physics the periodicity of the lattice, i.e. its (discrete) translation symmetry, allows to write the electron wavefuction in terms of Bloch waves, and gives rise to the electronic band structure. In periodically time-dependent system an analogous approach, called Floquet theory, applies which we will use in the following to derive a master equation for a periodically driven quantum system in contact with an environment.

### 4.2.1 Floquet theory

Consider the Schrödinger equation written in the homogeneous form

$$\left(H(t) - i\hbar\frac{\partial}{\partial t}\right)|\Psi(t)\rangle = 0 \tag{4.19}$$

with the time-dependent Hamiltonian $H(t)$ obeying the discrete time translation symmetry

$$H(t) = H(t+T), \qquad T = \frac{2\pi}{\Omega}. \tag{4.20}$$

The symmetry operator $S_T : t \to t+T$, which translates a given state by one period $T$, commutes with $H(t) - i\hbar\frac{\partial}{\partial t}$, and hence the eigenstates of $S_T$ are, up to a phase factor, also solution of the Schrödinger equation (4.19). One has

$$S_T\,|\Psi(t)\rangle = |\Psi(t+T)\rangle = e^{i\Phi}\,|\Psi(t)\rangle \tag{4.21}$$

Using the “plane wave” ansatz

$$|\Psi(t)\rangle = e^{-i\varepsilon t/\hbar}\,|\Phi(t)\rangle\,, \quad \text{with} \quad \varepsilon = \hbar\Phi/T, \tag{4.22}$$

one effectively separates the timescales, where the long time behavior is dominated by the phase factor with the *quasi-energy* $\varepsilon$ and the dynamics within one period $T$ is determined by the *Floquet states* $|\phi(t)\rangle$ which obey

$$|\Phi(t)\rangle = |\Phi(t+T)\rangle\,. \tag{4.23}$$

The previous reasoning can be summed up in the *Floquet theorem* stating that the Scrödinger equation (4.19) possesses a complete set of solutions [22, 147, 148]

$$|\Psi_\alpha(t)\rangle = e^{-i\varepsilon_\alpha t/\hbar} |\Phi_\alpha(t)\rangle \quad \text{with} \quad |\Phi_\alpha(t)\rangle = |\Phi_\alpha(t+T)\rangle \,, \tag{4.24}$$

Thus, its general solution can be expressed as the superposition

$$|\Psi(t)\rangle = \sum_\alpha c_\alpha e^{-i\varepsilon_\alpha t/\hbar} |\Phi_\alpha(t)\rangle \,, \tag{4.25}$$

where the coefficients $c_\alpha = \langle \Phi_\alpha(0) \mid \Psi(0)\rangle$ depend on the initial condition. Note that Floquet states $|\Phi_\alpha(t)\rangle$ are in general no solutions of the Schrödinger equation. With the *Floquet operator*

$$\mathcal{H}(t) = H(t) - i\hbar\frac{\partial}{\partial t}, \tag{4.26}$$

one finds the eigenvalue equation

$$\mathcal{H}(t) |\Phi_\alpha(t)\rangle = \varepsilon_\alpha |\Phi_\alpha(t)\rangle \,. \tag{4.27}$$

Hence, one obtains the solution of Eq. (4.25) by solving Eq. (4.27). Moreover, from Eq. (4.27) one derives that

$$\varepsilon_\alpha^{(n)} = \varepsilon_\alpha + n\hbar\Omega, \tag{4.28}$$

with $n = 0, \pm 1, \pm 2, \ldots$, also solve Eq. (4.27). The quasi-energies $\varepsilon_\alpha$ hence belongs to a whole class of solutions and it is sufficient to restrict on the quasi-energies within one Brillouin zone $E - \hbar\Omega/2 < \varepsilon_\alpha < E + \hbar\Omega/2$, for any $E$. Owing their time periodicity, the Floquet states $|\Phi_\alpha(t)\rangle$ can be expressed as Fourier series

$$|\Phi_\alpha(t)\rangle = \sum_k e^{-ik\Omega t} |c_{\alpha,k}\rangle \,, \tag{4.29}$$

with

$$|c_{\alpha,k}\rangle = \frac{1}{T}\int_0^T dt\; e^{ik\Omega t} |\Phi_\alpha(t)\rangle \,. \tag{4.30}$$

#### 4.2.1.1 Floquet theory in Sambe space

The postulates of quantum mechanics tell us that the state $|\Psi(t)\rangle$ is an element of a Hilbert space $\mathcal{R}$. For the Floquet operator (4.26) it is convenient to introduce the composite Hilbert space $\mathcal{R} \otimes \mathcal{T}$ [149], sometimes also called Sambe space, where $\mathcal{R}$ is the space of square integrable functions on configuration space and $\mathcal{T}$ the space of $T$-periodic function. On $\mathcal{R}$ there exists a countable complete set $\{|n\rangle\}$ of orthonormal states with

$$\langle n|n'\rangle = \delta_{n,n'}, \qquad \sum_n |n\rangle \langle n| = 1. \tag{4.31}$$

Accordingly, we define on $\mathcal{T}$ the inner product

$$(u,v)=\frac{1}{T}\int_0^T dt\ u^*(t)v(t). \tag{4.32}$$

From Fourier analysis it follows that the functions $\exp(ik\Omega t)$, with $k=0,\pm1,\pm2$ form an orthonormal basis of $\mathcal{T}$. Consequently, on the composite Hilbert space $\mathcal{R}\otimes\mathcal{T}$ the inner product then is given by

$$\langle\langle\Phi_\alpha|\Phi_\beta\rangle\rangle=\frac{1}{T}\int_0^T dt\langle\Phi_\alpha(t)|\Phi_\beta(t)\rangle=\delta_{\alpha,\beta}, \tag{4.33}$$

where we introduced the notation $|\Phi_\beta\rangle\rangle$ for the elements of $\mathcal{R}\otimes\mathcal{T}$. An orthonormal basis of $\mathcal{R}\otimes\mathcal{T}$ is defined by the set of states $\{|\Phi_n^k\rangle\rangle\}$ with

$$\langle t|\Phi_n^k\rangle\rangle=e^{ik\Omega t}\,|n\rangle\,. \tag{4.34}$$

#### 4.2.1.2 Numerical approach – Method of Floquet matrix

Except for some special cases (see e.g. [22,148]), exactly solvable quantum systems with explicit time dependence are scarce. Therefore, one generally has to invoke numerical methods. Here, Floquet theory can be a powerful and elegant tool to numerically determine the dynamics of a given system. The literature describes different computational methods for the determination of the Floquet states $|\Phi_\alpha(t)\rangle$ and the quasi-energies $\varepsilon_\alpha$ [22,148]. Here, we employ the Floquet matrix method which is based on solving the eigenvalue equation Eq. (4.27). Starting with a general time-periodic Hamiltonian written as Fourier series,

$$H(t)=H_0+\sum_{l=0}^{\infty}A_l\sin(\Omega t+\varphi_l)H_l, \tag{4.35}$$

We transform the eigenvalue equation (4.27) to in Sambe space, where it reads

$$\sum_{n',k'}\mathcal{H}_{nn'}^{kk'}\ \Phi_{n',\alpha}^{k'}=\varepsilon_\alpha\ \Phi_{n,\alpha}^{k}. \tag{4.36}$$

Here, we introduced the Floquet matrix

$$\mathcal{H}_{nn'}^{kk'}=\left(\langle n|\,H_0\,|n'\rangle+k\hbar\Omega\delta_{n,n'}\right)\delta_{k,k'}+\sum_{l=1}^{\infty}\frac{A_l}{2i}\langle n|\,H_l\,|n'\rangle\left(e^{i\varphi_l}\delta_{k,k'+l}-e^{-i\varphi_l}\delta_{k,k'-l}\right), \tag{4.37}$$

with eigenstates

$$\Phi_{n,\alpha}^{k}=\langle\langle\Phi_n^k\mid\Phi_\alpha\rangle\rangle=\langle n\mid c_{\alpha,k}\rangle. \tag{4.38}$$

Hence, by solving Eq. (4.36) one finds the Fourier coefficients $|c_{\alpha,k}\rangle$ and is able to reconstruct the Floquet states in terms of Eq. (4.29). Together with the eigenvalues $\varepsilon_\alpha$, the solution of the Schrödinger equation can readily be found. As basis states $|n\rangle$ for the Hilbert space $\mathcal{R}$, one usually employs the eigenstates of the undriven Hamiltonian $H_0$. Note that dimension of the Sambe space and therefore of the Floquet matrix (4.37) is infinite. Thus, one has to cut the Sambe space index $k$ at a certain value $k_{\max}$. This is justified because the coefficients of $|c_{\alpha,k}\rangle$ vanish for large $k$. In general, $k_{\max}$ has to be chosen $\propto \max\{A/\hbar\Omega, \delta E_0/\hbar\Omega\}$, where $\delta E_0$ is the typical energy splitting of the Hamiltonian $H_0$. Additionally $k_{\max}$ may depend on the number of Fourier coefficients $A_l$ required for $H(t)$.

### 4.2.2 Floquet-Redfield master equation

The effect of the environment on the system dynamics is represented using the system-bath model (3.9), where the environment is described by a infinite sum of harmonic oscillators. Here, $H(t)$ is given by the system Hamiltonian (4.1). Moreover, we assume the system-bath coupling

$$H_{\mathrm{SB}} = \frac{1}{2} X \sum_{\nu} \hbar\lambda_{\nu}(a_{\nu}^{\dagger} + a_{\nu}), \tag{4.39}$$

where $\hbar\lambda_\nu$ are the system-oscillator coupling energies. For the qubit operator $X$ which couples to the bath, we consider $\sigma_x$ and $\sigma_z$ as well as a linear combination of the two. According to their orientation on the Bloch sphere with respect to the driving, we refer to the coupling as transverse ($\sigma_x$) and longitudinal ($\sigma_z$), respectively. Following the approximation steps of Sec. 3.4, we arrive, mutatis mutandis, at the Markovian master equation (3.18) for the density matrix $\rho$ in the interaction picture

$$\frac{d}{dt}\tilde{\rho}_{\mathrm{S}}(t) = -\frac{i}{\hbar}\int_0^{\infty} ds\, \mathrm{tr}_B[\tilde{H}_{\mathrm{SB}}(t), [\tilde{H}_{\mathrm{SB}}(t-s), \tilde{\rho}_{\mathrm{S}}(t) \otimes \rho_{\mathrm{B}}]. \tag{4.40}$$

Introducing the spectral density $J(\omega) = \pi \sum_\nu |\lambda_\nu|^2 \delta(\omega - \omega_\nu)$, and the symmetric and the antisymmetric bath correlation functions

$$\begin{aligned} \mathcal{S}(\tau) &= \frac{1}{2}\langle\{B(\tau), B(0)\}\rangle_{\mathrm{eq}} \\ &= \frac{1}{\pi}\int_0^{\infty} d\omega J(\omega) \coth(\hbar\omega\beta/2)\cos(\omega\tau), \end{aligned} \tag{4.41}$$

$$\begin{aligned} \mathcal{A}(\tau) &= \frac{1}{2}\langle[B(\tau), B(0)]\rangle_{\mathrm{eq}} \\ &= \frac{1}{\pi}\int_0^{\infty} d\omega J(\omega)\sin(\omega\tau), \end{aligned} \tag{4.42}$$

respectively, with the collective bath coordinate

$$B(t) = \sum_{\nu} \lambda_\nu \{a_\nu^{\dagger} \exp(i\omega_\nu t) + a_\nu \exp(-i\omega_\nu t)\} \tag{4.43}$$

and $\langle \dots \rangle_{\text{eq}}$ being the average with respect to the thermal equilibrium of the environment, Eq. (4.40) yields

$$\frac{d}{dt}\rho = -\frac{i}{\hbar}[H(t),\rho] - \frac{1}{4}\int_0^\infty d\tau \Big( \mathcal{S}(\tau)[X,[\tilde{X}(t-\tau,t),\rho]] + \mathcal{A}(\tau)[X,\{\tilde{X}(t-\tau,t),\rho\}] \Big). \tag{4.44}$$

where $\{A,B\} = AB + BA$ denotes the anti-commutator and $\tilde{X}(t',t)$ is a shorthand notation for $U^\dagger_{t,t'} X U_{t,t'}$, with $U$ being the propagator for the coherent qubit dynamics. In order to solve Eq. (4.44) numerically, we express it in the basis of Floquet states $|\Phi_\alpha(t)\rangle$. This yields

$$\frac{d}{dt}\rho_{\alpha\beta}(t) = -\frac{i}{\hbar}(\varepsilon_\alpha - \varepsilon_\beta)\rho_{\alpha\beta}(t) + \sum_{\alpha'\beta',k} e^{-ik\Omega t}\mathcal{D}^{(k)}_{\alpha\beta,\alpha'\beta'}\rho_{\alpha'\beta'}(t), \tag{4.45}$$

with $\rho_{\alpha\beta}(t) = \langle \Phi_\alpha(t)|\,\rho\,|\Phi_\beta(t)\rangle$, and the $k$th Fourier component of the dissipative superoperator

$$\begin{aligned} \mathcal{D}^{(k)}_{\alpha\beta,\alpha'\beta'} = & \sum_{k'} (N_{\alpha\alpha',k'} + N_{\beta\beta',k'-k}) X_{\alpha\alpha',k'} X_{\beta'\beta,k-k'} \\ & + \delta_{\beta,\beta'} \sum_{k',\beta''} N_{\beta''\alpha',k-k'} X_{\alpha\beta'',k'} X_{\beta''\alpha',k-k'} \\ & + \delta_{\alpha,\alpha'} \sum_{k',\alpha'} N_{\alpha''\beta',k'-k} X_{\beta'\alpha'',k-k'} X_{\alpha''\beta,k'}. \end{aligned} \tag{4.46}$$

In Eq. (4.46) we assumed a Ohmic spectral density

$$J(\omega) = \frac{1}{2}\pi\alpha\omega \tag{4.47}$$

with the dimensionless dissipation parameter $\alpha$. Moreover, we use the thermal coefficients

$$N_{\alpha\beta,k} = N(\varepsilon_\alpha - \varepsilon_\beta + k\hbar\Omega) \quad \text{with} \quad N(\omega) = \alpha\omega n_{\text{th}}(\omega), \tag{4.48}$$

and the bosonic thermal occupation number $n_{\text{th}}(\omega) = (e^{\beta\hbar\omega} - 1)^{-1}$. Finally, we introduced the transition matrix elements

$$X_{\alpha\beta,k} = \frac{1}{T}\int_0^T dt\, e^{ik\Omega t}\langle\Phi_\alpha(t)|X|\Phi_\beta(t)\rangle = \sum_n \langle c_{\alpha,n}|\,X\,|c_{\beta,n+k}\rangle\,. \tag{4.49}$$

In the long-time limit, the system relaxes to a steady state which obeys the time-periodicity of the driving, $\rho_\infty(t) = \rho_\infty(t+T)$. Hence we can write the density matrix as Fourier decomposition

$$\rho_\infty(t) = \sum_k e^{-ik\Omega t}\rho^{(k)} \tag{4.50}$$

Since for periodic driving also the systems Liouville operator $\mathcal{L}(t)$ is periodic, we can also expand it as a Fourier series so that the Liouville equation can be expressed as

$$\frac{d}{dt}\rho(t) = \sum_k e^{-ik\Omega t}\,\mathcal{L}_k\,\rho(t). \tag{4.51}$$

Together with Eq.(4.50) this yields the steady state condition

$$-i\hbar k\Omega\rho^{(k)} = \sum_{k'} \mathcal{L}^{(k-k')}\rho^{(k')}, \tag{4.52}$$

which can be written in matrix form:

$$\begin{pmatrix} -i\hbar N\Omega\rho^{(N)} \\ \vdots \\ 0 \\ \vdots \\ i\hbar N\Omega\rho^{(-N)} \end{pmatrix} = \begin{pmatrix} \mathcal{L}^{(0)} & \dots & \mathcal{L}^{(N)} & \dots & \mathcal{L}^{(2N)} \\ \vdots & \ddots & \vdots & \ddots & \vdots \\ \mathcal{L}^{(N)} & \dots & \mathcal{L}^{(0)} & \dots & \mathcal{L}^{(-N)} \\ \vdots & \ddots & \vdots & \ddots & \vdots \\ \mathcal{L}^{(-2N)} & \dots & \mathcal{L}^{(-N)} & \dots & \mathcal{L}^{(0)} \end{pmatrix} \begin{pmatrix} -i\hbar N\Omega\rho^{(N)} \\ \vdots \\ 0 \\ \vdots \\ i\hbar N\Omega\rho^{(-N)} \end{pmatrix}. \tag{4.53}$$

Comparing Eq. (4.52) with Eq. (4.45), one recognizes that the Fourier components $\mathcal{L}^{(k)}$ can be computed in the Floquet basis, and its matrix elements are

$$\mathcal{L}^{(k)}_{\alpha\beta,\alpha'\beta'} = \begin{cases} -i(\varepsilon_{\alpha'} - \varepsilon_{\beta'})\delta_{\alpha,\alpha'}\delta_{\beta,\beta'} + \mathcal{D}^{(0)}_{\alpha\beta,\alpha'\beta'}, & \text{for } k=0 \\ \mathcal{D}^{(k)}_{\alpha\beta,\alpha'\beta'}, & \text{else} \end{cases} \tag{4.54}$$

Plugging Eq. (4.54) into Eq. (4.52) directly leads to

$$-i\hbar k\Omega\rho^{(k)}_{\alpha\beta} = \sum_{\alpha',\beta',k'} \mathcal{L}^{(k-k')}_{\alpha\beta,\alpha'\beta'}\rho^{(k')}_{\alpha'\beta'}. \tag{4.55}$$

In Eq. (4.53), we truncate the system of equations (4.55) at $k = N$. In practice, at least in our studies, numerical convergence was already obtained for $N \leq 5$ i.e., for truncation at the fifth sideband, even when the Floquet states may contain many more relevant sidebands. Setting $N = 0$ reproduces the so called moderate rotating wave approximation (RWA) [150] which is valid when dissipative effects are relevant only on time scales much larger than one period $T$ of the driving. Note that in contrast to Eq. (4.45), the master equation in moderate RWA

$$\frac{d}{dt}\rho_{\alpha\beta}(t) = \sum_{\alpha'\beta'} \mathcal{L}^{(0)}_{\alpha\beta,\alpha'\beta'}\rho_{\alpha'\beta'}(t), \tag{4.56}$$

is in general not invariant under shifts of the Brillouin zone, because, $\varepsilon_\alpha \to \varepsilon_\delta = \varepsilon_\alpha + n\hbar\Omega$ does in general not imply $\mathcal{L}^{(0)}_{\alpha\beta,\alpha'\beta'} = \mathcal{L}^{(0)}_{\delta\beta,\alpha'\beta'}$. This can lead to artefacts which also reflect themselves in the steady state solution. Alternatively, one can additionally perform the full rotating wave approximation and set

$$\varepsilon_\alpha - \varepsilon_\beta = \varepsilon_{\alpha'} - \varepsilon_{\beta'} \tag{4.57}$$

which, for a non-degenerate spectrum, is fulfilled if $(\alpha, \beta) = (\alpha', \beta')$ or $(\alpha, \alpha') = (\beta, \beta')$. Thus, it leads to a decoupling of diagonal and off-diagonal elements and the master equation becomes

$$\dot{\rho}_{\alpha\alpha}(t) = \sum_{\alpha'} \mathcal{L}_{\alpha\alpha,\alpha'\alpha'} \rho_{\alpha'\alpha'} \tag{4.58}$$

$$\dot{\rho}_{\alpha\beta}(t) = \mathcal{L}_{\alpha\beta,\alpha\beta} \rho_{\alpha\beta}(t), \qquad \alpha \neq \beta. \tag{4.59}$$

In full RWA, the master equation is again invariant under shifts of the Brillouin zone, despite that this approximation is even more restrictive than the moderate RWA [150]. In contrast to the previous equations, it can be written in Lindblad form (compare Sec. 3.4.1) where the Lindblad operators $\Gamma_{\alpha\beta}(t) = |\Phi_\alpha(t)\rangle \langle\Phi_\beta(t)|$ act as shift operators for Floquet states [150, 151]. From Eq. (4.58) and Eqs. (4.59) it follows that in the steady state, the density matrix is diagonal in the Floquet basis. Moreover, in full RWA the stationary state will not depend on the dissipation strength $\alpha$. For vanishing temperature one will always end up in the Floquet states with the lowest energy.

## 4.3 Steady State LZSM patterns

### 4.3.1 Numerical results

In Section 4.1, we considered the average probability to be in the excited state starting in the initial state $|-\rangle$. In the presence of a heat bath, the system state in the long-time limit typically relaxes to a unique steady state which is independent of the initial state. Therefore, we consider time averages of observables such as populations when the system has reached its steady state. We define

$$P_{\mathrm{ex}}(\epsilon_0, A) := \frac{1}{T} \int_0^T dt\, \langle + | \rho_\infty(t) | + \rangle, \tag{4.60}$$

where $\rho_\infty(t)$ is the periodic long-time solution of the master equation. Thus, $P_{\mathrm{ex}}$ directly relates to the Fourier coefficients in Floquet basis, $\rho^{(k)}_{\alpha\beta}$. Alternatively, we could evaluate the probability to be in one of diabatic states, i.e., the eigenstates of the uncoupled Hamiltonian. Since in the vast part of the parameter space considered, the qubit is strongly biased, i.e., $\Delta \ll |\epsilon_0|$, the choice is of minor practical relevance.

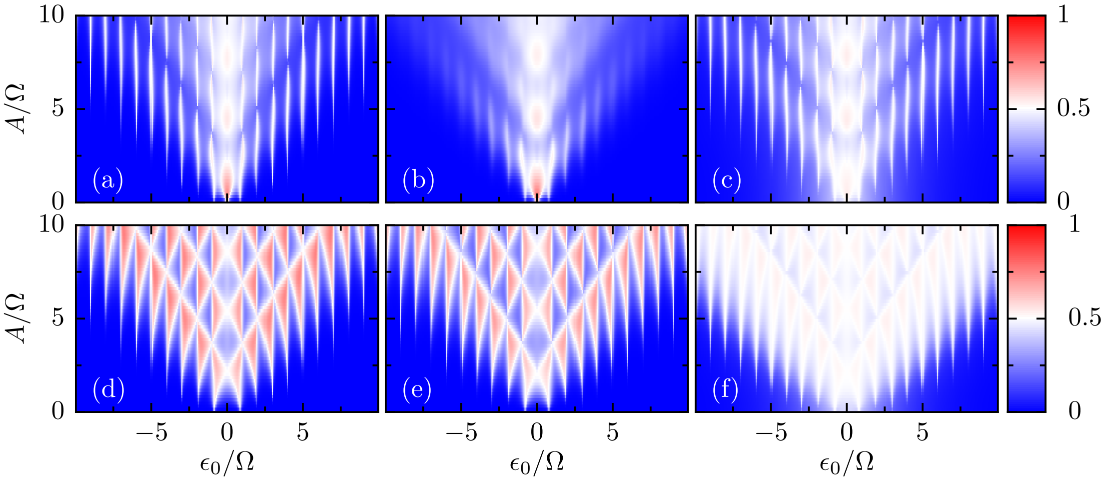

FIGURE 4.5: Non-equilibrium population $P_{\text{ex}}$ as a function of the detuning $\epsilon_0$ and the driving amplitude $A$ for $f(t) = \cos(\Omega t)$. The qubit-bath coupling $H_{\text{int}}$ is determined by $X = \sigma_x$ (a)–(c) and $X = \sigma_z$ (d) –(f), while $\Delta = 0.5\Omega$. Moreover, we consider different bath coupling strength $\alpha$ and temperatures $1/\beta$. (a), (d): $\alpha = 10^{-3}$, $1/\beta = 0.1\hbar\Omega$, (b), (e): $\alpha = 0.05$, $1/\beta = 0.1\hbar\Omega$ and (c), (f): $\alpha = 10^{-3}$, $1/\beta = 2\hbar\Omega$.

Let us first consider the transverse coupling ($X = \sigma_x$). The resulting pattern (Fig. 4.5(a)-(c))[3] is characterized by resonance islands which, as a function of the detuning $\epsilon_0$, are Lorentzians. As a function of the amplitude $A$, their shape follows approximately the squares of Bessel functions. Qualitatively, the patterns resemble the one without dissipation in Fig. 4.4. This behavior was also predicted for the current through ac-gated double quantum dots [34, 143]. Moreover, it has been observed with good resolution in various experiments [25, 27, 28, 30, 33, 34].

If the bath couples longitudinally with respect to the driving, i.e., when both the ac field and the environment enter via $\sigma_z$, the pattern changes qualitatively. As it can be appreciated in Fig. 4.5(d)-(f), the Lorentzian peaks turn into a triangular structures. This kind of bath coupling should be relevant for a charge qubit in a Cooper-pair box driven by an ac gate voltage, while being sensitive to environmental charge fluctuations. The LZSM pattern for such a case has been measured in Ref. [26] and indeed exhibits some similarity with Fig. 4.5(a)-(c). Recent experiments [152] have obtained such triangular patterns with much higher resolution.

A quantitative analysis of the peaks for longitudinal coupling (cf. Fig. 4.6) reveals that the maxima are shifted towards smaller $\epsilon_0$. Moreover, the maximal value of $P_{\text{ex}}$ exceeds the value of 0.5, implying population inversion in a two-level system. Physically, this can be explained by the observation that for longitudinal coupling the driving and the bath couple to the same coordinate. Hence, driving and bath can corporate and it is possible to excite a virtual state with $n\hbar\Omega > \epsilon_0$ from which one decays to $|+\rangle$. If this process

---

[3] The differences between these plots are discussed below.

is faster than the decay to the ground state, the population can be inverted [153–155]. This also explains the shift of the maxima towards smaller $\epsilon_0$.

In order to study the effect of the bath temperature and the coupling strength we consider different values of dissipation strength $\alpha$ and temperature $1/\beta$. Therefore, we compare the patterns with rather small values of $\alpha$ and $1/\beta$ (Figs. 4.5 (a),(d)) with patterns where either the coupling $\alpha$ is increased (Figs. 4.5(b),(e)), or the temperature $1/\beta$ (Figs. 4.5(c),(f)).

While for increasing $\alpha$ and transverse bath coupling the pattern gets washed out distinctly (Fig. 4.5(b)), the pattern with longitudinal coupling almost stays unchanged (Fig. 4.5(e)). This also suggests that in the latter case the pattern not only gets damped out by the environmental fluctuations, but is a result of the interplay between driving and dissipation.

On the other hand, for increasing temperature (Fig. 4.5(c),(f)) both patterns get washed out. Interestingly, the pattern with transverse bath coupling 4.5(c) seems to be less sensitive to an increasing by temperature than the pattern with longitudinal coupling 4.5(f). Here, the peak structure vanishes almost completely, however, the residual excited state population is not going to zero, but is striving towards $P_{\text{ex}} = 0.5$. This stems from the fact that for $X = \sigma_z$ the bath induces transitions between the eigenstates, when the Hamiltonian is dominated by $\Delta\sigma_x$, i.e. between $|\pm\rangle \approx |\uparrow\rangle \pm |\downarrow\rangle$. Most of the time, however, the Hamiltonian is dominated by $(\epsilon_0 + A\cos(\Omega t))\sigma_z$, so that the excited state coincides with a diabatic state $|+\rangle = |\uparrow\rangle$ or, $|+\rangle = |\downarrow\rangle$, respectively, depending on t. As a consequence, the bath propels the system a state $\approx |\uparrow\rangle + |\downarrow\rangle$, corresponding to an average excited state population $P_{\text{ex}} = 0.5$.

### 4.3.2 Analysis of the resonance peaks

To analyse the peak structure of the interference patterns quantitatively, it is useful to plot horizontal cuts, i.e., to fix the amplitude $A$ and plot $P_{\text{ex}}$ as a function of $\epsilon_0$ (see Fig. 4.6). The plot reveals that the peaks for transverse coupling indeed are Lorentzians. For longitudinal coupling, the peaks are anti-symmetric. Moreover, we witness a triangular shaped background with a roughly linear decays in $|\epsilon_0|$ while being practically independent of the tunneling $\Delta$. Our aim is to explain these features within the Bloch equations for the qubit derived in Appendix C. We restrict the discussion to the limit of very low temperatures for which the interference pattern is most pronounced.

#### 4.3.2.1 Lorentzian peaks for the transverse coupling via $\sigma_x$

An analytic expression for the resonance peaks can be found within an approximation scheme for close-to-resonant excitation [20, 143]. For a bath coupling via $\sigma_x$, the calculation follows the one in [20]. We sketch it briefly, so that we can later highlight the

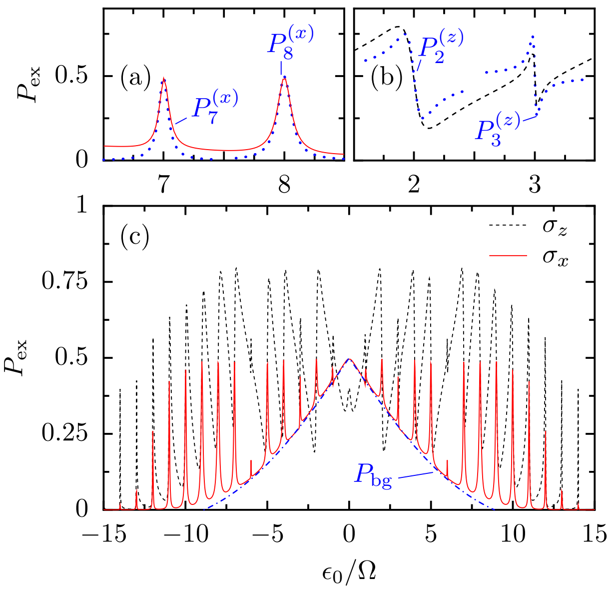

FIGURE 4.6: (Color online) Non-equilibrium population $P_{\rm ex}$ shown in Fig. 4.5 as a function of the detuning $\epsilon_0$ for the driving amplitude $A = 10\Omega$. (a) Comparison between numerical result with $\sigma_x$ coupling obtained with the Bloch-Redfield master equation (solid red) and the analytical solution (4.62) for the resonances with $n = 7, 8$ (dotted blue). (b) Comparison between numerical result with $\sigma_z$ coupling (dashed black) and the analytical solution (4.67) for n=2,3 (dotted blue). (c) Numerical results for $\sigma_x$ and $\sigma_z$ coupling plotted together with the analytical result for the off-resonant background predicted by Eq. (4.65).

differences to the case of a bath coupling via $\sigma_z$.

Embarking with the master equation (4.44), we consider the limit $\epsilon_0 \gg \Delta$ and assume that the driving frequency is close to resonance, i.e., $n\Omega = (\epsilon_0^2 + \Delta^2)^{1/2} \approx \epsilon_0$. In this regime the tunneling contribution proportional to $\Delta$ represents a perturbation to the free dynamics governed by $\frac{1}{2}\{\epsilon_0 + Af(t)\}\sigma_z$. In order to capture the coherent dynamics in large part, we apply the unitary transformation, Eq. (4.11), and average over one period of the driving, leading to the effective Hamiltonian (4.16). The corresponding equation of motion for the Bloch vector $\vec{s} = (\langle\sigma_x\rangle, \langle\sigma_y\rangle, \langle\sigma_z\rangle)^T$ with $\langle\ldots\rangle = \mathrm{tr}\{\ldots\rho_{\rm S}\}$ reads $\dot{\vec{s}} = \vec{B}_{\rm eff} \times \vec{s}$, where $\vec{B}_{\rm eff} = (\Delta_n, 0, -\delta_n)^T$.

For the dissipative dynamics, we distinguish two limiting cases. First, during the stage at which the qubit passes through the crossing, the tunneling term $\Delta\sigma_x/2$ dominates in the Hamiltonian (4.1), while the qubit-bath coupling essentially commutes with the Hamiltonian. Thus, it induces pure dephasing but no decay. Since for an Ohmic bath, the dephasing rate (C.7) is proportional to the temperature, it can be neglected in the limit under consideration.

For most of the time, however, the qubit Hamiltonian is dominated by the term proportional to $\sigma_z$, so that the bath causes transitions between the eigenstates $H_{\rm eff}$. We describe them by the Bloch equation (C.4) which together with the effective coherent dynamics reads

$$\dot{\vec{s}} = \begin{pmatrix} -\Gamma/2 & -\delta_n & 0 \\ \delta_n & -\Gamma/2 & \Delta_n \\ 0 & -\Delta_n & -\Gamma \end{pmatrix} \vec{s} - \begin{pmatrix} 0 \\ 0 \\ \Gamma \end{pmatrix}. \tag{4.61}$$

Notice that since we are only interested in the stationary state, we can ignore possible driving-induced renormalizations of the decay rates [156] and treat $\Gamma$ as phenomenological parameter. Nevertheless, we like to stress that our numerical treatment captures this renormalization. The steady state $\vec{s}(\infty)$ is easily obtained by matrix inversion and provides the non-equilibrium population

$$P_n^{(x)} = \frac{1}{2}(s_z + 1) = \frac{1}{2}\frac{\Delta_n^2/2}{(\epsilon_0 - n\Omega)^2 + \Delta_n^2/2 + \Gamma^2/4}. \tag{4.62}$$

While this expression holds close to the $n$th resonance, it vanishes far-off. Therefore, the global picture is simply given by the sum of the contributions of all resonances and reads

$$P_{\mathrm{ex}}^{(x)} = \sum_n P_n^{(x)}. \tag{4.63}$$

Such expressions have been found not only for non-equilibrium populations of driven qubits [20, 33] but also for the dc current through double quantum dots [34, 143].

In Fig. 4.6(a), we compare the numerically computed interference pattern for the $\sigma_x$ coupling with the analytical solution (4.62) at various resonances. While close to the resonances, i.e. for $\delta_n \ll \Delta$, the agreement is almost perfect, we observe small deviations between the resonances which mainly stem from the off-resonant background which gets more pronounced for small $\epsilon_0$. In the following, we derive an analytical formula for this background.

#### 4.3.2.2 Off-resonant background

We start our considerations by noticing that at low temperatures, the dissipative dynamics is mainly a decay towards the qubit ground state. Since for small tunneling $\Delta$ and large amplitude $A$, the (adiabatic) qubit levels form avoided crossings, the states $|\downarrow\rangle$ and $|\uparrow\rangle$ take turns in having lower energy, cf. dotted lines in Fig. 4.1. Within an adiabatic description, we employ the Bloch equation (C.4) and replace the $\epsilon$-dependent rate by its instantaneous value to obtain for the $z$-component of the Bloch vector $\vec{s} = \mathrm{tr}(\vec{\sigma}\rho)$ the equation of motion

$$\dot{s}_z = -\Gamma[\epsilon(t)]s_z - \pi\alpha\epsilon(t), \tag{4.64}$$

where $\epsilon(t) = \epsilon_0 + Af(t)$. If the decay is sufficiently slow, we can replace the time-dependent coefficients by their time averages $\overline{\epsilon(t)} = \epsilon_0$ and $\bar{\Gamma} \equiv \overline{\Gamma[\epsilon(t)]} \approx \alpha(2A + \epsilon_0^2/A)$, where the latter results from a Taylor expansion in $\epsilon_0/A$. Then, the steady state solution

$s_z = \pi\alpha\epsilon_0/\bar{\Gamma}$ corresponds to the non-equilibrium population

$$P_{\rm bg} = \frac{1}{2} - \frac{\pi\epsilon_0 A}{4A^2 + 2\epsilon_0^2}. \tag{4.65}$$

The dashed-dotted line in Fig. 4.6(c) shows that this estimate indeed describes the triangular shaped background rather well which, in turn, confirms the underlying adiabatic picture.

#### 4.3.2.3 Anti-symmetric resonances for the longitudinal coupling via $\sigma_z$

For longitudinal coupling, the situation is complementary to the transverse case. Outside the crossing, the bath couples to a good quantum number of the qubit and, thus, creates pure dephasing negligible at low temperatures. Therefore, dissipative transitions are only induced close to the crossing, and we obtain the corresponding Bloch equations by cyclic permutation of the dissipative terms in Eq. (4.61) which yields

$$\dot{\vec{s}} = \begin{pmatrix} -\Gamma & -\delta_n & 0 \\ \delta_n & -\Gamma/2 & \Delta_n \\ 0 & -\Delta_n & -\Gamma/2 \end{pmatrix} \vec{s} - \begin{pmatrix} \Gamma \\ 0 \\ 0 \end{pmatrix}. \tag{4.66}$$

Its stationary solution provides the non-equilibrium population

$$P_n^{(z)} = \frac{1}{2} + \frac{(\epsilon_0 - n\Omega)\Delta_n}{(\epsilon_0 - n\Omega)^2 + 2\Delta_n^2 + \Gamma^2/2}. \tag{4.67}$$

Since now the qubit decay occurs only during the short stages when the levels cross, the phenomenological rate $\Gamma$ is expected to be considerably smaller than for $\sigma_x$ coupling.

In Fig. 4.6(b), we compare the numerically computed interference pattern obtained with $\sigma_z$ coupling with the analytical solution (4.67) for $n = 2, 3$. Again, close to a resonance the analytics and the numerical solution agree rather well. Far from resonance, however, expression (4.67) decays only slowly and, the global picture is beyond the simple summation of all $P_n^{(z)}$. Exactly on the $n$th resonance, i.e., for $\epsilon_0 = n\Omega$, the second term of Eq. (4.67) vanishes and, hence, the excitation probability becomes $P_{\rm ex}^{(z)} = 1/2$, for all $n$.

#### 4.3.2.4 Coupling via $\sigma_y$

A bath coupling via the Pauli matrix $\sigma_y$ can induce dissipative transitions between the eigenstates of $\sigma_x$ and those of $\sigma_z$. Therefore, the corresponding Bloch equation is a combination of Eqs. (4.61) and (4.66). However, we focus in this work on parameter regimes in which the avoided crossings are well separated, i.e., in which the tunnel coupling $\Delta$ is small such that for most of the time the qubit Hamiltonian is dominated

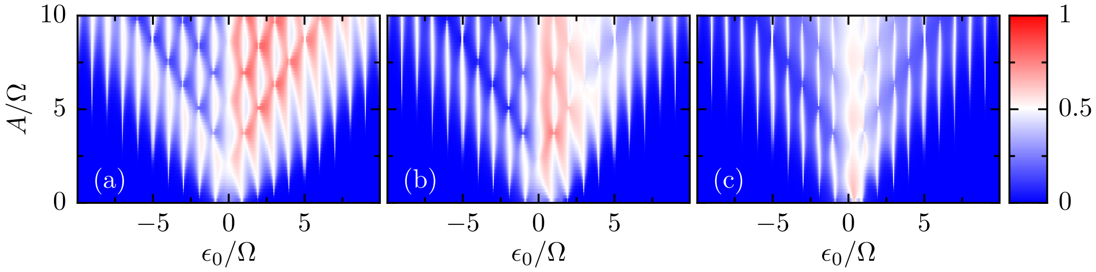

FIGURE 4.7: Steady state LZSM pattern with general bath coupling defined as in Eq. (4.68) for the mixing angles (a) $\theta/\pi = 0.03$, (b) $\theta/\pi = 0.1$ and (c) $\theta/\pi = 0.3$. All other parameters as in Fig. 4.5 (a),(d).

by the detuning $\propto \sigma_z$. Thus, dissipation will be mainly of the form (4.61). Consequently, a bath coupling via $\sigma_y$ should yield by and large the non-equilibrium population given in Eq. (4.62), i.e., $P_n^{(y)} \approx P_n^{(x)}$.

In order to confirm this conjecture, we have computed the stationary state for the parameters used in Fig. 4.5 and found that the result is practically indistinguishable from Figs. 4.5(a) and 4.6(a) (not shown). Accordingly, we find that the normalized overlap with the pattern for $\sigma_x$ coupling assumes the value $r = 0.996$.

### 4.3.3 General bath coupling

As a generalization we also considered the coupling via the operator

$$X = \sigma_x \cos\theta + \sigma_z \sin\theta. \tag{4.68}$$

The mixing angle $\theta$ varies from 0 to $\pi/2$, where the limits $\theta = 0$ and $\theta = \pi/2$ correspond to the transverse and the longitudinal case. This model captures, e.g., a superconducting charge qubit that interacts capacitively as well as inductively with the environmental circuitry. In Fig. 4.7 we plot the resulting interference pattern for different angles $\theta$. Increasing $\theta$ leads to a transition from a pattern as in Fig. 4.5(a) to a pattern as in Fig. 4.5(d). One observes, that for $\epsilon_0 < 0$ this transition proceeds faster as for $\epsilon_0 > 0$ leading to an asymmetry in the pattern. This can be understood by noticing that the bath coupling operator (4.68) is in general not invariant (unless $\theta$ is a multiple of $\pi$) under $\epsilon_0 \to -\epsilon_0$, i.e., a transformation $U = \exp(-i\pi\sigma_x)$ corresponding to a rotation of $\pi$ around the $x$ axis.

It is also intriguing to see which dissipative influence dominates the LZSM interference. For this purpose, we define the normalized overlap between the pattern for $\sigma_x$ coupling and the pattern for the coupling operator in Eq. (4.68) as

$$r_x(\theta) = \frac{(P_{\text{ex}}^x | P_{\text{ex}}^X)}{\sqrt{(P_{\text{ex}}^x | P_{\text{ex}}^x)(P_{\text{ex}}^X | P_{\text{ex}}^X)}}, \tag{4.69}$$

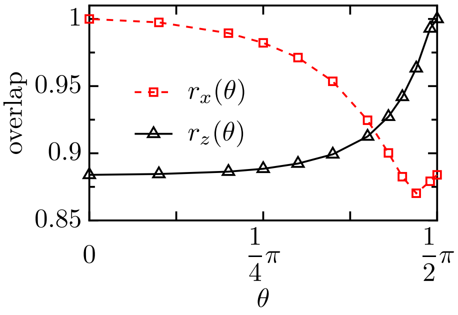

FIGURE 4.8: Overlap of the interference pattern for the mixed coupling (4.68) with the patterns for the coupling operators $\sigma_x$ (squares) and $\sigma_z$ (triangles) as a function of the mixing angle. All other parameters are as in Fig. 4.5 (a),(d).

where $(P, Q) = \int d\epsilon\, dA\, P(\epsilon, A)Q(\epsilon, A)$ denotes the inner product between two real functions in $\epsilon$-$A$ space. For $\sigma_z$ coupling we define $r_z(\theta)$ accordingly. Obviously, their limits are $r_x(0) = 1 = r_z(\pi/2)$.

The result shown in Fig. 4.8 reveals that upon increasing $\theta$ from $\theta = 0$, i.e., augmenting the influence of $\sigma_z$, the pattern remains close to the one of Fig. 4.5(a). By contrast, the pattern for $\sigma_z$ coupling is more sensitive to a small admixture of $\sigma_x$. Thus, unless the bath coupling via $\sigma_z$ is much larger, we find the “usual” interference pattern of Fig. 4.5(a). This is consistent with the fact that in most experiments, one indeed finds such a LZSM pattern with Lorentzians [25, 27, 28, 33]. Notice ,however, that this reasoning does not necessarily apply to LZSM patterns for the average current through open double quantum dots [30,34], because there the dominating incoherent dynamics is the electron tunneling between the quantum dots and the leads. Moreover, the Hilbert space for a transport setup is larger since it must comprise states with different electron number.

## 4.4 Patterns in Fourier space

Fourier theory is a reliable tool for analysing and processing data, signals and images, and applying the Fourier transform to a certain set of data often reveals important information and hidden structures. Therefore, it seems natural to consider the Fourier transform of LZSM patterns

$$W(\tau_\epsilon, \tau_A) := \int \frac{d\epsilon_0}{2\pi}\frac{dA}{2\pi}\, e^{-i\epsilon_0\tau_\epsilon} e^{-iA\tau_A} P_{\text{ex}}(\epsilon_0, A). \tag{4.70}$$

Indeed, this Fourier transform of LZSM patterns has been studied experimentally [29] as well as theoretically [33]. There, one observed characteristic “lemon shaped” arcs which can be connected with the dynamical phase of the qubit [33]. In Fig. 4.9, we plot the $W(\tau_\epsilon, \tau_A)$ obtained by a numerical Fast Fourier transform (FFT) algorithm [157] to $P_{\text{ex}}^{(x)}$ obtained from the analytical formula (4.81). The resulting structure is generic for LZSM patterns and can also be observed for patterns with longitudinal bath coupling $X = \sigma_z$. As we will discuss later, the arcs decay exponentially in Fourier space, with a decay rate that can be connected with the decoherence rate of the qubit [33, 34]. This

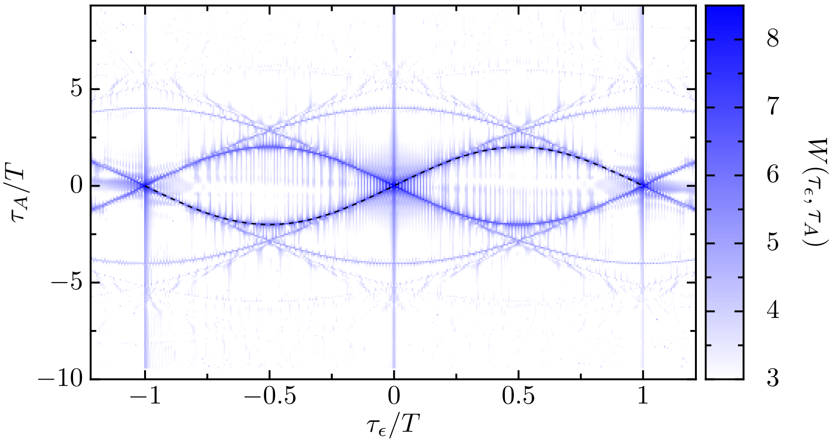

FIGURE 4.9: Fourier transform of a LZSM pattern defined in Eq. (4.70). $P_{\mathrm{ex}}$ was calculation using the analytical solution (4.63) with parameter $\Delta = 0.5\Omega$, $\Gamma = 0.001\Omega$. The black dashed line shows the analytical prediction (4.81) for structure in Fourier space.

opens the possibility to use LZSM interference as a tool to measure decoherence. For this purpose, it desirable to know the analytical form of the arcs. This will be provided in the following.

### 4.4.1 Stationary phase calculation

As a first attempt which will prove useful for symmetric drivings $f(t) = f(-t)$, we follow the arguments of [33]. Assuming that the coupling $\Delta$ is small. the dynamical phase between two LZ-transition (4.6) of the system is

$$\phi^{\mathrm{d}}_{1,2}(\epsilon_0, A) = \epsilon_0(t_2 - t_1) + A[F(t_2) - F(t_1)], \tag{4.71}$$

where we explicitly stressed the $\epsilon_0$ and $A$ dependence of the phase, and introduced

$$F(t) = \int_0^t f(t')dt'. \tag{4.72}$$

In a semi-classical description, the LZSM- interference contrast is a periodic function of the dynamical phase, i.e.,

$$P_{\mathrm{ex}}(\epsilon_0, A) = e^{i\phi^{\mathrm{d}}_{1,2}(\epsilon_0,A)} P_0, \tag{4.73}$$

with $P_0$ being a constant. In Fourier space this leads to

$$W(\tau_\epsilon, \tau_A) = \int \frac{d\epsilon_0}{2\pi} \frac{dA}{2\pi}\, e^{-i\epsilon_0\tau_\epsilon} e^{-iA\tau_A} e^{i\phi^{\mathrm{d}}_{1,2}(\epsilon_0,A)} P_0 \tag{4.74}$$

$$= \int \frac{d\epsilon_0}{2\pi} \frac{dA}{2\pi}\, e^{i\tilde{\phi}(\epsilon_0,A)} P_0, \tag{4.75}$$

with the phase

$$\tilde{\phi}(\epsilon_0, A) = \epsilon_0[(t_2 - t_1) - \tau_\epsilon] + A[(F(t_2) - F(t_1)) - \tau_A]. \tag{4.76}$$

The integrals in Eq. (4.74) contain rapidly oscillating terms in $\epsilon_0$ and $A$ which will average out and do not contribute to $W(\tau_\epsilon, \tau_A)$. The main contribution will come from terms where the phase $\tilde{\phi}(\epsilon_0, A)$ vanishes. This leads to the stationary-phase conditions

$$\frac{\partial \tilde{\phi}(\epsilon_0, A)}{\partial \epsilon_0} \overset{!}{=} 0, \qquad \frac{\partial \tilde{\phi}(\epsilon_0, A)}{\partial A} \overset{!}{=} 0, \tag{4.77}$$

from which directly follow the conditions

$$\tau_\epsilon = (t_2 - t_1), \qquad \tau_A = F(t_2) - F(t_1). \tag{4.78}$$

Using that here $f(t) = \cos(\Omega t)$, or $F(t) = (1/\Omega)\sin(\Omega t)$, respectively, one can employ the identity

$$\sin(\theta_1) - \sin(\theta_2) = 2\sin\Big(\frac{\theta_2 - \theta_1}{2}\Big)\cos\Big(\frac{\theta_2 + \theta_2}{2}\Big) \tag{4.79}$$

to find

$$\tau_A = 2\sin\Big(\frac{\Omega\tau_\epsilon}{2}\Big)\cos\Big(\frac{\Omega(t_2 + t_1)}{2}\Big). \tag{4.80}$$

Since $t_2$ and $t_1$ are solution of $\epsilon_0 = Af(t)$ while $f(t)$ is a symmetric function with one maximum and one minimum per period, it follows that $t_2 = -t_1 + T$ and we obtain

$$\tau_A = \pm 2F\Big(\frac{\tau_\epsilon}{2}\Big). \tag{4.81}$$

Note that a similar calculation can performed also for a phase shifted driving with $f(t) = \cos(\Omega t + \varphi_0)$, or even a general periodic driving as long as two condition are met:

1. The driving possesses only one maximum and one minimum per period,
2. The driving is symmetric (up to a phase shift $\varphi_0$): $f(t + \varphi_0) = f(-t + \varphi_0)$.

Alternatively, to the derivation presented in the this subsection, Eq. (4.81) can be derived from the analytical solution (4.63). This approach can be generalized beyond symmetric driving and gives a description of the Fourier transformed pattern for any periodic driving, as we will discuss later. Plotting the solution Eq. (4.81) together with the result obtain by a numerical FFT algorithm in Fig. 4.9 shows that at least the “fundamental” arcs are described accurately. Additionally, one observes “higher order” arcs obeying the phenomenological equation [34]

$$\tau_A = \pm\frac{2k}{\Omega}\sin\Big(\frac{\Omega\tau_\epsilon + 2\pi k'}{2k}\Big), \tag{4.82}$$

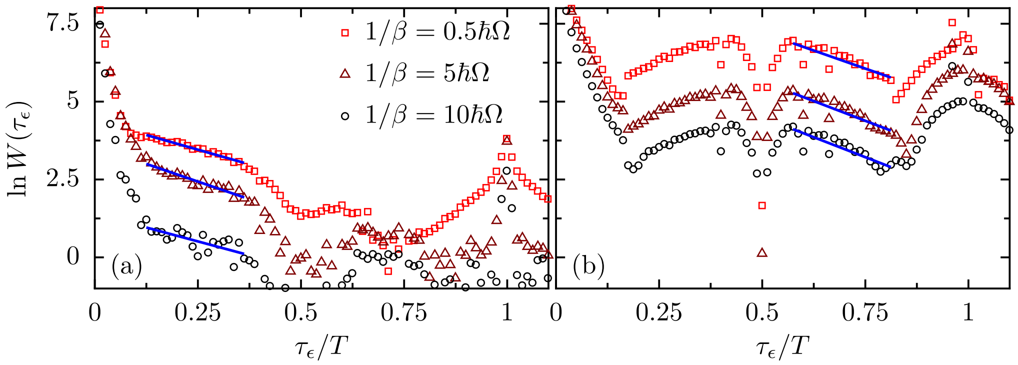

FIGURE 4.10: Fourier transform of the interference pattern, $W(\tau_\epsilon, \tau_A)$ along the principal arc $\tau_A = 2F(\tau_\epsilon/2)$ for (a) $X = \sigma_x$ and (b) $X = \sigma_y$. Parameter $\Delta = 0.5$ and $\alpha = 0.05$. The symbols show numerical results for different temperatures $1/\beta$, while the straight lines are fits to an exponential decay.

with $k = 1, 2, 3, \ldots$, $k' = 0, 1, 2, 3, \ldots$, and $k' < k$. Their emergence will be explained below.

### 4.4.2 Decay of the arc structures

Commonly, resonances, like the LZSM resonances, are of Lorentzian shape, which usually is a direct consequence of an exponential decay process. Hence, it is not surprising also that the LZSM pattern with transverse bath coupling exhibits peaks which are Lorentzian in $\epsilon_0$ direction. The Fourier transform of the LZSM pattern can be considered as transformation from the energy domain back to the time domain, and may reproduce the exponential decay. Indeed, theoretical investigations using a simple dephasing model [33] suggest that the arcs in Fourier space (cf. Fig. 4.9), obeying the analytical form Eq. (4.81), decay exponentially with an decay rate $\Gamma_2 = 1/T_2$ corresponding to the decoherence rate,[4] of the qubit. Hence, LZSM interferometry is a promising tool to measure decoherence. Admittedly, the decay in Fourier space in general will also depend on other, possibly uncontrollable quantities, however, ofter it might be still possible to determine ,e.g., dimensionless dissipation strength $\alpha$, by comparing the decay of the arc structure of measured LZSM patterns with theoretical data [34].

The underlying analysis requires that the decay is noticeably influenced by $\alpha$ and by the temperature. Therefore, we like to explore numerically, whether such a dependence can be found also for the present spin-boson model. In Sec. 4.3.1, we observed that the steady state interference patterns with different bath coupling respond quite differently to a change in dissipation strength and temperature. Hence, it might be interesting to see how the corresponding Fourier transformed patterns decay. Figure 4.10 shows this decay along one arc (black dashed line in Fig. 4.9) for transverse (panel (a)) and

---

[4] The decoherence rate can be defined as the rate with which the off-diagonal elements of the density matrix decay. Accordingly, also the entanglement [e.g. quantified by the concurrence Eq. (3.3)] between the system and e.g. an other qubit will decay with this rate, see e.g. Ref. [4] Chapter 3.

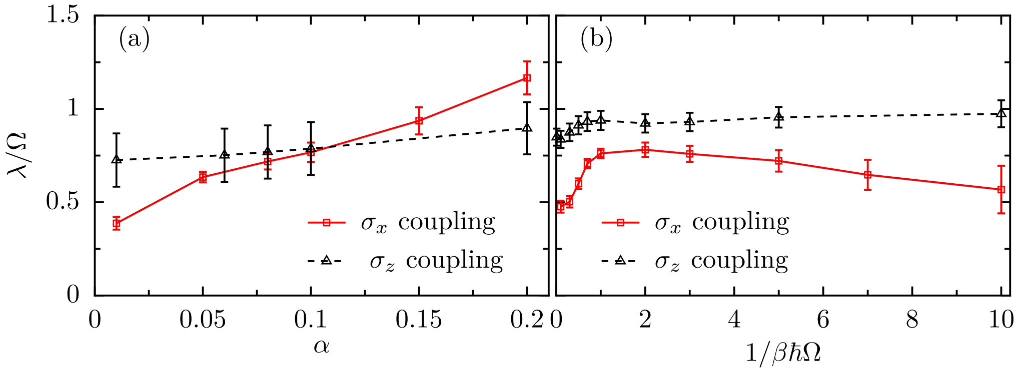

FIGURE 4.11: Analysis of the principal arc for $\Delta = 0.5\Omega$. (a) Decay rate $\lambda$ for temperature $1/\beta = 0.5\hbar\Omega$ as a function of the dissipation strength $\alpha$. The error bars are determined by slightly varying the fit range. (b) Decay rate as a function of the temperature for dissipation strengths

longitudinal (panel (b)) bath coupling. In panel (a) it can be appreciated that in the vicinity of $\tau_\epsilon \approx T/4$, the Fourier amplitude decays exponentially, $W(\tau_\epsilon) \propto \exp(-\lambda\tau_\epsilon)$. This implies that there the decay can be characterized by only one parameter, namely the rate $\lambda$ which we will determine within a numerical fit procedure.

For longitudinal bath coupling (panel (b)) the behavior is quite different, but nevertheless one can locate regions where the decay is exponential (between $T/2$ and $3T/2$), so that we can determine a decay constant $\lambda$. The central question is then whether $\lambda$ exhibits a clear $\alpha$ dependence, in particular in the regime of low temperatures $T \lesssim \hbar\Omega/k_B$ and small tunneling $\Delta \lesssim \hbar\Omega$, in which most LZSM patterns have been measured. Figures 3.4(a) and 3.4(b) show the decay rate as a function of the dissipation strength and the temperature, respectively. For longitudinal bath coupling, the rate exhibits a rather weak parameter dependence. A possible reason for this is that dissipative decays happen mainly during the short stages when the levels cross. Therefore, the effective decoherence rate is always much smaller than the “natural” width of the asymmetric peaks given by $\Delta_n$, cf. Fig. 4.6(a) and Eq. (4.67). At first sight, this weak parameter dependence seems not in accordance with the LZSM patterns for open quantum dots with a bath coupling via $\sigma_z$ [34]. Notice, however, that the open double quantum dot used there is beyond the present model. First, the description of electron transport requires one to take more states and different electron numbers into account, especially when also spin effects play a role. Second, there the dot-lead coupling is responsible for the main dissipative effects, while the bath coupling represents a perturbation and does not influence the qualitative behavior.

For the transverse bath coupling via $\sigma_x$, by contrast, $\lambda$ grows significantly and monotonically with the dissipation strength $\alpha$, a feature that is essential for the fixing of $\alpha$ from measured data. The behavior as a function of the temperature is more involved and even non-monotonic. For very low temperatures, the decay rate starts with a value

$\lambda \approx 0.4\Omega$, followed by a steep increase until the thermal energy matches the photon energy, $k_B T \approx \hbar\Omega$. Then a slow decay sets in which lasts until eventually the range of exponential decay becomes so small that the fitting procedure is no longer reasonable.

## 4.5 LZSM patterns with general driving

The aim of this section is to investigate LZSM interference for general periodic driving, i.e. we consider the Hamiltonian (4.1) with

$$f(t) = f(t+T). \tag{4.83}$$

In our numerical examples, we consider besides the specific examples

$$f_1(t) = \cos(\Omega t) + 0.1\cos(3\Omega t), \tag{4.84a}$$

$$f_2(t) = \cos(\Omega t) + \cos(2\Omega t), \tag{4.84b}$$

$$f_3(t) = \sin(\Omega t) + \sin(2\Omega t), \tag{4.84c}$$

where $f_1$ and $f_2$ are symmetric functions, i.e., they obey $f(t_0+t) = f(t_0-t)$ for $t_0 = 0$ and for $t_0 = T/2$. By contrast, $f_3(t_0+t) = -f_3(t_0-t)$ is anti-symmetric. While $f_1$ modifies the pure cosine driving only slightly, the other two shapes are qualitatively different because they possess several maxima and minima per driving period. As we discuss below in Sec. 4.4 this has consequences for the structures observed in Fourier space, see Fig. 4.12(g)–(i).

To give a first impression of our results, we depict in Figs. 4.12(d)–(f) the LZSM interference patterns for the driving shapes in Eq. (4.84) and transverse qubit-bath coupling. All three patterns exhibit resonance peaks whenever the detuning $\epsilon_0$ matches with a multiple of the driving frequency. As discussed above, significant non-equilibrium population requires that the amplitude is large enough to reach the avoided level crossing, which is the case for $\min[f(t)] < \epsilon_0/A < \max[f(t)]$. The peaks depend strongly on the amplitude and may even vanish. Comparing panels (d)–(f), we can conclude that the patterns look qualitatively the same, despite the rather different driving shapes which are visible in the adiabatic energies of the qubit Hamiltonian (4.1) depicted in panels (a)–(c). The main differences stem from the fact that the harmonics with frequency $2\Omega$ may change the maximum and the minimum value of $f(t)$ and, thus, affect the above condition for significant excitations. For the driving shape $f_2$, this condition depends on the sign of $\epsilon_0$, which explains the asymmetry of the pattern in panel (e), which was also observed in [158].

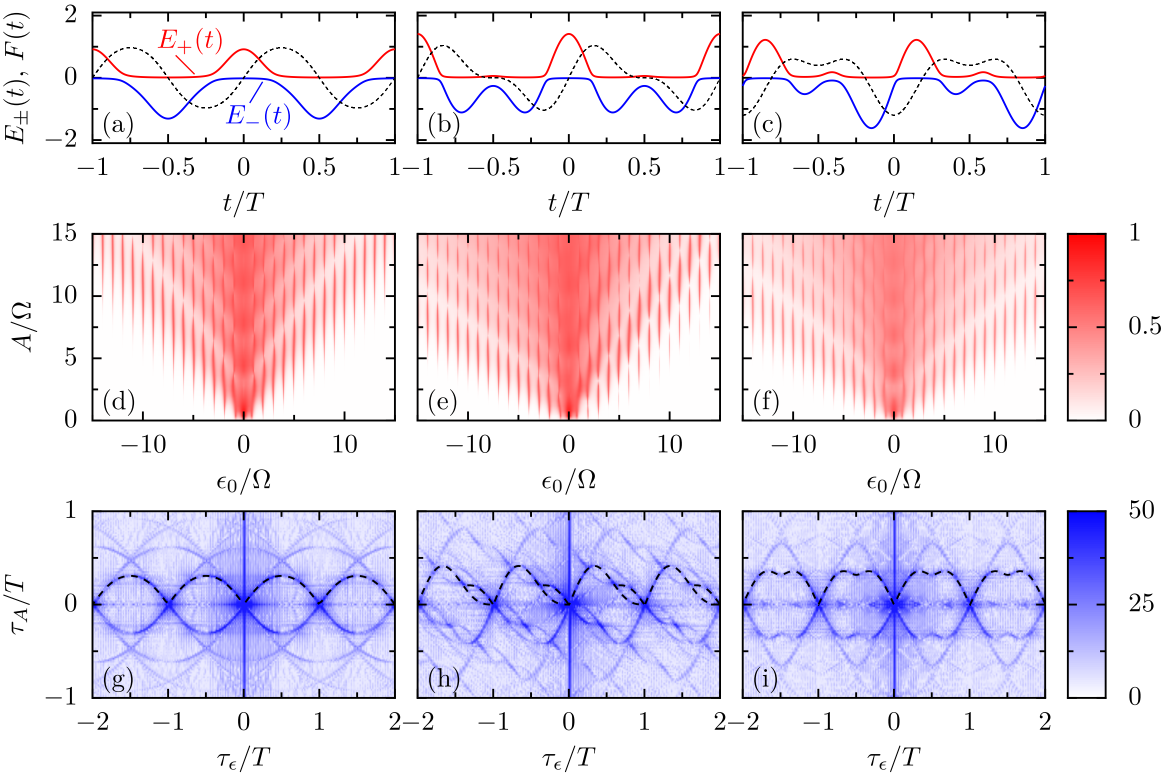

FIGURE 4.12: [(a)–(c)] Adiabatic energies $E_\pm(t)$ (red and blue solid lines) of the Hamiltonian (**??**) in units of $\hbar\Omega$ for vanishing static detuning, $\epsilon_0 = 0$, and the driving shapes $f_1(t)$–$f_3(t)$ in Eq. (4.84). The dashed black line marks the integral of the driving, $F(t)$, in units of $1/\Omega$. [(d)–(f)] Resulting non-equilibrium populations in $\epsilon_0$-$A$ space. [(g)–(i)] 2D Fourier transform $W(\tau_\epsilon, \tau_A)$ of the interference patterns, defined in Eq. (4.70). The dashed lines in the upper half plane mark the analytic expressions for the arc structure derived in Sec. 4.4. The patterns are computed with the stationary solution of the Bloch-Redfield master equation for the tunnel matrix element $\Delta = 0.5\Omega$, dissipation strength $\alpha = 10^{-3}$, temperature $k_BT = 1/\beta = 0.1\hbar\Omega$, and transverse qubit-bath coupling, i.e., $X = \sigma_x$ in Eq. (**??**).

### 4.5.1 Interference pattern in Fourier space

The interference patterns in real space depend only weakly on the shape of the driving, while qubit-bath coupling has a strong influence. The 2D Fourier transform of these pattern (Figs. 4.12(g)–(i)) provide a complementary picture in which the shape of the driving dominates. For the symmetric driving functions $f_1$ and $f_2$, we find a pronounced arc structure at $\tau_A = 2F(\tau_\epsilon/2)$ and $\tau_A = 2F(\tau_\epsilon/2 + T/2)$, cf. the dashed black lines in panels (a) and (b). They can be explained within the stationary-phase treatment of the LZSM interference in Sec. 4.4.1 and have been measured in [29]. However, there emerge several features that are beyond. Most significantly, in panel (i) we find that for the anti-symmetric driving with $f_3$, the structure is different from the corresponding $F(\tau_\epsilon/2)$ depicted by the dashed line in panel (c). Moreover, the driving $f_2$ yields additional arcs close to the origin. As discussed before, there also emerge higher-order replica of the arcs which have been found both experimentally [33,34] and theoretically [34].

For an analytical approach to the arc structure, we assume a system bath coupling via $X = \sigma_x$ and. follow the lines of Sec. 4.3.2.1. We first transform the system Hamiltonian by means of $U_\mathrm{r}(t) = \exp\{-i\phi(t)\sigma_z/2\}$ with the time-dependent phase $\phi(t) = n\Omega t + AF(t)$, where

$$F(t) = \int_0^t dt'\, f(t'). \tag{4.85}$$

This constitutes a straightforward generalization of the above treatment. In order to derive an effective Hamiltonian of the form (4.16) we introduce the renormalized coupling

$$\Delta_n(A) = \frac{\Delta}{T}\int_0^T dt\, e^{in\Omega t - iAF(t)}. \tag{4.86}$$

The latter obviously is the $n$th Fourier coefficient of $\Delta \exp\{-iAF(t)\}$, a property that will prove useful. This generalizes the result for purely harmonic driving, $\Delta_n = \Delta J_n(A/\Omega)$ with the $n$th order Bessel function of the first kind, to arbitrary but periodic shapes $f(t)$. With this we are able to derive the generalization of the non-equilibrium population Eq. (4.63) and obtain

$$P_{\mathrm{ex}}^{(x)} = \frac{1}{2}\sum_n \frac{\Delta_n^2/2}{(\epsilon_0 - n\Omega)^2 + \Delta_n^2/2 + \Gamma^2/4}. \tag{4.87}$$

Except for the re-defined $\Delta_n$, all quantities are as above. To derive an expression for the structures in Fourier space, we apply the Fourier transform (4.70), where $\epsilon_0$-integral can be evaluated readily to yield

$$W(\tau_\epsilon, \tau_A) = \frac{1}{4\pi}\int dA\, e^{-iA\tau_A}\sum_n \frac{\Delta_n^2}{\Gamma_n^*} e^{-in\Omega\tau_\epsilon} e^{-\Gamma_n^*|\tau_\epsilon|}, \tag{4.88}$$

with the resonance width $\Gamma_n^* = (\Delta_n^2/2 + \Gamma^2/4)^{1/2}$.

#### 4.5.1.1 Overdamped limit

The remaining $A$-integral in (4.88) can be evaluated directly in the over-damped limit $\Gamma \gg \Delta$ in which $\Gamma_n^* \approx \Gamma/2$ and, thus,

$$W(\tau_\epsilon, \tau_A) = \frac{1}{2\pi\Gamma}\int dA e^{-iA\tau_A}\sum_n \Delta_n^2 e^{-in\Omega\tau_\epsilon}. \tag{4.89}$$

Focusing on the range of small $\tau_\epsilon$, we have neglected the last exponential in Eq. (4.88). To proceed, we evaluate the sum

$$\sum_n \Delta_n \cdot \Delta_n e^{-in\Omega\tau_\epsilon}, \tag{4.90}$$

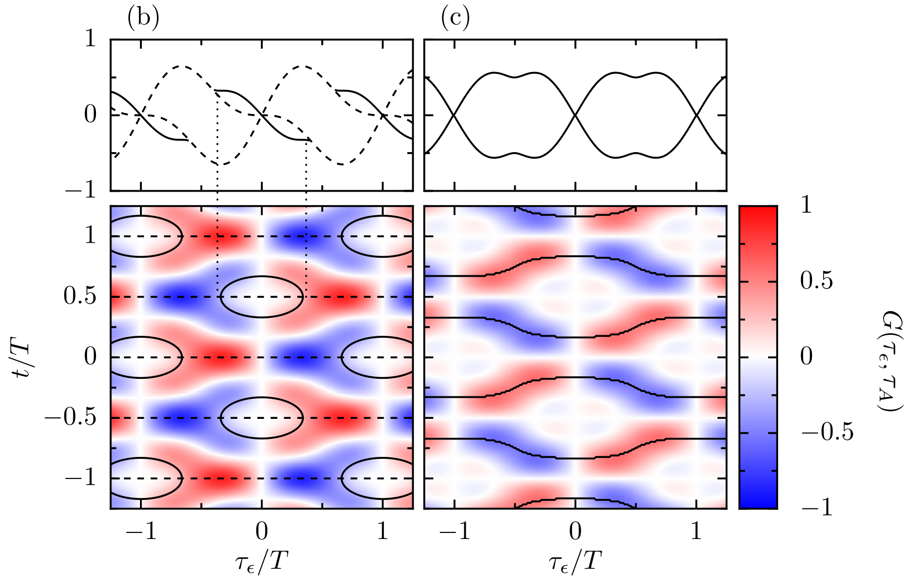

FIGURE 4.13: Determination of the "non-generic" arcs for the driving shapes $f_2$ (a) and $f_3$ (b). The color code in the lower panels depicts $G(t, \tau_\epsilon)$, while the horizontal dashed lines mark the generic solutions of Eq. (4.96) at multiples of $T/2$. The solid lines represent numerical solutions of Eq. (4.96). Significant contributions to $W(\tau_\epsilon, \tau_A)$ are determined by the solutions of the transcendental equations (4.96) and (4.97), i.e. the cuts of $G(t, \tau_\epsilon)$ along the solid and dashed lines. Projecting these solutions on the $\tau_\epsilon$ axis (hinted by vertical dotted lines) results in the arc structures plotted in the upper panels and in Figs. 4.12(h) and 4.12(i).

where the two factors are easily identified as the $n$th Fourier coefficients of $\exp\{-iAF(t)\}$ and $\exp\{-iAF(t+\tau_\epsilon)\}$, respectively, cf. the definition of $\Delta_n$ in Eq. (4.86). Thus, expression (4.90) represents the inner product of these exponentials. According to Parseval's theorem ( [159] p. 156), it can be written in the time domain to read

$$\frac{1}{T}\int_0^T dt\, e^{iAF(t)} e^{-iAF(t+\tau_\epsilon)}. \tag{4.91}$$

We symmetrize the integrand via the substitution $t \to t - \tau_\epsilon/2$ and perform the $A$-integration to obtain

$$W(\tau_\epsilon, \tau_A) = \frac{1}{T}\int_0^T dt\, \delta(\tau_A - G(t, \tau_\epsilon)) \tag{4.92}$$

$$= \frac{1}{T}\sum_{t_i} \frac{1}{|g(t_i, \tau_\epsilon)|}, \tag{4.93}$$

where

$$G(t, \tau_\epsilon) = F(t + \tau_\epsilon/2) - F(t - \tau_\epsilon/2), \tag{4.94}$$

$$g(t, \tau_\epsilon) = f(t + \tau_\epsilon/2) - f(t - \tau_\epsilon/2). \tag{4.95}$$

The sum in Eq. (4.93) has to be taken over all times $t_i$ that fulfill $\tau_A = G(t_i, \tau_\epsilon)$.

Expressions (4.92) and (4.93) allow us to extract the arc structure by the following reasoning. On the one hand, the argument of the delta-function in Eq. (4.92) specifies the times $t_i$ that contribute to the integral. On the other hand, the most significant contributions to $W$ stem from regions where the denominator in Eq. (4.93) vanishes. Thus, the structure is determined by the conditions

$$0 = g(t, \tau_\epsilon), \tag{4.96}$$

$$\tau_A = G(t, \tau_\epsilon), \tag{4.97}$$

which describe one-dimensional manifolds in the Fourier space $(\tau_\epsilon, \tau_A)$. They correspond to the arcs in Figs. 4.12(g)–(i). Practically, the arc structure is obtained in the following way. One determines from $g(t_i, \tau_\epsilon) = 0$ all zeros $t_i(\tau_\epsilon)$ and inserts them into Eq. (4.97) which yields relations of the type $\tau_A^{(i)}(\tau_\epsilon)$. Obviously, $\tau_A = \tau_\epsilon = t = 0$ is a trivial solution for any driving shape $f(t)$. Thus, the Fourier transformed of all LZSM patterns exhibits a peak at the origin and, owing to the periodicity of the driving, at multiples of $T$.

Two generic arcs can be found analytically if the driving obeys time-reversal symmetry, $f(t - t_s) = f(-t - t_s)$ (without loss of generality, we henceforth assume $t_s = 0$). Then Eq. (4.96) possesses the solutions $t_1 = 0$ and, owing to the $T$-periodicity of $f$, $t_2 = T/2$. They provide the arcs

$$\tau_A^{(1)} = 2F(\tau_\epsilon/2), \tag{4.98}$$

$$\tau_A^{(2)} = 2F(\tau_\epsilon/2 + T/2), \tag{4.99}$$

which are in agreement with those found within the stationary-phase treatment of Sec. 4.4.1 and [33], see Eq. (4.81).

If a symmetric driving $f$ has only one minimum and one maximum per period, such as $f_1$ or $f(t) = \cos(\Omega t)$, $t_1$ and $t_2$ are the only roots of Eq. (4.96). Then the arc structure for symmetric driving can be obtained fully analytically. This fact is of practical use if one employs LZSM interference to determine decoherence properties of a qubit via the arc decay [34]. In all other cases, i.e., when $f$ is not symmetric or if it possesses more than two minima/maxima per period, we have to solve Eq. (4.96) numerically to obtain also “non-generic” arcs. For the symmetric driving $f_2$, this leads to the ellipse-shaped solutions sketched in the lower panel of Fig. 4.13(a). Upon reducing the harmonic with frequency $2\Omega$, they shrink and eventually vanish. Together with the generic solution, we obtain the structure shown in the upper panel of Fig. 4.13(a). In particular, there is a region in which the arc splits into two branches. This prediction is quantitatively confirmed by the numerical solution of the full problem shown in Fig. 4.12(h).

If $f$ is not time-reversal symmetric, we generally have to determine all $t_i$ numerically. For the driving shape $f_3$, this procedure is visualized in Fig. 4.13(b), where the solid lines in the lower panel depict the zeros of $g(t, \tau_\epsilon)$ which define two independent manifolds $t_i(\tau_\epsilon)$ and those related by the time shift $t \to t + T$. The corresponding arc structure shown in the upper panel agrees with the one obtained numerically which is shown in Fig. 4.12(i).

#### 4.5.1.2 Weak dissipation and arcs of higher order

In the limit of weak dissipation, $\Gamma \ll \Delta_n$, the resonance width in Eq. (4.88) becomes $\Gamma_n^* = |\Delta_n|/\sqrt{2}$, so that we have to evaluate the Fourier transform of $\sum_n |\Delta_n(A)|$. This represents a rather difficult task and, thus, we only discuss its implications on a qualitative level.

A main effect of the cusps stemming from the absolute value is the emergence of higher harmonics, cf. the Fourier transform of expressions such as $|\cos(\Omega t)|$. Accordingly, in the Fourier transform of our interference patterns, we find arcs of higher order as can be appreciated in Figs. 4.12(g)–(i). To be specific, the arcs given by Eqs. (4.98) and (4.99) are generalized to (c.f. Eq. (4.82))

$$\tau_A = 2kF(\tau_\epsilon/2k + k'T/2k), \tag{4.100}$$

where $k = 1, 2, 3, \dots$ and $k' = 0, 1, \dots, 2k-1$. This prediction agrees with our numerical findings shown in Figs. 4.12(g) and 4.12(h). From a theoretical point of view, it is interesting to see that arcs of higher order are found already within a two-level description, i.e., within the most basic model for LZSM interference. Thus, their emergence does not require the consideration of further levels or non-linearities.

## 4.6 Summary and Outlook

We have developed a comprehensive picture of LZSM interference for a two level system in contact with a bosonic environment and thereby extended previous results to arbitrary periodic driving shapes and a general qubit-bath coupling. The central quantity of interest was the time-averaged steady state population of the excited state of the undriven qubit. For its numerical computation, we derived a Bloch-Redfield master equation decomposed into the Floquet states of the driven qubit, where we avoided any rotating-wave approximation even in its moderate form. Thus, our long-time solution contained the full information about the coherences.

The interference patterns in “real space”, i.e., as a function of the detuning and the driving amplitude, turned out to be strongly influenced by the qubit operator that couples to the environmental degrees of freedom. By contrast, the shape of the driving is of minor relevance. In particular, we found that for a bath coupling that is transverse with respect to the driving, the resonances are Lorentzians, while they possess an anti-symmetric structure in the longitudinal case. By a mapping the time-dependent problem to an effective static Hamiltonian, we have obtained Bloch equations which yield expressions for the LZSM patterns in agreement with the numerical results. As a further feature, the LZSM pattern exhibits a triangular background which can be explained within an adiabatic approximation for the full time-dependent Bloch equations. Moreover, in the presence of both a transverse and a longitudinal bath coupling, the influence of the transverse coupling prevails.

The Fourier transform of the LZSM patterns provide a complementary picture. This representation of the interference pattern is dominated by the shape of the driving manifest in the arc structure. The solution of our effective Bloch equations allowed us to generalize knowledge about these arcs. For a driving with time-reversal symmetry, they are given by the integral of the driving. In addition, they may develop side branches which can be explained within our analytical approach, but their determination requires the moderate effort of numerically solving a transcendental equation. The same numerical procedure also serves for the case of asymmetric driving.

A promising application of LZSM interferometry is the fixing of dissipative parameters by comparing the arc decay for experimental and theoretical data. Analysing the arc decay for different bath couplings, we found that for transverse bath coupling, the decay rate increases significantly with dissipation strength and temperature, unless the thermal energy exceeds the energy quantum of the driving. Thus, in particular for predominantly transverse coupling and low temperatures, LZSM interference represents a useful tool for analyzing decoherence properties. For purely longitudinal bath coupling, by contrast, the arc decay depends only weakly on dissipation.

Our investigation reveals that already the LZSM pattern of a qubit is quite intriguing. It may become even more involved for Landau-Zener scenarios with three or more levels [160,161] which are relevant when spin effects enter [162] or for a qubit that couples to additional degrees of freedom such as, e.g., an exciton in a photonic crystal with a coupling modulated by a surface-acoustic wave (compare Chap. 3). LZSM interferometry for such setups represents an emerging field of investigation.

# Chapter 5

# Conclusion

Driven quantum systems bear a variety of intriguing phenomena, while at the same time, a time-dependent interaction with a quantum system is often mandatory, if one whats to control its dynamics. Because solid-state quantum systems give the opportunity to tune parameters within a range inaccessible with, e.g. atomic systems, they offer an auspicious playground for investigating the physics of driven quantum systems and testing novel control schemes. Since the interaction with their environment is in general not negligible, one has to consider them as open system. On the one hand, this induces dissipation and noise in the system, leading to decoherence. One the other hand, the interplay between driving and dissipation can engender new effects, worth to investigate. This motivated us to adress three specific problems:

In the first part (Chapter 2), we propose to study quantum work fluctuations of a parametrically driven oscillator using superconducting circuits. Therefore, we employ a novel method based on Ramsey interferometry which uses an ancilla qubit to read out the characteristic function of work. In order to apply this method to a standard circuit QED setup, a line resonator coupled to a Cooper pair box, we extend it to a two qubit scheme and derive an effective Hamiltonian for the situation where the resonator frequency is much smaller than the splitting of the qubit. We present results for a closed system, where we numerically simulate the experimental test of the quantum Crooks fluctuation theorem, and argue that the presented scheme allows to test fluctuation relations even for open systems with arbitrary strong interaction with an environment. The presented scheme is not fixed to a specific setup and can be transferred to other more involved experimental arrangements.

The second part of this thesis (Chapter 3), focuses on the generation of entanglement between a self-assembled quantum dot and a photonic crystal nanocavity using surface acoustic waves (SAW). Here, we show for realistic experimental parameters that it is possible to implement entangling gates based on Landau-Zener transitions by modulating the cavity frequency with a SAW. In order to include the main sources of decoherence, we derive a master equation describing photon loss, and incoherent decay of a quantum dot exciton. A systematic analysis of the parameter space reveals the optimal driving parameters and shows that the maximal entanglement, as well as its lifetime, can be improved by employing Fourier synthesised SAW pulses. Our calculations show that the fundamental limit of this scheme is the photon lifetime in the cavity.

The third part of this thesis (Chapter 4), is devoted to the periodically driven spin-boson model, where a driven two-level system is interacting with environment modeled as an infinite ensamble of harmonic oscillators. If the driving modulates the level splitting of the two-level system, its dynamics can be interpreted as a succession of Landau-Zener transition, induced whenever the level splitting vanishes. Because between the transitions the system gains a dynamical phase, the qubit interferes with itself at the transitions, producing a characteristic interference pattern, called Landau-Zener-Stückelberg-Majorana (LZSM) pattern. As we show, this patterns sensitively depends on the details of the system bath coupling. If the driving and the bath couple to the same coordinate (longitudinal system-bath coupling), the pattern changes qualitatively and bath-induced population inversion emerges. Our numerical calculations, based on a Floquet-Markov master equation, are supported by analytical results, obtained from effective time-independent Bloch equations. Considering general periodic driving protocols, we show that, while the “real space” LZSM patterns only weakly depend on the shape of the driving, their Fourier transform exhibits periodic structures which reflect the driving shape. These structures decay in Fourier space, where the decay rate may be used to determine details about the system-bath coupling. This requires that the decay rate depends on the temperature and the system-bath coupling strength. We show numerically that, while for system-bath coupling longitudinal to the driving the decay rate depends rather weakly on the bath parameters, for transversal coupling it depends linearly on the system-bath coupling. Moreover, we observe a clear temperature dependence for low temperatures. Hence, in the latter case LZSM-interferometry could be employed to quantify decoherence.

The results presented in this thesis give an impression of the richness of the field of driven open quantum systems, reaching from state “engineering” to fundamental problems in quantum thermodynamics. However, we only investigated small parts of this field. It is expected that the technical progress, especially in the field of engineered quantum systems, will bring about new experiments and intriguing effects that pose further theoretical challenges. Here, profound knowledge about the interplay between the time-dependent modulation of a quantum system and its interaction with the environment will be inalienable, in order to effectively control these systems and evade unwanted effects coming from the environmental fluctuations.

# Appendix A

# Derivation of the soft mode Hamiltonian $H'_{S+A}$

In this appendix, we derive the soft mode Hamiltonian (2.44) following *mutatis mutandis*, the derivation of the dispersive Hamiltonian presented by Schleich [163]. Our starting point is the Rabi Hamiltonian, Eq. (2.39). For simplicity we do not include the time dependence of $\varepsilon$. In the interaction picture the qubit-oscillator coupling reads [163]:

$$\tilde{H}_{\mathrm{Rabi}}(t) = \hbar g(\sigma_+ a^\dagger e^{i\Delta t} + \sigma_- a^\dagger e^{-i\Delta t} + \sigma_- a e^{-i\Gamma t} + \sigma_+ a e^{i\Gamma t}), \tag{A.1}$$

where $\Delta = \varepsilon - \omega$, $\Gamma = \varepsilon + \omega$ and $\sigma_-, \sigma_+$ are the qubit rising and lowering operators. In the interaction picture, $\tilde{H}_{\mathrm{Rabi}}(t)$ is the generator of the dynamics

$$\begin{aligned} U_{t,0} &= \mathcal{T} \exp\left(-\frac{i}{\hbar}\int_0^t dt' \tilde{H}_{\mathrm{Rabi}}(t')\right) \\ &\simeq 1 - \frac{i}{\hbar}\int_0^t dt' \tilde{H}_{\mathrm{Rabi}}(t') - \frac{1}{\hbar^2}\int_0^t dt' \tilde{H}_{\mathrm{Rabi}}(t') \int_0^{t'} dt'' \tilde{H}_{\mathrm{Rabi}}(t''). \end{aligned} \tag{A.2}$$

Plugging Eq. (A.1) into (A.2), the first order term reads

$$\begin{aligned} \int_0^t dt' \tilde{H}_{\mathrm{Rabi}}(t') = \hbar g \Big( & \sigma_+ a \frac{e^{i\Delta t} - 1}{i\Delta} + \sigma_- a^\dagger \frac{e^{-i\Delta t} - 1}{-i\Delta} \\ & + \sigma_- a \frac{e^{-i\Gamma t} - 1}{-i\Gamma} + \sigma_+ a^\dagger \frac{e^{i\Gamma t} - 1}{i\Gamma} \Big). \end{aligned} \tag{A.3}$$

This can be used the to calculate the second order term

$$\begin{aligned}\int_0^t dt'\tilde{H}_{\text{Rabi}}(t')\int_0^{t'} dt''\tilde{H}_{\text{Rabi}}(t'') \\ = \hbar^2 g^2 \int_0^t dt' \Bigg( & \sigma_+\sigma_- aa^\dagger \frac{1-e^{i\Delta t'}}{-i\Delta} + \sigma_+\sigma_- a^2 \frac{e^{i(\Delta-\Gamma)t'} - e^{-i\Delta t'}}{-i\Gamma} \\ & +\sigma_-\sigma_+ a^\dagger a \frac{1-e^{-i\Delta t'}}{i\Delta} + \sigma_-\sigma_+ a^{\dagger 2} \frac{e^{-i(\Delta-\Gamma)t'} - e^{-i\Delta t'}}{i\Gamma} \\ & +\sigma_-\sigma_+ a^2 \frac{e^{i(\Delta-\Gamma)t'} - e^{-i\Gamma t'}}{i\Delta} + \sigma_-\sigma_+ aa^\dagger \frac{1-e^{-i\Gamma t'}}{i\Gamma} \\ & +\sigma_+\sigma_- a^{\dagger 2} \frac{e^{-i(\Delta-\Gamma)t'} - e^{i\Gamma t'}}{-i\Delta} + \sigma_+\sigma_- a^\dagger a \frac{1-e^{-i\Gamma t'}}{-i\Gamma} \Bigg).\end{aligned} \tag{A.4}$$

Recalling that the oscillator is slow compared to the qubit, for times short compared to the oscillator's period we can employ the approximation $e^{\pm i(\Delta-\Gamma)t'} = e^{-\pm 2i\omega t'} \simeq 1$. In performing the integration, we neglect the fast oscillating terms of frequency $\Gamma, \Delta \simeq \varepsilon$ to obtain

$$\frac{1}{\hbar^2}\int_0^t dt'\tilde{H}_{\text{Rabi}}(t')\int_0^{t'} dt''\tilde{H}_{\text{Rabi}}(t'') \simeq \frac{ig^2}{\varepsilon}(a^\dagger + a)^2\sigma_z t, \tag{A.5}$$

where we used $\sigma_+\sigma_- - \sigma_-\sigma_+ = \sigma_z$. Note that the first order term, Eq. (A.4), contains either fast oscillating contributions or non relevant constant terms. Therefore it can be neglected at once. We thus get:

$$U_{t,0} \simeq \quad 1 - \tfrac{ig^2}{\varepsilon}(a^\dagger + a)^2\sigma_z t \simeq \exp\left(-i\tfrac{g^2}{\varepsilon}(a^\dagger + a)^2\sigma_z t\right) \tag{A.6}$$

namely $\tilde{H}_{S+A}(t) \simeq \frac{\hbar g^2}{\varepsilon}(a^\dagger + a)^2\sigma_z$. Going back to the Schrödingier picture, we finally arrive at $H_{S+A} \simeq \hbar\varepsilon\sigma_z/2 + \hbar(\omega a^\dagger a + 1/2) + \hbar g^2(a^\dagger + a)^2\sigma_z/\varepsilon$.

# Appendix B

# Derivation of the Landau-Zener formula

In this appendix, we derive the famous Landau-Zener Formula used in Eqs. (3.6) and (4.5). This formula was derived in 1932 by Landau [15], Zener [16], Stückelberg [17] and Majorana [18] independently. Their aim was to study non-adiabatic energy transfer in atomic or molecular collisions, where the nuclear motion can be treated classically. This leads to the semi-classical model Hamiltonian

$$H(t) = \frac{1}{2}\begin{pmatrix} vt & \Delta \\ \Delta & -vt \end{pmatrix} \tag{B.1}$$

with the corresponding Schrödinger equation

$$i\hbar\frac{d}{dt}\begin{pmatrix} a(t) \\ b(t) \end{pmatrix} = \frac{1}{2}\begin{pmatrix} vt & \Delta \\ \Delta & -vt \end{pmatrix}\begin{pmatrix} a(t) \\ b(t) \end{pmatrix} \tag{B.2}$$

describing a two level system with linear time-dependent level splitting $vt$ and tunnel coupling $\Delta$. Since the Landau-Zener Hamiltonian (B.1) is dominated by the diagonal terms for $t \to \pm\infty$ tunneling is only expected in the crossing region, where $|vt| < \Delta$. Starting in and initial state $a(-\infty) = 1, b(-\infty) = 0$ two questions arise. First, one could ask what is the time evolution governed by Eq. (4.7), and second one could be interested in the probability $|a(\infty)|^2$ to stay in the initial state. According to the Landau-Zener formula this probability is given by

$$P_{LZ} = \exp\left(\frac{\pi\Delta^2}{2\hbar v}\right). \tag{B.3}$$

Zener derives Eq. (B.3) by mapping the differential equations for $a(t)$ and $b(t)$ on Weber's equation and solving it exactly. Finally he takes the limit $t \to \infty$. This derivation, however, is rather tedious. In their works Zener, as well as Stückelberg cite the work of Landau who derives the transition probability in the perturbative limit and with an error of $2\pi$ [16, 164]. Alternatively, Majorana solves the problem rather elegant by expressing the solution as generalized Laplace transform and applying the method of steepest decent [165]. Given its importance, the Landau-Zener Formula was re-derived several times, for example by Wittig [164], who developed a simple derivation based on contour integration, bypassing the exact solution of the Schrödinger equation (see also [166]). Here, we employ the ansatz of Kayanuma [167], who uses a formal perturbative expansion in the spirit of quantum scattering theory. The presented calculation, however, follows the arguments of Rojo [168], who uses essentially the same ansatz as Kayanuma, but a slightly different calculation. We start with a transformation to the interaction picture

$$\bar{H}(t) = U(t)H(t)U^\dagger(t) = \frac{1}{2}\begin{pmatrix} 0 & \Delta e^{-ivt^2/2\hbar} \\ \Delta e^{ivt^2/2\hbar} & 0 \end{pmatrix}, \qquad \begin{pmatrix} \bar{a}(t) \\ \bar{b}(t) \end{pmatrix} = U(t)\begin{pmatrix} a(t) \\ b(t) \end{pmatrix} \tag{B.4}$$

using the unitary transformation

$$U(t) = \exp\Big(i\frac{vt^2}{2\hbar}\sigma_z\Big). \tag{B.5}$$

The formal solution to the Landau-Zener problem is then given by

$$\begin{pmatrix} \bar{a}(\infty) \\ \bar{b}(\infty) \end{pmatrix} = U_{\infty,-\infty}\begin{pmatrix} \bar{a}(-\infty) \\ \bar{b}(-\infty) \end{pmatrix}, \tag{B.6}$$

with the time evolution operator

$$U_{t,t'} = \mathcal{T}\exp\Big(-\frac{i}{\hbar}\int_{t'}^{t} dt\ \bar{H}(t)\Big) \tag{B.7}$$

and the time-ordered exponential

$$\mathcal{T}\exp\Big(-\frac{i}{\hbar}\int_{-\infty}^{\infty} dt\ \bar{H}(t)\Big) = 1 - \frac{i}{\hbar}\int_{-\infty}^{\infty} dt\ \bar{H}(t) - \frac{1}{\hbar^2}\int_{-\infty}^{\infty} dt_1\ \bar{H}(t_1)\int_{-\infty}^{t1} dt_2\ \bar{H}(t_2) + \dots. \tag{B.8}$$

Note that even powers of $\bar{H}$ only have diagonal entries, whereas as the odd powers have off diagonal terms. Hence, in order to compute $a(\infty)$ it suffices to consider even powers in (B.8). We obtain

$$\bar{a}(\infty) = \sum_{n=0}^{\infty}\Big(-i\frac{\Delta}{2}\Big)^{2n} A_{2n} \tag{B.9}$$

with,

$$A_{2n} = \int_{-\infty}^{\infty} dt_1 \int_{-\infty}^{t_1} dt_2 \dots \int_{-\infty}^{t_{2n-1}} dt_{t_{2n}} \exp\Big[\frac{iv}{2}\sum_{j=0}^{2n}(-1)^j t_j^2\Big]. \tag{B.10}$$

The time ordered exponentials in Eq. (B.10) can be written using the Heaviside step function $\Theta(t)$, yielding

$$A_{2n} = \int_{-\infty}^{\infty} dt_1 \dots dt_{2n}\, \Theta(t_1 - t_2)\Theta(t_2 - t_3)\dots\Theta(t_{2n-1} - t_{2n}) \exp\Big[\frac{iv}{2}\sum_{j=0}^{2n}(-1)^j t_j^2\Big]. \tag{B.11}$$

The Heaviside function has the integral representation

$$\Theta(t) = \lim_{\epsilon\to 0^+} \frac{1}{2\pi i}\int_{-\infty}^{\infty} d\omega \frac{e^{i\omega t}}{\omega + i\epsilon}. \tag{B.12}$$

Inserting Eq. (B.12) into Eq. (B.11), completing the squares and evaluating the Gaussian integrals leads to

$$\begin{aligned} A_{2n} = \lim_{\epsilon\to 0^+} \frac{1}{(2\pi i)^{2n-1}} \left(\sqrt{\frac{2\pi}{\hbar v}}\right)^{2n} \int_{-\infty}^{\infty} d\omega_1 \dots d\omega_{2n-1} \\ \times \frac{1}{\omega_1 + i\epsilon} \frac{e^{i\omega_2(\omega_1 - \omega_3)}}{\omega_2 + i\epsilon} \frac{1}{\omega_3 + i\epsilon} \frac{e^{i\omega_2(\omega_3 - \omega_5)}}{\omega_4 + i\epsilon} \dots \frac{1}{\omega_{2n-1} + i\epsilon}, \end{aligned} \tag{B.13}$$

where we used that $2n$ is a even number. The integrals over even $\omega_k$ can be carried out using Eq. (B.12). This gives

$$\begin{aligned} A_{2n} = \lim_{\epsilon\to 0^+} \frac{1}{(2\pi i)^{n}} \left(\sqrt{\frac{2\pi}{\hbar v}}\right)^{2n} \int_{-\infty}^{\infty} d\omega_1 \dots d\omega_{n} \\ \times \frac{1}{\omega_1 + i\epsilon}\Theta(\omega_1 - \omega_2) \frac{1}{\omega_2 + i\epsilon}\Theta(\omega_2 - \omega_3) \dots \frac{1}{\omega_n + i\epsilon}, \end{aligned} \tag{B.14}$$

where we relabeled the odd indices. Eq. (B.14) can be interpreted as time ordered integrals of the function $1/(\omega + i\epsilon)$. Since the integrals are invariant under arbitrary permutations of the variables $\omega_k$, one can write

$$\begin{aligned} A_{2n} &= \lim_{\epsilon\to 0^+} \left(\frac{2\pi}{\hbar v}\right)^n \frac{1}{n!} \left(\frac{1}{2\pi i}\int_{-\infty}^{\infty} d\omega \frac{1}{\omega + i\epsilon}\right)^n \\ &= \frac{1}{n!}\left(\frac{2\pi}{\hbar v}\right)^n. \end{aligned} \tag{B.15}$$

Substituting Eq. (B.15) into the formal perturbation series (B.9) we obtain

$$|\bar{a}(\infty)|^2 = |a(\infty)|^2 = \exp\left(\frac{-\pi\Delta^2}{2\hbar v}\right), \tag{B.16}$$

what proves the Landau Zener formula Eq. (B.3). In this derivation, we calculated the transition probability between diabatic states, i.e., in the eigenstates of the uncoupled qubit. For $t \to \pm\infty$, however, diabatic states and adiabatic states (eigenstates of the full Hamiltonian) coincide. Therefore, Eq. (B.3) can also be interpreted as the probability to undergo a non-adiabatic transition by sweeping through the avoided crossing [20]. The ansatz used in this derivation has also been used to generalize the Landau-Zener formula to the situation where the qubit couples to one or several (also infinitely many) harmonic oscillators, see [19, 169, 170].

# Appendix C

# Bloch equations

In this appendix, we derive Bloch equations for an open two-level system. We start from the master equation (4.44). and notice that for the Ohmic spectral density $J(\omega) = 2\pi\alpha\omega$, the anti-symmetric bath correlation function (4.42) becomes $A(\tau) = 2\pi\alpha\delta'(\tau)$. This has for the $\tau$-integral in Eq. (4.44) the consequence that the Heisenberg operator $\tilde{X}$ turns into its time-derivative evaluated at $\tau = 0$. Thus it can be expressed by the commutator $i[H, X]$ and we obtain

$$\dot{\rho} = -i[H, \rho] - \frac{1}{4}[X, Q, \rho]] + \frac{\pi\alpha}{4}[X, \{[H, X], \rho\}], \tag{C.1}$$

where the second term depends on the coherent qubit dynamics via the operator

$$Q = \frac{1}{2}\int_{-\infty}^{+\infty} d\tau\, S(\tau)\tilde{X}(-\tau). \tag{C.2}$$

Since all analytical results of the main paper can be mapped by a permutation of the Pauli matrices to a qubit in its eigenbasis with a qubit-bath coupling via either $X = \sigma_x$ or $X = \sigma_z$, we consider the Hamiltonian

$$H = \frac{E}{2}\sigma_z. \tag{C.3}$$

For $X = \sigma_x$, the Heisenberg operator in Eq. (C.2) reads $\tilde{\sigma}_x(-\tau) = \sigma_x \cos(E\tau) - \sigma_y \sin(E\tau)$. With this expressions at hand, it is straightforward to evaluate the operator $Q$ and to map the master equation (C.1) to an equation of motion for the Bloch vector $\vec{s} = \mathrm{tr}(\vec{\sigma}\rho)$. After some algebra and a rotating-wave approximation, we find the Bloch equation

$$\frac{d}{dt}\vec{s} = \begin{pmatrix} -\Gamma/2 & E & 0 \\ -E & -\Gamma/2 & 0 \\ 0 & 0 & -\Gamma \end{pmatrix} \vec{s} + \begin{pmatrix} 0 \\ 0 \\ \pi\alpha E \end{pmatrix}, \tag{C.4}$$

where the rate

$$\Gamma = \pi\alpha E \coth(\beta E/2) \tag{C.5}$$

depends on the qubit splitting and at low temperatures, $kT \ll E$, it becomes $\Gamma = \pi\alpha|E|$.

For $\sigma_z$ coupling, the Heisenberg operator of the bath coupling is time independent, $\tilde{\sigma}_z(-\tau) = \sigma_z$, so that the $\tau$-integral yields the Fourier transform of the symmetric spectral density at zero frequency. Moreover, the last term of the master equation (C.1) vanishes. Accordingly, the Bloch equation is homogeneous and reads

$$\frac{d}{dt}\vec{s} = \begin{pmatrix} -\Gamma\varphi & E & 0 \\ -E & -\Gamma\varphi & 0 \\ 0 & 0 & 0 \end{pmatrix} \vec{s}, \tag{C.6}$$

where the dephasing rate

$$\Gamma_\varphi = 4\pi\alpha kT \tag{C.7}$$

vanishes in the zero-temperature limit. Notice that the $z$-component of the Bloch vector is conserved.

# Bibliography

[1] E. Schrödinger, *Quantisierung als Eigenwertproblem (Vierte Mitteilung)*, Ann. Phys. **81**, 109 (1926).

[2] M. Born, W. Heisenberg, and P. Jordan, *On quantum mechanics 2*, Z. Phys. **35**, 557 (1926).

[3] J. S. Briggs and J. M. Rost, *On the Derivation of the Time-Dependent Equation of Schrödinger*, Foundations of Physics **31**, 693 (2001).

[4] H.-P. Breuer and F. Petruccione, *Theory of open quantum systems* (Oxford University Press, Oxford, 2003).

[5] U. Weiss, *Quantum Dissipative Systems*, 2nd ed. (World Scientific, Singapore, 1998).

[6] C. W. Gardiner and P. Zoller, *Quantum Noise*, 3rd ed. (Springer, Berlin and Heidelberg, 2004).

[7] M. Campisi, P. Hänggi, and P. Talkner, *Quantum fluctuation relations: Foundations and applications*, Rev. Mod. Phys. **83**, 771 (2011).

[8] R. Dorner, S. R. Clark, L. Heaney, R. Fazio, J. Goold, and V. Vedral, *Extracting Quantum Work Statistics and Fluctuation Theorems by Single-Qubit Interferometry*, Phys. Rev. Lett. **110**, 230601 (2013).

[9] L. Mazzola, G. De Chiara, and M. Paternostro, *Measuring the Characteristic Function of the Work Distribution*, Phys. Rev. Lett. **110**, 230602 (2013).

[10] A. Blais *et al.*, *Quantum-information processing with circuit quantum electrodynamics*, Phys. Rev. A **75**, 032329 (2007).

[11] J. Avron and A. Elgart, *Adiabatic theorem without a gap condition*, Commun. Math. Phys. **203**, 445 (1999).

[12] M. Born and V. Fock, *Beweis des Adiabatensatzes*, Zeitschift für Physik **51**, 165 (1928).

[13] T. Kato, *On the adiabatic theorem of quantum mechanics*, J. Phys. Soc. Jpn. **5**, 435 (1950).

[14] H. Nakamura, *Nonadiabatic Transition: Concepts, Basic Theories and Applications* (World Scientific, Singapore, 2002).

[15] L. D. Landau, *Zur Theorie der Energieübertragung bei Stößen*, Phys. Z. Sowjetunion **2**, 46 (1932).

[16] C. Zener, *Non-adiabatic crossing of energy levels*, Proc. R. Soc. London, Ser. A **137**, 696 (1932).

[17] E. C. G. Stückelberg, *Theorie der unelastischen Stösse zwischen Atomen*, Helv. Phys. Acta **5**, 369 (1932).

[18] E. Majorana, *Atomi orientati in campo magnetico variable*, Nuovo Cimento **9**, 43 (1932).

[19] K. Saito, M. Wubs, S. Kohler, P. Hänggi, and Y. Kayanuma, *Quantum state preparation in circuit QED via Landau-Zener tunneling*, Europhys. Lett. **76**, 22 (2006).

[20] S. N. Shevchenko, S. Ashhab, and F. Nori, *Landau-Zener-Stückelberg interferometry*, Phys. Rep. **492**, 1 (2010).

[21] G. Casati and L. Molinari, *Quantum Chaos with Time-Periodic Hamiltonians*, Progress of Theoretical Physics **98**, 287 (1989).

[22] M. Grifoni and P. Hänggi, *Driven Quantum Tunneling*, Phys. Rep. **304**, 229 (1998).

[23] A. Shapere and F. Wilczek, *Geometric phases in Physics* (World Scientific, Singapore, 1989).

[24] N. H. Lindner, G. Refael, and V. Galitski, *Floquet topological insulator in semiconductor quantum wells*, Nature Phys. **7**, (2011).

[25] W. D. Oliver, Y. Yu, J. C. Lee, K. K. Berggren, L. S. Levitov, and T. P. Orlando, *Mach-Zehnder Interferometry in a Strongly Driven Superconducting Qubit*, Science **310**, 1653 (2005).

[26] M. Sillanpää, T. Lehtinen, A. Paila, Y. Makhlin, and P. Hakonen, *Continuous-time monitoring of Landau-Zener interference in a Cooper-pair box*, Phys. Rev. Lett. **96**, 187002 (2006).

[27] C. M. Wilson, T. Duty, F. Persson, M. Sandberg, G. Johansson, and P. Delsing, *Coherence Times of Dressed States of a Superconducting Qubit under Extreme Driving*, Phys. Rev. Lett. **98**, 257003 (2007).

[28] A. Izmalkov *et al.*, *Consistency of Ground State and Spectroscopic Measurements on Flux Qubits*, Phys. Rev. Lett. **101**, 017003 (2008).

[29] D. M. Berns *et al.*, *Amplitude spectroscopy of a solid-state artificial atom*, Nature **455**, 51 (2008).

[30] J. Stehlik *et al.*, *Landau-Zener-Stuckelberg Interferometry of a Single Electron Charge Qubit*, Phys. Rev. B **86**, 121303(R) (2012).

[31] E. Dupont-Ferrier *et al.*, *Coherent Coupling of Two Dopants in a Silicon Nanowire Probed by Landau-Zener-Stückelberg Interferometry*, Phys. Rev. Lett. **110**, 136802 (2013).

[32] J. Li *et al.*, *Motional averaging in a superconducting qubit*, Nature Comm. **4**, 1420 (2013).

[33] M. S. Rudner *et al.*, *Quantum Phase Tomography of a Strongly Driven Qubit*, Phys. Rev. Lett. **101**, 190502 (2008).

[34] F. Forster *et al.*, *Characterization of Qubit Dephasing by Landau-Zener-Stückelberg-Majorana Interferometry*, Phys. Rev. Lett. **112**, 116803 (2014).

[35] F. Ritort, *Nonequilibrium fluctuations in small systems: From physics to biology*, Adv. Chem. Phys. **137**, 31 (2008).

[36] A. Altland and B. Simons, *Condensed matter field theory* (Cambridge University Press, Cambridge, 2010).

[37] A. Denisov, H. M. Castro-Beltran, and H. J. Carmichael, *Time-Asymmetric Fluctuations of Light and the Breakdown of Detailed Balance*, Phys. Rev. Lett. **88**, 243601 (2002).

[38] V. Vedral, *The role of relative entropy in quantum information theory*, Rev. Mod. Phys. **74**, 197 (2002).

[39] M. Esposito and S. Mukamel, *Fluctuation theorems for quantum master equations*, Phys. Rev. E **73**, 046129 (2006).

[40] C. Jarzynski, *Equalities and Inequalities: Irreversibility and the Second Law of Thermodynamics at the Nanoscale*, Ann. Rev. Cond. Mat. Phys. **2**, 329 (2011).

[41] U. Seifert, *Stochastic thermodynamics, fluctuation theorems, and molecular machines*, Rep. Prog. Phys. **75**, 126001 (2012).

[42] A. Einstein, *Eine neue Bestimmung der Moleküldimensionen*, Ann. Phys. **324**, 289 (1906).

[43] A. Einstein, *Zur Theorie der Brownschen Bewegung*, Ann. Phys. **324**, 371 (1906).

[44] W. Sutherland, *Dynamical theory of diffusion for non- electrolytes and the molecular mass of albumin*, Philos. Mag. **9**, 781 (1905).

[45] D. J. Evans, E. G. D. Cohen, and G. P. Morriss, *Probability of second law violations in shearing steady states*, Phys. Rev. Lett. **71**, 2401 (1993).

[46] G. Gallavotti and E. G. D. Cohen, *Dynamical Ensembles in Nonequilibrium Statistical Mechanics*, Phys. Rev. Lett. **74**, 2694 (1995).

[47] M. Campisi, R. Blattmann, S. Kohler, D. Zueco, and P. Hänggi, *Employing circuit QED to measure non-equilibrium work fluctuations*, New J. Phys. **15**, 105028 (2013).

[48] S. Weinberg, *Quantum theory of fields Vol. 1* (Cambridge University Press, Cambridge, 1995).

[49] B. P. Venkatesh, G. Watanabe, and P. Talkner, *Transient quantum fluctuation theorems and generalized measurements*, New J. Phys. **16**, 015032 (2014).

[50] G. Watanabe, B. P. Venkatesh, P. Talkner, M. Campisi, and P. Hänggi, *Quantum fluctuation theorems and generalized measurements during the force protocol*, Phys. Rev. E **89**, 032114 (2014).

[51] P. Talkner, E. Lutz, and P. Hänggi, *Fluctuation theorems: Work is not an observable*, Phys. Rev. E **75**, 050102(R) (2007).

[52] J. v. Neumann, *Mathematical Foundations of Quantum Mechanics* (Princeton University Press, Princeton, 1955).

[53] P. Talkner and P. Hänggi, *The Tasaki-Crooks quantum fluctuation theorem*, J. Phys. A **40**, F569 (2007).

[54] A. Messiah, *Quantum Mechanics, vol. 2* (North Holland, Amsterdam, 1962).

[55] M. Campisi, *Quantum fluctuation relations for ensembles of wave functions*, New Journal of Physics **15**, 115008 (2013).

[56] J. Liphardt, B. Onoa, S. Smith, J. I. Tinoco, and C. Bustamante, *Reversible Unfolding of Single RNA Molecules Using Mechanical Force*, Science **296**, 1832 (2002).

[57] D. Collin, F. Ritort, C. Jarzynski, S. B. Smith, I. Tinoco, and C. Bustamante, *Verification of the Crooks fluctuation theorem and recovery of RNA folding free energies*, Nature **437**, 231 (2005).

[58] G. Huber, F. Schmidt-Kaler, S. Deffner, and E. Lutz, *Employing Trapped Cold Ions to Verify the Quantum Jarzynski Equality*, Phys. Rev. Lett. **101**, 070403 (2008).

[59] S. Deffner, O. Abah, and E. Lutz, *Quantum work statistics of linear and nonlinear parametric oscillators*, Chem. Phys. **375**, 200 (2010).

[60] M. Campisi, P. Talkner, and P. Hänggi, *Fluctuation Theorem for Arbitrary Open Quantum Systems*, Phys. Rev. Lett. **102**, 210401 (2009).

[61] R. P. Feynman and F. L. Vernon, *The theory of a general quantum system interacting with a linear dissipative system*, Ann. Phys. **24**, 118 (1963).

[62] C. Jarzynski, *Nonequilibrium Equality for Free Energy Differences*, Phys. Rev. Lett. **78**, 2690 (1997).

[63] P. Pechukas, *Reduced Dynamics Need Not Be Completely Positive*, Phys. Rev. Lett. **73**, 1060 (1994).

[64] D. Kafri and S. Deffner, *Holevo's bound from a general quantum fluctuation theorem*, Phys. Rev. A **86**, 044302 (2012).

[65] T. Albash, D. A. Lidar, M. Marvian, and P. Zanardi, *Fluctuation theorems for quantum processes*, Phys. Rev. E **88**, 032146 (2013).

[66] A. E. Rastegin, *Non-equilibrium equalities with unital quantum channels*, J. Stat. Mech. **06**, P06016 (2013).

[67] R. Chetrite and K. Mallick, *Quantum fluctuation relations for the Lindblad master equation*, J. Stat. Phys. **148**, 480 (2012).

[68] M. Tinkham, *Introduction to superconductivity* (McGraw-Hill, Inc, New York, 1996).

[69] V. Ginzburg, *On the theory of superconductivity*, J. Exp. Theoret. Phys. **20**, 1064 (1950).

[70] L. N. Cooper, *Bound Electron Pairs in a Degenerate Fermi Gas*, Phys. Rev. **104**, 1189 (1956).

[71] J. Bardeen, L. N. Cooper, and J. R. Schrieffer, *Theory of Superconductivity*, Phys. Rev. **108**, 1175 (1957).

[72] B. D. Josephson, *Possible new effects in superconductive tunnelling*, Phys. Lett. **1**, 251 (1962).

[73] B. Yurke and J. S. Denker, *Quantum network theory*, Phys. Rev. A **29**, 1419 (1984).

[74] M. H. Devoret, *Quantum Fluctuations in Electrical circuits*, in *Quantum Fluctuations in Electrical circuits*, *Les Houches, Session LXIII* (Elsevier, Amsterdam, 1995), Chap. 10.

[75] M. H. Devoret, A. Wallraff, and J. M. Martinis, *Superconducting Qubits: A Short Review*, arXiv:cond-mat/0411174 (2004).

[76] Y. Makhlin, G. Schön, and A. Shnirman, *Quantum-state engineering with Josephson-junction devices*, Rev. Mod. Phys. **73**, 357 (2001).

[77] J. Q. You and F. Nori, *Superconducting Circuits and Quantum Information*, Phys. Today **58**, 42 (2005).

[78] J. Clarke and F. K. Wilhelm, *Superconducting quantum bits*, Nature **453**, 1031 (2008).

[79] A. Blais, R.-S. Huang, A. Wallraff, S. M. Girvin, and R. J. Schoelkopf, *Cavity quantum electrodynamics for superconducting electrical circuits: An architecture for quantum computation*, Phys. Rev. A **69**, 062320 (2004).

[80] H. Walther, B. T. H. Varcoe, B.-G. Englert, and T. Becker, *Cavity quantum electrodynamics*, Rep. Prog. Phys. **69**, 1325 (2006).

[81] I. I. Rabi, *On the Process of Space Quantization*, Phys. Rev. **49**, 324 (1936).

[82] D. Braak, *Integrability of the Rabi Model*, Phys. Rev. Lett. **107**, 100401 (2011).

[83] T. Niemczyk *et al.*, *Circuit quantum electrodynamics in the ultrastrong-coupling regime*, Nature Phys. **6**, 772 (2010).

[84] A. Wallraff *et al.*, *Strong coupling of a single photon to a superconducting qubit using circuit quantum electrodynamics*, Nature **431**, 162 (2004).

[85] G. M. Reuther, D. Zueco, P. Hänggi, and S. Kohler, *Time-Resolved Measurement of a Charge Qubit*, Phys. Rev. Lett. **102**, 033602 (2009).

[86] B. Peropadre, P. Forn-D’ıaz, E. Solano, and J. J. Garc’ıa-Ripoll, *Switchable Ultrastrong Coupling in Circuit QED*, Phys. Rev. Lett. **105**, 023601 (2010).

[87] D. Zueco, G. M. Reuther, S. Kohler, and P. Hänggi, *Qubit-oscillator dynamics in the dispersive regime: analytical theory beyond the rotating-wave approximation*, Phys. Rev. A **80**, 033846 (2009).

[88] S. Filipp *et al.*, *Two-Qubit State Tomography Using a Joint Dispersive Readout*, Phys. Rev. Lett. **102**, 200402 (2009).

[89] J. Casanova, G. Romero, I. Lizuain, J. J. García-Ripoll, and E. Solano, *Deep Strong Coupling Regime of the Jaynes-Cummings Model*, Phys. Rev. Lett. **105**, 263603 (2010).

[90] G. M. Reuther, D. Zueco, P. Hänggi, and S. Kohler, *Time-resolved qubit readout via nonlinear Josephson inductance*, New J. Phys. **13**, 093022 (2011).

[91] D. Deutsch, *Quantum theory, the Church-Turing principle and the universal quantum computer*, Proc. R. Soc. Lond. A **400**, 97 (1985).

[92] D. Deutsch and R. Jozsa, *Rapid Solution of Problems by Quantum Computation*, Proc. R. Soc. Lond. A **439**, 553 (1992).

[93] L. K. Grover, *A fast quantum mechanical algorithm for database search*, arXiv:quant-ph/9605043 (1996).

[94] P. W. Shor, in *Proc. 35th Annual Symposium on the foundations of computer science*, edited by S. Goldwasser (IEEE Computer Society Press, Los Alamitos, CA, 1994), pp. 124–134.

[95] M. A. Nielsen and I. L. Chuang, *Quantum Computing and Quantum Information* (Cambridge University Press, Cambridge, 2000).

[96] R. Horodecki, P. Horodecki, M. Horodecki, and K. Horodecki, *Quantum entanglement*, Rev. Mod. Phys. **81**, 865 (2009).

[97] D. P. Di Vincenzo, *The Physical Implementation of Quantum Computation*, Fortschr. Phys. **48**, 771 (2000).

[98] M. Wubs, S. Kohler, and P. Hänggi, *Entanglement creation in circuit QED via Landau-Zener sweeps*, Physica E **40**, 187 (2007).

[99] H. Ribeiro and G. Burkhard, *Nuclear State Preparation via Landau-Zener-Stckelberg Transitions in Double Quantum Dots*, Phys. Rev. Lett. **102**, 216802 (2009).

[100] J. I. Cirac, P. Zoller, H. J. Kimble, and H. Mabuchi, *Quantum State Transfer and Entanglement Distribution among Distant Nodes in a Quantum Network*, Phys. Rev. Lett. **78**, 3221 (1997).

[101] W. Ya, R.-B. Liu, and L. J. Sham, *Theory of Control of the Spin-Photon Interface for Quantum Networks*, Phys. Rev. Lett. **95**, 030504 (2005).

[102] D. A. Fuhrmann *et al.*, *Dynamic modulation of photonic crystal nanocavities using gigahertz acoustic phonons*, Nature Phot. **5**, 605 (2011).

[103] R. Blattmann, H. J. Krenner, S. Kohler, and P. Hänggi, *Entanglement creation in a quantum dot-nanocavity system by Fourier-synthesized acoustic pulses*, Phys. Rev. A **89**, 012327 (2014).

[104] M. B. Plenio and S. Virmani, *An introduction to entanglement measures*, Quant. Inf. Comput. **7**, 1 (2007).

[105] L. Amico, R. Fazio, A. Osterloh, and V. Vedral, *Entanglement in Many-Body Systems*, Rev. Mod. Phys. **80**, 517 (2008).

[106] S. Hill and K. Wooters, *Entanglement of a Pair of Quantum Bits*, Phys. Rev. Lett. **78**, 5022 (1997).

[107] W. K. Wootters, *Entanglement of Formation of an Arbitrary State of Two Qubits*, Phys. Rev. Lett. **80**, 2245 (1998).

[108] C. H. Bennett, D. P. DiVincenzo, J. A. Smolin, and W. K. Wootters, *Mixed-state entanglement and quantum error correction*, Phys. Rev. A **54**, 3824 (1996).

[109] A. Zrenner, E. Beham, S. Stufler, F. Findeis, M. Bichler, and G. Abstreiter, *Coherent properties of a two-level system based on a quantum-dot photodiode*, Nature **418**, 612 (2002).

[110] Y. Akahane, T. Asano, B. S. Song, and S. Noda, *High-Q photonic nanocavity in a two-dimensional photonic crystal*, Nature **425**, 944 (2003).

[111] E. Yablonovitch, *Inhibited Spontaneous Emission in Solid-State Physics and Electronics*, Phys. Rev. Lett. **58**, 2059 (1987).

[112] E. Yablonovitch, T. J. Gmitter, and K. M. Leung, *Photonic band structure: The face-centered-cubic case employing nonspherical atoms*, Phys. Rev. Lett. **67**, 2295 (1991).

[113] A. Faraon, A. Majumdar, D. Englund, E. Kim, M. Bajcsy, and J. Vukovi, *Integrated quantum optical networks based on quantum dots and photonic crystals*, New J. Phys. **13**, 055025 (2011).

[114] C. W. Gardiner, *Quantum Noise*, Vol. 56 of *Springer Series in Synergetics* (Springer, Berlin, 1991).

[115] D. F. Walls and G. J. Milburn, *Quantum Optics*, 2 ed. (Springer, Heidelberg, 1995).

[116] S. Noda, M. Fujita, and T. Asano, *Spontaneous-emission control by photonic crystals and nanocavities*, Nature Phot. **1**, 449 (2007).

[117] D. Englund *et al.*, *Controlling the Spontaneous Emission Rate of Single Quantum Dots in a Two-Dimensional Photonic Crystal*, Phys. Rev. Lett. **95**, 013904 (2005).

[118] A. Kress *et al.*, *Manipulation of the spontaneous emission dynamics of quantum dots in two-dimensional photonic crystals*, Phys. Rev. B **71**, 241304 (2005).

[119] W.-H. Chang, W.-Y. Chen, H.-S. Chang, T.-P. Hsieh, J.-I. Chyi, and T.-M. Hsu, *Efficient Single-Photon Sources Based on Low-Density Quantum Dots in Photonic-Crystal Nanocavities*, Phys. Rev. Lett. **96**, 117401 (2006).

[120] T. Yoshie *et al.*, *Vacuum Rabi splitting with a single quantum dot in a photonic crystal nanocavity*, Nature **432**, 200 (2004).

[121] K. Hennessy *et al.*, *Quantum nature of a strongly coupled single quantum dot-cavity system*, Nature **445**, 896 (2007).

[122] D. Englund, A. Faraon, I. Fushman, N. Stoltz, P. Petroff, and J. Vuckovic, *Controlling cavity reflectivity with a single quantum dot*, Nature **450**, 857 (2007).

[123] A. Laucht *et al.*, *Dephasing of Exciton Polaritons in Photoexcited InGaAs Quantum Dots in GaAs Nanocavities*, Phys. Rev. Lett. **103**, 87405 (2009).

[124] S. M. Thon *et al.*, *Strong coupling through optical positioning of a quantum dot in a photonic crystal cavity*, Appl. Phys. Lett. **94**, 111115 (2009).

[125] F. J. R. Schülein *et al.*, *Acoustically regulated carrier injection into a single optically active quantum dot*, Phys. Rev. B **88**, 085307 (2013).

[126] J. R. Gell *et al.*, *Modulation of single quantum dot energy levels by a surface-acoustic-wave*, Appl. Phys. Lett. **93**, 81115 (2008).

[127] W. H. Zurek, *Decoherence, einselection, and the quantum origins of the classical*, Rev. Mod. Phys. **75**, 715 (2003).

[128] K. Blum, *Density Matrix Theory and Applications*, 2nd ed. (Springer, New York, 1996).

[129] A. J. Leggett, S. Chakravarty, A. T. Dorsey, M. P. A. Fisher, A. Garg, and W. Zwerger, *Dynamics of the dissipative two-state system*, Rev. Mod. Phys. **59**, 1 (1987).

[130] P. Hänggi, P. Talkner, and M. Borkovec, *Reaction-rate theory: fifty years after Kramers*, Rev. Mod. Phys. **62**, 251 (1990).

[131] G. Lindblad, *On the Generators of Quantum Dynamical Semigroups*, Commun. Math. Phys. **48**, 119 (1976).

[132] V. Gorini, A. Kossakowski, and E. C. G. Sudarshan, *Completely positive dynamical semigroups of N-level systems*, J. Math. Phys. **17**, 821 (1976).

[133] J. P. Reithmaier *et al.*, *Strong coupling in a single quantum dot-semiconductor microcavity system*, Nature **432**, 197 (2004).

[134] M. M. de Lima Jr. and P. V. Santos, *Modulation of photonic structures by surface acoustic waves*, Rep. Prog. Phys. **68**, 1639 (2005).

[135] A. Faraon, A. Majumdar, H. Kim, P. Petroff, and J. Vučković, *Fast Electrical Control of a Quantum Dot Strongly Coupled to a Photonic-Crystal Cavity*, Phys. Rev. Lett. **104**, 047402 (2010).

[136] C. Kistner, S. Reitzenstein, C. Schneider, S. Höfling, and A. Forchel, *Resonantly probing micropillar cavity modes by photocurrent spectroscopy*, Appl. Phys. Lett. **94**, 221103 (2009).

[137] M. Rakher, N. Stoltz, L. Coldren, P. Petroff, and D. Bouwmeester, *Externally Mode-Matched Cavity Quantum Electrodynamics with Charge-Tunable Quantum Dots*, Phys. Rev. Lett. **102**, 097403 (2009).

[138] R. Blattmann, P. Hänggi, and S. Kohler, *Qubit interference at avoided crossings: The role of driving shape and bath coupling*, arxiv:cond-mat/1409.5237 (2014).

[139] L. Zehnder, *Ein neuer Interferenzrefraktor*, Zeitschrift für Instrumentenkunde **11**, 275 (1891).

[140] L. Mach, *Über einen Interferenzrefraktor*, Zeitschrift für Instrumentenkunde **12**, 89 (1892).

[141] Y. Kayanuma, *Stokes phase and geometrical phase in a driven two-level system*, Phys. Rev. A **55**, R2495 (1997).

[142] M. C. Baruch and T. F. Gallagher, *Ramsey interference fringes in single pulse microwave multiphoton transitions*, Phys. Rev. Lett. **68**, 3515 (1992).

[143] M. Strass, P. Hänggi, and S. Kohler, *Nonadiabatic Electron Pumping: Maximal Current with Minimal Noise*, Phys. Rev. Lett. **95**, 130601 (2005).

[144] S. Ashhab, J. R. Johansson, and F. Nori, *Decoherence in a scalable quantum computer*, Phys. Rev. A **74**, 052330 (2006).

[145] M. Abramowitz and I. A. Stegun, *Handbook of Mathematical Functions With Formulas, Graphs, and Mathematical Tables*, 9th ed. (Dover Publications, New York, 1965).

[146] F. Grossmann, T. Dittrich, P. Jung, and P. Hänggi, *Coherent Destruction of Tunneling*, Phys. Rev. Lett. **67**, 516 (1991).

[147] J. H. Shirley, *Solution of the Schrödinger Equation with a Hamiltonian Periodic in Time*, Phys. Rev. **138**, B979 (1965).

[148] P. Hänggi, *Quantum Transport and Dissipation* (Wiley-VCH, Weinheim, 1998), Chap. 5, pp. 249–286.

[149] H. Sambe, *Steady States and Quasienergies of a Quantum-Mechanical System in an Oscillating Field*, Phys. Rev. A **7**, 2203 (1973).

[150] S. Kohler, T. Dittrich, and P. Hänggi, *Floquet-Markovian description of the parametrically driven, dissipative harmonic quantum oscillator*, Phys. Rev. E **55**, 300 (1997).

[151] R. Blümel, A. Buchleitner, R. Graham, L. Sirko, U. Smilansky, and H. Walter, *Dynamical localisation in the microwave interaction of Rydberg atoms: The influence of noise*, Phys. Rev. A **44**, 4521 (1991).

[152] P. Neilinger, M. Rehák, U. Hübner, E. Il'ichev, and M. Grajcar, *Mach Zehnder interferometry in an artificial quantum two level system*, in *20th International Conference on Applied Physics of Condensed Matter* (FEI STU, Bratislava, 2014), pp. 26–29.

[153] T. M. Stace, A. C. Doherty, and S. D. Barrett, *Population Inversion of a Driven Two-Level System in a Structureless Bath*, Phys. Rev. Lett. **95**, 106801 (2005).

[154] A. Ferrón, D. Domínguez, and M. J. Sánchez, *Tailoring Population Inversion in Landau-Zener-Stückelberg Interferometry of Flux Qubits*, Phys. Rev. Lett. **109**, 237005 (2012).

[155] J. Hauss, A. Fedorov, C. Hutter, A. Shnirman, and G. Schön, *Single-Qubit Lasing and Cooling at the Rabi Frequency*, Phys. Rev. Lett. **100**, 037003 (2008).

[156] K. M. Fonseca-Romero, S. Kohler, and P. Hänggi, *Coherence control for qubits*, Chem. Phys. **296**, 307 (2004).

[157] J. W. Cooley and J. W. Tukey, *An algorithm for the machine calculation of complex Fourier series*, Math. Comput. **19**, 297 (1965).

[158] A. M. Satanin, M. V. Denisenko, A. I. Gelman, and F. Nori, *Amplitude and phase effects in Josephson qubits driven by a biharmonic electromagnetic field*, Phys. Rev. B **90**, 104516 (2014).

[159] T. W. Körner, *Fourier Analysis* (Cambridge University Press, Cambridge, 1989).

[160] M. N. Kiselev, K. Kikoin, and M. B. Kenmoe, *SU(3) Landau-Zener interferometry*, EPL **104**, 57004 (2013).

[161] A. M. Satanin, M. V. Denisenko, S. Ashhab, and F. Nori, *Amplitude spectroscopy of two coupled qubits*, Phys. Rev. B **85**, 184524 (2012).

[162] H. Ribeiro, G. Burkard, J. R. Petta, H. Lu, and A. C. Gossard, *Coherent Adiabatic Spin Control in the Presence of Charge Noise Using Tailored Pulses*, Phys. Rev. Lett. **110**, 086804 (2013).

[163] W. Schleich, *Quantum Optics in Phase Space* (Wiley VCH, Weinheim, 2001).

[164] C. Wittig, *The Landau-Zener formula*, J. Phys. Chem. B **109**, 8428 (2005).

[165] F. Wilczek, *Majorana and Condensed Matter Physics*, arxiv:cond-mat/1404.0637 (2014).

[166] A. I. Chichinin, *Comment on The LandauZener Formula*, J. Phys. Chem. B **117**, 6018 (2013).

[167] Y. Kayanuma, *Nonadiabatic Transitions in Level Crossing with Energy Fluctuation. I: Analytical Investigations*, J. Phys. Soc. Jpn. **53**, 108 (1984).

[168] A. G. Rojo, *Matrix exponential solution of the Landau-Zener problem*, arxiv:quant-ph/1004.2914 (2010).

[169] M. Wubs, K. Saito, S. Kohler, P. Hänggi, and Y. Kayanuma, *Gauging a Quantum Heat Bath with Dissipative Landau-Zener Transitions*, Phys. Rev. Lett. **97**, 200404 (2006).

[170] K. Saito, M. Wubs, S. Kohler, Y. Kayanuma, and P. Hänggi, *Dissipative Landau-Zener transitions of a qubit: bath-specific and universal behavior*, Phys. Rev. B **75**, 214308 (2007).

# Danksagungen

Ich möchte mich bei allen Kollegen und Freunden bedanken, die im Laufe der Jahre direkt oder indirekt zur vorliegenden Dissertation beigetragen haben. Zunächst einmal richtet sich mein Dank an Peter Hänggi, der mir die Möglichkeit gegeben hat am Lehrstuhl für theoretische Physik 1 zu promovieren. Der erfolgreiche Abschluss dieser Arbeit baut maßgeblich auf seiner Erfahrung, seinem Enthusiasmus, und seiner fortwährenden Unterstützung, sowie auf seiner Fähigkeit seine Mitarbeiter immer wieder aufs Neue zu motivieren.

Besonderer Dank gebührt sicherlich Sigmund Kohler, der mich trotz der großen Distanz hervorragend betreut hat. Ohne seine Motivation, seine Ideen, und seine bewundernswerte Geduld beim Beantworten meiner Fragen, wäre diese Arbeit nicht in dieser Form möglich gewesen. Darüber hinaus werde ich die Zeit, die ich bei ihm in Madrid verbringen durfte, immer in guter Erinnerung behalten.

Ich möchte mich außerdem bei Allen bedanken, die in den letzten Jahren mit mir zusammengearbeitet haben. Speziell bei Michele Campisi und Hubert Krenner, der mir viele konkrete Einblicke in experimentelle Fragestellungen gewährt hat. Gert Ingold hat durch einige hilfreiche Tipps zur Programmierung ebenfalls zum Gelingen dieser Arbeit beigetragen. Darüber hinaus gilt mein Dank Georg Reuther, Anonio Hill, Johannes Wanner, Gerhard Schmid und Ralf Utermann für die vielfältige Unterstützung bei der Bewältigung von Computer-Administrationsaufgaben. Speziell Georg Reuther hat mich bestmöglich eingearbeitet und dazu beigetragen, dass mir der Wechsel nach Augsburg nicht schwer gefallen ist. Auch bedanken möchte ich mich bei Frau Geiger für die Hilfe bei verschiedenen organisatorischen Problemstellungen. Ausserdem möchte ich allen jetzigen und früheren Mitgliedern des Lehrstuhls für theoretische Physik 1 herzlich Danke sagen, für die angenehme und stimulierende Arbeitsumgebung. Besonders erwähnt seien Ao Xue, Stephan Umrath und Alexander Geiseler, mit denen ich zum Teil mehrere Jahre das Büro geteilt habe, und Armin Seibert, der sich auf diversen Workshops das Zimmer mit mir geteilt hat.

Hervorheben möchte ich auch die finazielle Unterstützung meiner Arbeit durch den SFB 631, sowie durch die "Nanosystem Initiative München" (NIM) im Rahmen ihres Graduiertenprogrammes.

Zu guter Letzt gilt mein Dank meinen Eltern, meiner Familie und vor allem Carla Lux, dafür, dass sie mich stets unterstützt und in meinen Entscheidungen bestärkt haben.

# Lebenslauf

Name: Ralf Blattmann
Geburtsdatum: 08. Februar 1986
Geburtsort: Freiburg im Breisgau
Familienstand: ledig

Juni 2005: Abitur, Kolleg St. Sebastian, Stegen
Oktober 2005 – Dezember 2011: Physikstudium an der Albert–Ludwigs–Universität Freiburg
Februar 2010: Diplomprüfung
August 2010 – Dezember 2011: Diplomarbeit in theoretischer Physik
bei Prof. Dr. Andreas Buchleitner
Januar 2012 – : Wissenschaftlicher Mitarbeiter, Universität Augsburg,
Lehrstuhl für theoretische Physik 1
Promotion bei Prof. Dr. Peter Hänggi